

---


Electronic Theses and Dissertations, 2004-2019

---

2010

## Development Of Optical Coherence Tomography For Tissue Diagnostics

Panomsak Meemon  
*University of Central Florida*

 Part of the [Electromagnetics and Photonics Commons](#), and the [Optics Commons](#)  
Find similar works at: <https://stars.library.ucf.edu/etd>  
University of Central Florida Libraries <http://library.ucf.edu>

This Doctoral Dissertation (Open Access) is brought to you for free and open access by STARS. It has been accepted for inclusion in Electronic Theses and Dissertations, 2004-2019 by an authorized administrator of STARS. For more information, please contact [STARS@ucf.edu](mailto:STARS@ucf.edu).

---

### STARS Citation

Meemon, Panomsak, "Development Of Optical Coherence Tomography For Tissue Diagnostics" (2010).  
*Electronic Theses and Dissertations, 2004-2019*. 1646.  
<https://stars.library.ucf.edu/etd/1646>

DEVELOPMENT OF OPTICAL COHERENCE TOMOGRAPHY  
FOR TISSUE DIAGNOSTICS

by

PANOMSAK MEEMON

B.S. Chiang Mai University, Thailand, 2000  
M.S. University of Central Florida, USA, 2007

A dissertation submitted in partial fulfillment of the requirements  
for the degree of Doctor of Philosophy  
in the College of Optics and Photonics  
at the University of Central Florida  
Orlando, Florida

Fall Term  
2010

Major Professor: Jannick P. Rolland

© 2010 Panomsak Meemon

## ABSTRACT

Microvasculature can be found in almost every part of the human body, including the internal organs. Importantly, abnormal changes in microvasculature are usually related to pathological development of the tissue cells. Monitoring of changes in blood flow properties in microvasculature, therefore, provides useful diagnostic information about pathological conditions in biological tissues as exemplified in glaucoma, diabetes, age related macular degeneration, port wine stains, burn-depth, and potentially skin cancer. However, the capillary network is typically only one cell in wall thickness with 5 to 10 microns in diameter and located in the dermis region of skin. Therefore, a non-invasive flow imaging technique that is capable of depth sectioning at high resolution and high speed is demanded. Optical coherence tomography (OCT), particularly after its advancement in frequency domain OCT (FD-OCT), is a promising tool for non-invasive high speed, high resolution, and high sensitivity depth-resolved imaging of biological tissues. Over the last ten years, numerous efforts have been paid to develop OCT-based flow imaging techniques. An important effort is the development of phase-resolved Doppler OCT (PR-DOCT).

Phase-resolved Doppler imaging using FD-OCT is particularly of interest because of the direct access to the phase information of the depth profile signal. Furthermore, the high speed capability of FD-OCT is promising for real time flow monitoring as well as 3D flow segmentation applications. However, several challenges need to be addressed; 1) Flow in biological samples exhibits a wide dynamic range of flow velocity caused by, for example, the

variation in the flow angles, flow diameters, and functionalities. However, the improvement in imaging speed of FD-OCT comes at the expense of a reduction in sensitivity to slow flow information and hence a reduction in detectable velocity range; 2) A structural ambiguity so-called 'mirror image' in FD-OCT prohibits the use of maximum sensitivity and imaging depth range; 3) The requirement of high lateral resolution to resolve capillary vessels requires the use of an imaging optics with high numerical aperture (NA) that leads to a reduction in depth of focus (DOF) and hence the imaging depth range (i.e. less than 100 microns) unless dynamic focusing is performed. Nevertheless, intrinsic to the mechanism of FD-OCT, dynamic focusing is not possible.

In this dissertation, the implementation of PR-DOCT in a high speed swept-source based FD-OCT is investigated and optimized. An acquisition scheme as well as a processing algorithm that effectively extends the detectable velocity dynamic range of the PR-DOCT is presented. The proposed technique increased the overall detectable velocity dynamic range of PR-DOCT by about five times of that achieved by the conventional method. Furthermore, a novel technique of mirror image removal called 'Dual-Detection FD-OCT' (DD-FD-OCT) is presented. One of the advantages of DD-FD-OCT to Doppler imaging is that the full-range signal is achieved without manipulation of the phase relation between consecutive axial lines. Hence the full-range DD-FD-OCT is fully applicable to phase-resolved Doppler detection without a reduction in detectable velocity dynamic range as normally encountered in other full-range techniques. In addition, PR-DOCT can utilize the maximum SNR provided by the full-range capability. This capability is particularly useful for imaging of blood flow that locates deep below the sample surface, such as

blood flow at deep posterior human eye and blood vessels network in the dermis region of human skin.

Beside high speed and functional imaging capability, another key parameter that will open path for optical diagnostics using OCT technology is high resolution imaging (i.e. in a regime of a few microns or sub-micron). Even though the lateral resolution of OCT can be independently improved by opening the NA of the imaging optics, the high lateral resolution is maintained only over a short range as limited by the depth of focus that varies inversely and quadratically with NA. Recently developed by our group, ‘Gabor-Domain Optical Coherence Microscopy’ (GD-OCM) is a novel imaging technique capable for invariant resolution of about 2-3  $\mu\text{m}$  over a 2 mm cubic field-of-view. This dissertation details the imaging protocol as well as the automatic data fusion method of GD-OCM developed to render an in-focus high-resolution image throughout the imaging depth of the sample in real time. For the application of absolute flow measurement as an example, the precise information about flow angle is required. GD-OCM provides more precise interpretation of the tissue structures over a large field-of-view, which is necessary for accurate mapping of the flow structure and hence is promising for diagnostic applications particularly when combined with Doppler imaging.

Potentially, the ability to perform high resolution OCT imaging inside the human body is useful for many diagnostic applications, such as providing an accurate map for biopsy, guiding surgical and other treatments, monitoring the functional state and/or the post-operative recovery process of internal organs, plaque detection in arteries, and early detection of cancers in the gastrointestinal tract. Endoscopic OCT utilizes a special miniature probe in the sample arm to

access tubular organs inside the human body, such as the cardiovascular system, the lung, the gastrointestinal tract, the urinary tract, and the breast duct. We present an optical design of a dynamic focus endoscopic probe that is capable of about 4 to 6  $\mu\text{m}$  lateral resolution over a large working distance (i.e. up to 5 mm from the distal end of the probe). The dynamic focus capability allows integration of the endoscopic probe to GD-OCM imaging to achieve high resolution endoscopic tomograms.

We envision the future of this developing technology as a solution to high resolution, minimally invasive, depth-resolved imaging of not only structure but also the microvasculature of *in vivo* biological tissues that will be useful for many clinical applications, such as dermatology, ophthalmology, endoscopy, and cardiology. The technology is also useful for animal study applications, such as the monitoring of an embryo's heart for the development of animal models and monitoring of changes in blood circulation in response to external stimulus in small animal brains.

To my parents Jan and Jamnean Meemon

To my beloved wife Meow

To my family



## ACKNOWLEDGMENTS

First of all, I would like to give my grateful thank to my advisor, Dr. Jannick P. Rolland, who has been a lovely advisor, a great teacher, a cheerful guide, and an inspiration not just for my research but for every aspect of my living. To me, she is not only my advisor but also my parent when I have been far away from home. I would like to thank my dissertation committee, Dr. Peter Delfyett, Dr. Martin Richardson, and Dr. Hassan Foroosh not only for their interest in this research but also for their fruitful comments, suggestions, and discussions throughout the progress of this dissertation.

This work could not be completed without inputs from these excellent people; Prof. Harrison Barrett at the University of Arizona for stimulating discussion about the Gabor-based fusing technique, Dr. Kevin Hsu of Micron Optics Inc. for his partnership in the development and excellent technical support and service on a custom designed broadband frequency swept light source that has been used in all Doppler OCT experiments, Dr. Martin Leahy at University of Limerick and Anjul Davis of Thorlabs for their stimulating discussion about Doppler imaging, Dr. Lisa DeLouise, Department of Dermatology at the University of Rochester Medical Center, for providing the ex vivo human skin sample for GD-OCM, Dr. Miguel A. Alonso at University of Rochester for his input on the mathematical derivations of FD-OCM and GD-OCM, Dr. Kevin P. Thompson for a discussion about the optical design of the dynamic focus catheter. I must also acknowledge Optical Research Associates (ORA) for the educational license of Code V<sup>TM</sup> that was used for the optimization of the catheter.

Moreover, I would like to gratefully acknowledge the Florida Photonics Center for Excellence (FPCE), the I<sup>2</sup>lab Foundation at the University of Central Florida, James and Esther King Biomedical Research Program, Photonics Technology Access Program (PTAP) sponsored by the Defense Advanced Research Projects Agency and National Science Foundation (DARPA & NSF), and New York State Foundation for Science, Technology, and Innovation (NYSTAR) for funding this research. I would like to give my special thank to the Royal Thai Government Scholarship from 2005 to 2010 for providing me such a great opportunity to pursue my doctoral research. Without them, this research would have never been possible.

My life would be miserable without these beautiful and cheerful people around me over the past five years away from home. I thank every ODALab members: post docs, alumni, current students, visitors, and interns for their friendship as well as their direct and indirect inputs to this work. Especially, I would like to thank my OCT team members —Kye-Sung Lee and Supraja Murali— for support and help they have provided. It is my pleasure to have a chance to work with them. I would like to thank also the faculty at CREOL, the College of Optics and Photonics, for their great work on teaching and advising that provided me a strong background on optics. I would like to sincerely thank the staff both at CREOL and the Institute of Optics at University of Rochester (in particular Rachel Franzetta and Gina Kern) for services and supports on administrative procedures, travel, purchasing etc. I would like to mention my classmates and friends at CREOL for making my study and campus life enjoyable. I thank Michelle Ver Way at the International Service Center at UCF for taking care of my immigration documents over these five years of my abroad study. I thank all my Thai friends both in the USA and in Thailand for

their friendship and support. I would like to thank also the staff at the Office of Educational Affairs and the Royal Thai Embassy in Washington DC for every help, service, and consult that they have provided me since the time I arrived in the USA.

My very special thanks go to my family; my parents —Jan and Jamnean Meemon—, my sisters and my nieces for their love, unconditional supports, encouragement, and sacrifice, and particularly to my beloved wife —Meow— for her patience, support and endless love and for being the source of joy and happiness in my life.

## TABLE OF CONTENTS

LIST OF FIGURES .....	xv
LIST OF TABLES .....	xxii
LIST OF ACRONYMS/ABBREVIATIONS.....	xxiii
CHAPTER ONE: INTRODUCTION.....	1
1.1    Introduction to Medical Imaging.....	1
1.2    Optical Coherence Tomography.....	3
1.3    Motivation.....	6
1.4    Research Summary .....	9
1.5    Dissertation Outline .....	11
CHAPTER TWO: LITERATURE REVIEW.....	13
2.1    Frequency Domain OCT.....	13
2.2    Complex Conjugate Ambiguity in FD-OCT.....	18
2.3    Full-Range FD-OCT .....	22
2.4    Optical Coherence Microscopy .....	28
2.5    Endoscopic OCT .....	31
2.6    Doppler OCT.....	34
2.7    Summary .....	46
CHAPTER THREE: VARIABLE VELOCITY DYNAMIC RANGE DOPPLER OCT.....	49
3.1    Swept-Source OCT System.....	49

3.1.1	System Configuration.....	49
3.1.2	MZI Calibration Curve.....	52
3.1.3	System Sensitivity.....	54
3.1.4	Volumetric Imaging with SS-OCT.....	55
3.2	Phase-Resolved DOCT.....	56
3.3	Method for Multi-VDR DOCT.....	63
3.4	Phase Stability of Multi-VDR DOCT.....	66
3.5	<i>In vivo</i> Imaging with Multi-VDR DOCT.....	70
3.6	Summary.....	74
CHAPTER FOUR: DUAL DETECTION FULL RANGE FD-OCT.....		75
4.1	Two Steps Phase Shifting Method.....	75
4.2	The Implementation of DD-FD-OCT.....	78
4.2.1	Free-Space DD-FD-OCT.....	78
4.2.2	Hybrid DD-FD-OCT.....	81
4.3	Results and Discussion.....	84
4.3.1	System Performances.....	84
4.3.2	In Vivo Imaging of Biological Sample with DD-FD-OCT.....	85
4.4	Summary.....	87
CHAPTER FIVE: DOPPLER IMAGING WITH DD-FD-OCT.....		88
5.1	Introduction.....	88
5.2	Experimental Method.....	90

5.2.1	Doppler Phase Shift Determination .....	90
5.2.2	Flow Phantom and Pumping System .....	92
5.3	Results and Discussion .....	94
5.3.1	Phase Stability of the System .....	94
5.3.2	Phase Stability in the Presence of Noise .....	98
5.3.3	Flow Measurement Verification .....	100
5.4	Summary .....	106
CHAPTER SIX: GABOR DOMAIN OPTICAL COHERENCE MICROSCOPY .....		108
6.1	Mathematical Description of GD-OCM .....	108
6.2	GD-OCM Implementation .....	112
6.3	Gabor-Based Fusing Method .....	115
6.3.1	Fusing Algorithm .....	115
6.3.2	Imaging Speed .....	119
6.3.3	Fusing Results .....	119
6.4	Volumetric Imaging with GD-OCM .....	123
6.5	Summary .....	126
CHAPTER SEVEN: OPTICAL DESIGN OF DYNAMIC FOCUS CATHETER FOR ENDOSCOPIC GD-OCM .....		128
7.1	Optical Design of a Dynamic Focus Catheter .....	128
7.2	Effects of the Cylindrical Exit Window .....	132
7.3	As Designed Performance .....	134

7.4	Fabrication and Assembly Tolerances .....	134
7.5	Summary .....	135
CHAPTER EIGHT: SUMMARY AND FUTURE DIRECTION.....		137
8.1	Summary .....	137
8.2	Future Directions .....	141
LIST OF REFERENCES .....		145

## LIST OF FIGURES

Figure 2.1: Typical configurations of (a) spectrometer based FD-OCT and (b) swept-source based FD-OCT .....	14
Figure 2.2: A fiber ring configuration of the frequency swept light source proposed by Huber et al. Isolators were used to ensure unidirectional resonating and a booster SOA was used to improve the output power as well as the shape of the spectrum (Huber et al. 2005a).....	16
Figure 2.3: The configuration of a Fourier domain mode locking laser proposed by Huber et al. A dispersion managed delay was used to optically store an entire frequency sweep within the laser cavity. (Huber et al. 2006).....	17
Figure 2.4: Illustration of the depth-resolved reflectivity profile achieved by inverse Fourier transform of the detected spectral interference (a) with and (b) without overlapping. ....	21
Figure 2.5: Example of mirror image in conventional FD-OCT.....	22
Figure 2.6: The processing algorithm to achieve the full-range depth profile in (Zhang et al. 2004).....	26
Figure 2.7: Processing diagram of the BM-scan method where (A) is a frame of acquired modulated spectra, and (B) is the 1st Fourier transform along the time axis (lateral direction), in which the band-pass filter is applied to filter out the negative frequency components. An inverse Fourier transform is then performed yielding complex spectral interference signals that give a mirror-free image in (C) after a Fourier transform in the $k$ -domain (Jaillon et al. 2010). ....	27



Figure 2.8: Examples of (a) B-Mode intensity map, (b) B-Mode Doppler map, (c) M-Mode intensity map, and M-Mode Doppler map (Mariampillai et al. 2007).	35
Figure 2.9: Illustration of OMAG algorithm	37
Figure 2.10: Illustration of STdOCT algorithm (Szkulmowski et al. 2009).	39
Figure 2.11: (a) The configuration of the dual-angle Doppler measurement; (b) The configuration within the sample arm optics (Dave and Milner 2000).	42
Figure 2.12: The illustration of dual incident angles encoded in the different path lengths (Pedersen et al. 2007)	43
Figure 2.13: The experimental setup of dual-beam, dual-angle FD-DOCT (Iftimia et al. 2008)	44
Figure 2.14: The configuration of Doppler angle determination utilizing dual-plane measurement (Wang, Y. et al. 2007)	45
Figure 2.15: A flow angle measurement using 3D flow segmentation technique (Davis et al. 2008)	46
Figure 3.1: The fiber-based swept-source OCT built on Mach-Zehnder interferometer; PD = photo-detector, Cir = circulator, and PC = polarization controller	50
Figure 3.2: An <i>en face</i> image acquired over about 4 mm x 4 mm field of view of a calibrated resolution target, where the number of line-pairs per millimeter (lp/mm) and the corresponding lateral resolution in parenthesis of several groups of the target are provided in the red boxes.	51

Figure 3.3: (a) The example of an interference signal acquired by an unbalanced MZI; (b) the portion of the MZI signal marked by a red dash box in (a); (c) a calibration curve extracted from peaks, valleys, and zero-crossing position of the MZI signal. ....53

Figure 3.4: Time encoded spectral interference (a) as detected by the photo-receiver and (b) after calibration to linear frequency using the MZI curve in Figure 3.3(c). ....53

Figure 3.5: Measured SNR as a function of depth (a) without a booster and (b) with a booster amplifier.....55

Figure 3.6: A volumetric imaging of an African frog tadpole using the developed SS-OCT system. Image was rendered with Voxx software developed by the School of Medicine at Indiana University. ....56

Figure 3.7: An illustration of the flow angle respective to the incident beam direction.....58

Figure 3.8: Example of acquired spectra consisting 5 sweep cycles .....64

Figure 3.9: Illustration of the Doppler phase stability measurement; (a) Doppler image; (b) Intensity image; (c) zoom-in of the intensity image in (b); (d) axial profile of the intensity image in (c). ....67

Figure 3.10: An example of histogram distribution of the measured phase shift along with the corresponding Gaussian fitted curve (red dash line) for the case of (a)  $p = 1$  and (b)  $p = 6$ ; The horizontal axis is the phase shift error in mrad. ....68

Figure 3.11: Doppler images of an African frog tadpole that were simultaneously acquired at the same location at different times where (a, d, g, and j) are intensity images, (b, e, h, and k) and (c, f, i, and l) are Doppler images corresponding to  $p = 1$  and  $p = 4$ , respectively. ....72

Figure 3.12: (a) Conventional intensity image, (b) fast-flow Doppler image, and (c) slow-flow Doppler image acquired at the same location of the tadpole heart region. ....	73
Figure 4.1: A $\pi/2$ phase shift deviation across the spectral range .....	77
Figure 4.2: (a) A free-space DD-FD-OCT setup and (b) Adjustment of NPBS2 to obtain $\pi/2$ phase shift between the two interference signals (Lee et al. 2010a).....	80
Figure 4.3: A-scan depth profiles of a single reflector in the sample arm (a) with single detection and (b) with suppression of the complex conjugate peak of 35 dB in the DD-FDOCT (Lee et al. 2010a). ....	81
Figure 4.4: (a) The experimental setup of DD-FD-OCT in a hybrid MZI setup. FC: fiber coupler, PC: polarization controller, BS: beam splitter, COL: collimator, M: mirror, GM: galvo mirror, MZI: Mach-Zehnder interferometer, OBJ: Objective, CIR: circulator, FOC: focuser, and BD: balanced detector. (b) The photograph of the free-space section with red arrows indicates optical paths from reference and sample out-couplers to each balanced detector. ....	82
Figure 4.5: (a) Two spectra with quadratic phase relation simultaneously acquired by the dual detection system when imaging a single reflector; (b) A depth profile demonstrates the suppression performance of DD-FD-OCT that corresponds to a case of matching amplitudes of the signals shown in (a) within 2%. ....	85
Figure 4.6: <i>In vivo</i> full-range images taken from a <i>Xenopus Laevis</i> tadpole by using conventional FD-OCT (left) and DD-FD-OCT (right) .....	86
Figure 4.7: <i>In vivo</i> image of a human finger joint taken by conventional FD-OCT (left) and full-range DD-FD-OCT (right).....	86

Figure 5.1: Illustration of the flow phantom and pumping system.....	93
Figure 5.2: Histogram distributions of measured Doppler phase errors where left (a,c) and right (b,d) columns correspond with the measurement data taken with conventional FD-OCT and DD-FD-OCT, and top (a,b) and bottom (c,d) rows correspond with B-mode and M-mode operations, respectively; The measurements were conducted at different values of $M$ . The filled square markers and the solid lines represent measurement values and the Gaussian fit, respectively. ....	96
Figure 5.3: Average phase errors measured from stationary diluted milk when the sample surface was placed at different depth positions by changing the optical path length in the reference, where the white dash box indicates the area that the phase error was averaged over in each case, and the orange dash line denotes the zero-delay position. ....	98
Figure 5.4: Measured SNR (in air) of the system as a function of depth. ....	99
Figure 5.5: (a) and (d) are intensity images, (b) and (e) are B-mode Doppler images, and (c) and (f) are M-mode Doppler images measured by conventional FD-OCT and DD-FD-OCT, respectively, where the yellow horizontal dash line indicate the zero path delay position, the white vertical dash line indicates the lateral position where the M-mode Doppler was operated, and the white solid line at the bottom right of (d) denotes the scale bar that is applied to all images (a-f). ....	101
Figure 5.6: M-mode Doppler images calculated from the full-range signal at various flow velocities set by the pump.....	103

Figure 5.7: Plots of the measured velocity at the peak of the flow profile and the set flow velocity measured by conventional FD-OCT (left) and full-range DD-FD-OCT (right). 200 measurements were performed at each set flow velocity. Each data point corresponds to a mean value, and the size of the error bar at each measurement point represents the FWHM of the distribution of the measured Doppler phase shift estimated by  $2.36\sigma$  assuming a Gaussian distribution. .... 104

Figure 5.8: (a) and (b) are intensity images and (c) and (d) are corresponding Doppler images of the heart of an African frog tadpole processed with and without full-range enabled, respectively. The white arrow in (b) indicates the location of the flow activity displayed in (d). .... 106

Figure 6.1: An experimental setup for GD-OCM..... 113

Figure 6.2: Flow diagram of the imaging procedure of GD-OCM..... 114

Figure 6.3: Acquired images or GD-samples after Fourier transform and logarithmic intensity mapping ..... 115

Figure 6.4: Flow diagram of adaptive weighting windows construction..... 117

Figure 6.5: Mathematical definition of the window for Gabor domain OCM ..... 118

Figure 6.6: (a) OCM Images of an African Frog Tadpole (*Xenopus laevis*) each acquired with the optics focused every 100  $\mu\text{m}$  apart in depth from 0 to 0.5 mm; the white arrow points to a dominant feature (b) A plot of each window profile superimposed on top of an averaged reflectivity profile (c) Filtered images (d) The filtered images were then summed using a Gabor-based fusion algorithm. .... 120

Figure 6.7: (a) Sub-cellular resolution cross-sectional imaging of an African frog tadpole acquired by GD-OCM (b) in comparison, an image acquired by FD-OCM with the same custom objective.....	121
Figure 6.8: GD-OCM imaging of fat cells of an <i>ex vivo</i> human skin sample covering a 2 mm lateral field of view.....	122
Figure 6.9: <i>In vivo</i> GD-OCM images of human skin taken from a nail fold (top) and a finger joint (bottom) .....	123
Figure 6.10: A volumetric image of the fat cells of an <i>ex vivo</i> skin acquired by GD-OCM.....	124
Figure 6.11: A cut portion of the 3D data displayed in various angles.....	125
Figure 6.12: (a) volumetric rendering of <i>in vivo</i> human finger skin acquired by high speed GD-OCM; (b) <i>En face</i> images extracted from every 20 $\mu\text{m}$ along the axial direction of the fused 3D dataset. ....	126
Figure 7.1: The catheter design layout .....	129
Figure 7.2: Response times of the liquid lens at different repetition rates (Lee et al. 2010b).....	130
Figure 7.3: The ray aberration curves at arbitrary focus (a-d) plotted within $\pm 10 \mu\text{m}$ maximum scale. The chromatic aberration was optimized at the working distances of 0.5, 1.5 and 3 mm; a slight degradation is observed at a distance of $\sim 4.5 \text{ mm}$ from the exit window ...	131
Figure 7.4: Lateral point spread function (PSF) and Strehl ratio (SR) throughout the working range (a) without the cylindrical microlens and using an already ultrathin 50 microns window thickness, and (b) with a cylindrical microlens and a 500 microns window thickness. ....	133

## LIST OF TABLES

Table 3-1 Quantification of detectable velocity range corresponds to each value of $p$ .....	70
Table 5-1 The minimum detectable axial velocity at various $M$ values, where the top (without parenthesis) and bottom (in parenthesis) values in each cell correspond to B-mode and M-mode Doppler imaging, respectively.....	97
Table 7-1 Design specification .....	130
Table 7-2 Dynamic focusing performance throughout the working range i.e. lateral resolution as determined by convolution of two PSFs, averaged MTF at 100 cycles/mm, and SR at best focus. ....	134
Table 7-3 Fabrication and assembly tolerance analysis .....	135

## LIST OF ACRONYMS/ABBREVIATIONS

1D	One Dimension
2D	Two Dimensions
3D	Three Dimensions
BW	Bandwidth
CCD	Charge-Couple Device
CMOS	Complementary Metal–Oxide–Semiconductor
CT	Computed Tomography
DF	Dynamic Focus
DOCT	Doppler Optical Coherence Tomography
DOF	Depth of Focus
DD-FD-OCT	Dual Detection Frequency Domain Optical Coherence Tomography
EO	Electro-Optics
EOCT	Endoscopic Optical Coherence Tomography
FD-DOCT	Frequency Domain Doppler Optical Coherence Tomography
FD-OCT	Frequency Domain Optical Coherence Tomography
FD-ODL	Fourier Domain Optical Delay Line
FDML	Fourier Domain Mode Locking
FFP-TF	Fiber Fabry-Perot Tunable Filter
FFT	Fast Fourier Transform



FWHM	Full-Width at Half-Maximum
GD-OCM	Gabor Domain Optical Coherence Microscopy
HWHM	Half-Width at Half-Maximum
LCI	Low Coherence Interferometry
MEMS	Micro-Electro-Mechanical Systems
MRI	Magnetic Resonance Imaging
MTF	Modulation Transfer Function
MZI	Mach-Zehnder Interferometer
NA	Numerical Aperture
OCM	Optical Coherence Microscopy
OCT	Optical Coherence Tomography
OLCR	Optical Low-Coherence Reflectometry
OMAG	Optical microangiography
PC	Polarization Controller
PR-DOCT	Phase-Resolved Doppler Optical Coherence Tomography
PSF	Point Spread Function
PSI	Phase-Shifting Interferometry
ROI	Region of Interest
RSOD	Rapid Scanning Optical Delay-line
SNR	Signal to Noise Ratio
SOA	Semiconductor Optical Amplifier

SR	Strehl Ratio
SS-OCT	Swept Source Optical Coherence Tomography
STdOCT	joint Spectral and Time domain Optical Coherence Tomography
STFT	Short Time Fourier Transform
TD-OCT	Time Domain Optical Coherence Tomography
TD-DOCT	Time Domain Doppler Optical Coherence Tomography
VDR	Velocity Dynamic Range

## **CHAPTER ONE: INTRODUCTION**

Chapter one begins with a brief introduction to various medical imaging modalities. Then, the concept and basic principle of optical coherence tomography is explained. Finally, the motivation and summary of the research as well as the dissertation outline are presented.

### **1.1 Introduction to Medical Imaging**

Medical imaging technology has been developed since the invention and use of the optical microscope in the early 1600s. The inventor of the first optical microscope is not definitively known. However, it is usually attributed to Dutch spectacle-makers Hans Janssen and his son Zacharias Janssen at the end of 16<sup>th</sup> century, and to Galileo in 1610 (Abramowitz et al. 2009). The instrument operates in visible light and uses lenses to magnify images of very small objects that are not visible to the naked eye. However, it provides neither *in vivo* imaging nor depth perception. In 1895, William Roentgen discovered X-rays that are capable of revealing the skeletal system as well as enabling the detection of diseases in some soft tissues including lungs, intestines, and kidneys.

The development of modern computer technology in the 1960s led to the invention of X-ray Computed Tomography (CT) in the 1970s (Kalender 2006), which was introduced into clinical practice in 1979 (Hounsfield 1992). Nevertheless, the X-rays still have some limit in imaging soft tissue due to the fact that they normally pass through the tissue without significant

change. Furthermore, they provide radiation to the patient, which can damage healthy tissue and organs.

Even though ultrasonography had been introduced in medical applications before the invention of CT, it has only recently been fully developed and widely used. Medical ultrasonography has the ability to image soft tissue properties. It has been widely studied, developed, and has been used in various clinical applications (Erikson et al. 1974).

In the 1970s, Magnetic Resonance Imaging (MRI) was invented. It enables structural and functional imaging with high spatial resolution and with no penetration limit. However, these advantages come with high cost and complexity as well as slow data acquisition speed compared to other techniques (Broady and Gooding 1986). In addition, MRI requires large magnets that are not easily deployed or moved.

In recent years, optical imaging techniques have gained more interest as they show promise for various medical applications because of their focus on high sensitivity and high resolution, while being able to provide non-ionizing and safe radiation. In addition, optical diagnosis is often portable or deployable. The confocal microscope is an instrument that offers sub-micron spatial resolution, which allows the visualization of cell structures, by removing out-of-focus background noise through a pinhole device placed in front of a detector (Minsky 1961). Although this instrument provides high lateral resolution, it usually has poor axial resolution, and its depth scanning range is limited to only a few hundred microns.

Another technique, fluorescence imaging is based on the interaction of light, at a specific wavelength, with fluorophores in a target sample. Fluorescence microscopy was first attempted

by Kohler and Seidentopf in 1908 and the first fluorescence imaging was successfully demonstrated by Lehmann in 1910 (Rost 1995). A single fluorophore is typically used to mark a single molecular species. An emission filter is used to separate illumination light from much weaker emitted fluorescence. By combining confocal microscopy with fluorescence imaging, three dimensional (3D) reconstruction can be achieved by recording a series of *en face* images along the z-axis. Nevertheless, depth penetration is limited since it requires a specific and strong fluorescence signal (Liu and Chiang 2003). In order to enhance penetration depth as well as reduce photo damage and allow imaging of living specimens, two-photon and multiphoton fluorescence microscopes were invented (Denk et al. 1990; So et al. 2000).

## 1.2 Optical Coherence Tomography

In early 1991, Optical Coherence Tomography (OCT), a new imaging method with micrometer resolution and cross-sectional imaging capabilities, was introduced (Huang et al. 1991). OCT has the capability of performing real time *in vivo* high resolution imaging of microstructures by measuring the light intensity reflected from within the sample. Despite its lateral resolution, which is typically lower than a confocal microscope, it provides higher axial resolution given a broadband light source and a deeper penetration depth because the coherence gating enables further rejection of multiple scattering compared with confocal gating. Consequently, OCT has critical advantages over other medical imaging techniques given its relatively low-cost, noninvasive nature, and the capability of performing *in vivo* high resolution cross-sectional imaging of microstructures in real time.

Conventionally, OCT is based on low-coherence interferometry (LCI) that takes advantage of the short coherence length of broadband light sources, which is in the order of microns, to achieve precise depth sectioning in scattering media. In 1987, Davidson et al. presented the use of LCI for the application of integrated circuit inspection (Davidson et al. 1987). The use of LCI to determine the axial length of human eyes *in vivo* was proposed by Fercher et al. in 1988 (Fercher et al. 1988), and further improved by Hitzenberger in 1991 (Hitzenberger 1991). Later, a group of scientists at MIT led by Fujimoto pioneered the use of LCI to generate tomographic images of biological samples, which served as the first OCT system (Huang et al. 1991). OCT can be performed by fixing a sample of interest in one arm of the LCI, referred to as the sample arm, and placing a scanning mirror into the reference arm. The OCT system that acquired a sample depth profile by scanning the reference mirror is referred to as time domain OCT (TD-OCT).

The interference signal acquired by OCT is equivalent to an optical sampling of the sample reflectivity along the depth by using the low coherence of a broadband light source as a sampling gate (Fercher et al. 2003). Hence, the envelope of the temporal coherence serves as an axial point spread function (PSF). For a Gaussian spectral distribution assumption, the axial resolution  $\Delta z$  is given as

$$\Delta z = \frac{2 \ln 2}{\pi} \left( \frac{\lambda_0^2}{\Delta \lambda} \right), \quad (1.1)$$

where  $\lambda_0$  is the source central wavelength, and  $\Delta z$  and  $\Delta\lambda$  are the full width at half-maximum (FWHM) of the autocorrelation function and the power spectrum bandwidth of the light source, respectively (Born and Wolf 1999; Bouma and Tearney 2002). Ackay et al. studied the effect of non-Gaussian spectral shape to the degradation in axial resolution of OCT, in which the method of spectral shaping to achieve axial resolution close to the theoretical limit was presented (Ackay et al. 2005). In addition to a broad spectral characteristic, an OCT light source should provide sufficient illumination power to penetrate deep inside the sample (typically 2 to 3 mm). Moreover, the center wavelength of the light source is usually selected to yield optimum absorption and backscattering that is between 800-1300 nm for biological samples (Bouma and Tearney 2002; Fercher et al. 2003).

Separately, the lateral resolution is governed by a lateral PSF of an imaging lens in the sample arm. The lateral resolution can be estimated using the Rayleigh resolution criterion as

$$\Delta x = 1.22 \frac{\lambda_0}{NA}, \quad (1.2)$$

where  $NA$  is the numerical aperture of the objective lens (Born and Wolf 1999). The lateral resolution, therefore, can be improved by increasing the  $NA$  of the objective. Nevertheless, there is a trade-off between the lateral resolution and the depth of focus (DOF) since the lateral resolution is proportional to  $NA^{-1}$ , while the DOF is proportional to  $NA^{-2}$ . Consequently, a typical OCT system uses low  $NA$  objectives to achieve sufficient DOF, e.g.  $\sim 2$  mm in dense tissue, at the cost of low lateral resolution of often up to 20  $\mu\text{m}$ .

Synchronously with the axial scan, a lateral scan can be performed either by scanning the focusing beam or laterally moving the sample itself. Combining the axial and lateral scan, a cross-section image can be constructed. A 3D volumetric imaging can also be achieved by collecting multiple cross-section images acquired at different scanning planes (Huber et al. 2005b).

### 1.3 **Motivation**

OCT provides non-invasive high resolution cross-sectional imaging filling the resolution gap between microscopy and ultrasound imaging. Conventionally, OCT utilizes the depth-resolved backscattering amplitude as a contrast mechanism, providing cross-sectional mapping of the sample structure. However, the back-reflection magnitude alone may not provide sufficient information. Therefore, an extra contrast mechanism is necessary in order to gather enough information for decision making particularly in the field of medical diagnostics.

One of the useful information for diagnostics is blood flow property. Doppler OCT (DOCT) is capable of *in vivo* detection of flow activity embedded beneath the surface of a fairly thick biological sample in high resolution and wide velocity dynamic range. DOCT allows visualization of tissue structure and blood flow activity that provides important information for clinical diagnostics. For example, vessel flow property is an early indicator of many retinal pathologies such as glaucoma, diabetes, and age related macular degeneration (Wang et al. 2009). Moreover, detailed knowledge of *in vivo* blood flow under the skin surface is useful for burn-depth determination and port wine stains treatment (Nelson et al. 2001).



Furthermore, the ability to monitor the blood flow dynamics *in vivo* can open a window to the cardiovascular system since blood circulation is directly related to heart activity. The capillary network is only one cell in wall thickness with 5 to 10 microns in diameter and located in the dermis region of skin that is accessible from various parts of the human body (Murali 2009). However, since the Doppler sensitivity highly relies on the SNR of the imaging system, a high sensitivity OCT system is desired when imaging blood flow inside a dense tissue such as skin, in which the depth penetration is limited and the backscattering strength rapidly drops along the depth.

Frequency domain OCT (FD-OCT) provides speed and sensitivity advantage over TD-OCT. However, two main challenges in FD-OCT are the sensitivity fall-off caused by a finite spectral resolution and the existence of the complex conjugate signal known as mirror image that is intrinsic in the Fourier transformation of a real signal. Conventionally, to avoid structural ambiguity caused by a mirror image, two conjugate signals are completely separated into positive and negative planes and only half of the transformed plane is used to form an image. This prohibits the usage of the region around the zero path-delay that is known to be the most sensitive region in FD-OCT.

One known solution that allows efficient usage of the given SNR of each FD-OCT system is by implementing a full-range FD-OCT. The full-range FD-OCT is a technique of reconstruction of a complex spectral interference signal from a set of measurable signals prior to the Fourier transformation. The combination of Doppler imaging and full-range FD-OCT is

expected to improve the Doppler detection since the usable imaging depth range is doubled and the most sensitive region (i.e. at around the zero-delay position) can be used for imaging.

In addition, as a result of the large effort put forth by the scientific and industrial community to develop broader and broader source spectra, OCT has achieved (since the mid 1990s) remarkable axial resolution, starting in 1995 with mode-locked solid state lasers (Bouma et al. 1995) and recently with supercontinuum sources (Aguirre et al. 2006; Cimalla et al. 2009). To achieve quasi-invariant lateral resolution over an imaging depth range of  $\sim 2$ -3 mm, which corresponds to the depth penetration limit of OCT imaging, conventional OCT utilizes low NA imaging optics (e.g.  $NA < 0.1$ ) that provides quasi-invariant lateral resolution in the range of 10 to 30  $\mu\text{m}$ . By using a higher NA objective in the sample arm (i.e.  $NA = 0.4$ ), the first demonstration of high lateral resolution associated with the terminology of Optical Coherence Microscopy emerged in 1994 (Izatt et al. 1994).

Consequently, ultrahigh-resolution OCT was first demonstrated *in vivo* in 1999 with simultaneously up to  $\sim 1$   $\mu\text{m}$  axial resolution in tissue and 3  $\mu\text{m}$  lateral resolution (Drexler et al. 1999). Nevertheless, the high lateral resolution achieved by simply opening the NA comes with the expense of a severe reduction in DOF. To overcome the decrease in DOF that varies as the inverse square of the NA, the concept of dynamic focusing was introduced (Schmitt et al. 1997). Since then, an open challenge has been to achieve high lateral resolution over a large imaging depth range as well as at sufficient speed capable for *in vivo* imaging, because it is only then that one can open a path for *in vivo* clinical applications seeking histology grade image quality.

Finally, to enable new imaging capabilities and performances, custom optical design is only a matter of time called upon.

In recent years, the use of OCT in endoscopy so-called *endoscopic OCT* has gained more interest. In endoscopic OCT, one of the main challenges is the design of a high resolution endoscopic probe. Most catheters designed for endoscopic OCT use a fixed focus objective lens and hence have a fixed focal plane relative to the distal end of the probe. Therefore, the location of the probe relative to the sample surface is critical, particularly when combining with FD-OCT. Commercial endoscopic OCT probes utilize low NA optics to achieve a large working distance of the probe. For high resolution OCT however, the use of high NA optics is essential. As a result, the position of the catheter has to be precisely located so that the region of interest is placed within the DOF of the probe. For imaging inside the human body, the registration between the DOF of the probe and the area of interest could be difficult, if not possible.

#### **1.4 Research Summary**

The purpose of this research is to develop functional OCT systems that are useful for diagnostic applications. The research is divided into two main topics. The first part of the research focuses on the improvement in the stability, sensitivity, and imaging speed as well as detectable velocity dynamic range of swept-source based DOCT. The second part is the development of an ultra high resolution OCT called Gabor domain OCM (GD-OCM) focusing on the development of an automatic algorithm for image fusion to accommodate for real time *in vivo* imaging and display of the proposed technology.

One of the most important factors in Doppler detection is the ability to detect a wide range of flow velocity. DOCT is capable of the detection of Doppler phase shift only along the direction of the illumination beam (i.e. axial flow velocity). However, when imaging blood flow in biological samples, variation in the flow angles respective to the direction of the illumination produces a wide dynamic range of axial flow velocity. This dissertation presents a technique of multiple velocity dynamic range for phase-resolved DOCT that is capable of the detection of a wide velocity dynamic range in real time. The technique extends the minimum detectable velocity for a given phase stability of a DOCT system through the variation of acquisition time interval in real time. The proposed technique extends the lower limit of the velocity dynamic range while maintaining the maximum detectable velocity and hence increases the overall velocity dynamic range of a given DOCT system. The developed acquisition technique also provided high phase stability as compared with those reported in the literature. The improvement in detectable velocity dynamic range of about three to five times of a typical achieved value in the literature was achieved. The technique is particularly useful for high speed frequency domain OCT (FD-OCT) where the acquisition time is extremely short and hence the ability to visualize the slow axial flow may be limited.

Furthermore, a swept-source based full range DD-FD-OCT was developed. DD-FD-OCT provides an OCT Doppler image with high sensitivity over a large imaging depth range. A full range DOCT is demanded when employing a broadband light source in a high speed imaging system where spectral resolution needs to be sacrificed. The spectral resolution governs the sensitivity fall-off in FD-OCT system, and therefore, limits the imaging depth range. The full-

range system allows the use of regions on both side of the zero delay position and hence doubles a usable imaging depth range. The region around the zero delay position also provides the highest signal-to-noise ratio that will improve Doppler detection when monitoring the flow activity inside biological samples.

Moreover, an image fusion technique for GD-OCM is detailed. The mathematical description as well as an experimental implementation is explained. GD-OCM provides a quasi-invariant high resolution ( $< 5 \mu\text{m}$ ) cross-sectional image not only in axial direction but also in lateral direction. This leads to a more precise interpretation of the tissue structures. Therefore, this technique is promising for diagnostic application particularly when combined with functional imaging techniques. In addition, the optical design of a dynamic focus catheter for endoscopic GD-OCM is presented. Endoscopic OCT offers axial depth perception with high sensitivity as well as high spatial resolution and allows imaging within tubular organs such as the vascular system, the gastrointestinal tract, the breast duct, and the urinary tract. In this dissertation, a dynamic focus catheter that is capable, by designed, of less than  $6 \mu\text{m}$  lateral resolution over the 5 mm scanning range with more than 0.8 strehl ratio was achieved.

## **1.5 Dissertation Outline**

The rest of the dissertation is organized in the following way:

Chapter 2 consists of a literature review of FD-OCT, full-range FD-OCT, optical coherence microscopy, endoscopic OCT, and Doppler OCT. The review focuses on

functionality, configuration, performance, and limitations of related OCT systems that have been proposed to date.

Chapter 3 presents the development of Doppler imaging implemented in a high speed swept-source based FD-OCT system utilizing a FDML laser. A new acquisition scheme and the modified Doppler phase shift determination method to extend the detectable velocity dynamic range of the system are detailed.

Chapter 4 details the development of full range FD-OCT in a dual detection configuration so called a Dual Detection FD-OCT (DD-FD-OCT). The principle of DD-FD-OCT will be described, and the full-range imaging performance in biological samples is presented.

Chapter 5 demonstrates the combination of the Doppler technique and the full range DD-FD-OCT. Doppler imaging of biological samples using the full range DD-FD-OCT is also demonstrated.

Chapter 6 explains the principle, mathematical description, real time fusing algorithm, and imaging protocol of GD-OCM technique. The *in vivo* cellular imaging of biological samples is demonstrated.

Chapter 7 presents an optical design of a dynamic focus catheter for endoscopic GD-OCM. The effect of a cylindrical window of the catheter on through focus lateral resolution is discussed. Finally, the by design performances of the catheter is presented.

Chapter 8 summarizes and discusses future direction of this research.

## CHAPTER TWO: LITERATURE REVIEW

This chapter reviews the achieved advancements as well as limitations in FD-OCT, optical coherence microscopy, endoscopic OCT, and Doppler OCT; starting from, a detailed review of FD-OCT, followed by a discussion on the complex conjugate ambiguity in FD-OCT. Then, different proposed techniques of structural ambiguity removal in FD-OCT are reviewed. Finally, various techniques of extending depth of imaging in optical coherence microscopy are discussed as well as the key development and limitations in Doppler OCT.

### 2.1 Frequency Domain OCT

To date, there are two main different approaches of FD-OCT as shown in Figure 2.1. One is a spectrometer-based FD-OCT (Figure 2.1a), in which the sample is illuminated by a broadband light beam as in TD-OCT but the photodetector is replaced by a dispersive detector such as the combination of a grating and a linear detector array. Another approach is a swept-source based FD-OCT or swept-source OCT (SS-OCT) (Figure 2.1b), in which the sample is illuminated by a broadband frequency-swept light source and a photodetector is used to record the time-encoded spectral interference signal. Compared with TD-OCT, the most significant improvement is that a full depth profile can be immediately achieved by an inverse Fourier transformation of a single acquired spectral interference signal, without the scanning of the reference mirror as required in TD-OCT. In addition, the replacement of a single-element detector (i.e. photodetector) with a multi-element array detector, i.e. charge-couple device (CCD) camera, leads to the significant

reduction of shot noise. Therefore, not only the imaging speed but also the signal to noise ratio (SNR) is dramatically improved compared with TD-OCT (Choma, M. et al. 2003; De Boer et al. 2003; Leitgeb, R. et al. 2003b).

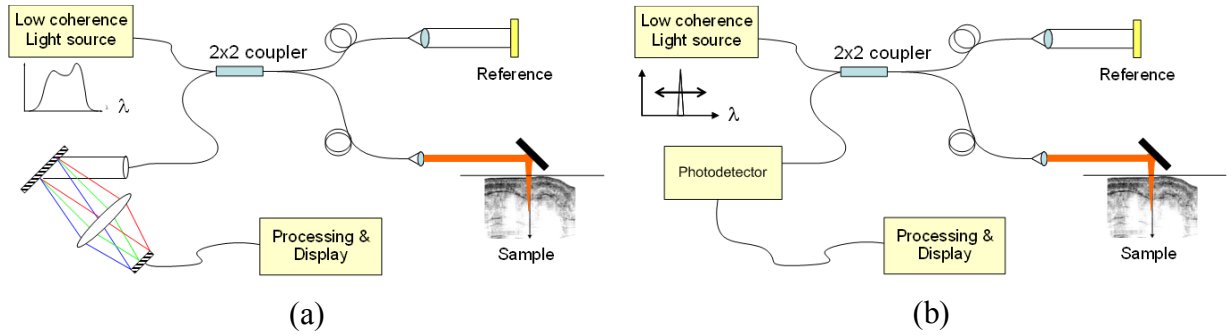


Figure 2.1: Typical configurations of (a) spectrometer based FD-OCT and (b) swept-source based FD-OCT

When the concept of FD-OCT was first introduced by Fercher in 1995, both tunable laser and spectrometer based configurations were presented. However, the measurement was demonstrated in one-dimensional (1D) eye length measurement through the spectrometer based setup using a 320 x 288 pixels photodiode array as a detector (Fercher et al. 1995). The technique stalled for many years due to the lack of high speed array detectors and high speed tunable laser as well as a high performance computer to handle the Fourier transform.

One of the important factors that lead to the breakthrough of a spectrometer based FD-OCT development is high speed CCD camera technology. Recently, Cense et al. reported a spectrometer based FD-OCT system capable of 29,300 spectra per second using a line-scan CCD camera (Cense et al. 2004). The movies of the human retina *in vivo* were demonstrated at 29.3 frames per second with 500 axial scans per frame. Another breakthrough point of a high speed



spectrometer based FD-OCT is the recent advance in the complementary metal-oxide-semiconductor (CMOS) technology. Potsaid et al. demonstrated the spectrometer based FD-OCT system at an acquisition speed as high as 312,500 spectra per second benefiting from the CMOS camera developed by Basler Vision Technologies. However, such high speed detection was achieved by illuminating the sample with a narrow bandwidth light source (27 nm FWHM, centered at 846 nm wavelength) and using only 576 camera pixels leading to an axial resolution of 8.7  $\mu\text{m}$  in tissue, sensitivity of 89 dB, and imaging depth range of 1.5 mm in tissue. The rapid volumetric imaging of 128 x 100 x 400 voxels was demonstrated at a speed of 250,000 axial scans per second corresponding with 0.08 second per volume (Potsaid et al. 2008).

Unlike the spectrometer based FD-OCT, swept-source based FD-OCT (SS-OCT) utilizes a frequency swept light source, and records the time-encoded spectral interference signal in a sequential manner by using a single element detector, such as a photodetector. This feature reduces the manufacturing cost because high performance CCD cameras, normally used in FD-OCT, are not required. Furthermore, a high speed frequency swept laser is also relatively low cost and portable as compared to a high performance broadband laser.

The first SS-OCT system was demonstrated in bulk optic design with a sweep rate of 10 Hz, which was not promising for high speed imaging in comparison with spectrometer based FD-OCT (Chinn et al. 1997). In recent years, many groups of researchers have reported a dramatic improvement in the imaging speed of SS-OCT. One of the key advancement in SS-OCT is the use of fiber ring laser geometry consisting of a semiconductor optical amplifier (SOA) and a wavelength tunable filter as shown in Figure 2.2 (Huber et al. 2005a).

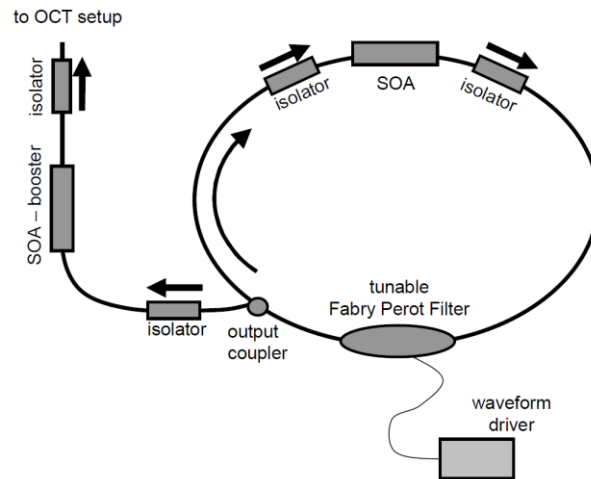


Figure 2.2: A fiber ring configuration of the frequency swept light source proposed by Huber et al. Isolators were used to ensure unidirectional resonating and a booster SOA was used to improve the output power as well as the shape of the spectrum (Huber et al. 2005a).

From Figure 2.2, the lasing started from spontaneous emission of the broadband SOA gain medium. The unidirectional isolating was achieved by using isolators. The broadband spontaneous emission was filtered by the high performance fiber Fabry-Perot tunable filter (FFP-TF) providing an output light with an extremely narrow line-width (e.g.  $\sim 0.135$  nm) around a specific wavelength corresponding with the tuning position of the filter. At each position of the filter, the filtered light was amplified through the process of amplified stimulated emission. The sweep rate of 20 kHz was achieved. The main factor that limits the sweep rate is that the lasing must built up from spontaneous emission at each new position of the filter.

Soon after the introduction of fiber-ring based frequency-swept light source, Huber et al. proposed an alternative scheme of frequency-swept laser, namely, Fourier Domain Mode Locking (FDML) as illustrated in Figure 2.3 (Huber et al. 2006). The main difference from the

previous fiber ring cavity is that, by adding a dispersion managed delay fiber, all modes of an entire sweep were simultaneously active in the resonator and the tunable filter was periodically tuned with a period matched to the round-trip time of the cavity or its harmonic. The light transmitted through a FFP-TF returned to the filter at a time when the filter was tuned to the same spectral position again. Therefore, it was not necessary for lasing to be built up from spontaneous emission as in the case of the previous approach. An effective sweep rate was up to 290 kHz. However, the imaging was demonstrated at a maximum of 232,000 axial scans per second, corresponding to 906 frames per second with 256 transverse pixels images, and 3.5 volume (256x128x128 voxels) per second.

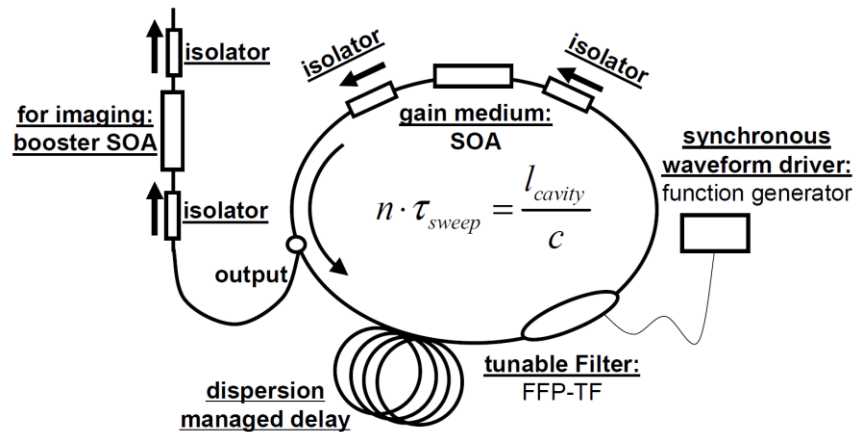


Figure 2.3: The configuration of a Fourier domain mode locking laser proposed by Huber et al. A dispersion managed delay was used to optically store an entire frequency sweep within the laser cavity. (Huber et al. 2006)

Even though the acquisition speed of FD-OCT has been dramatically improved during the past years, there are several challenges in FD-OCT that remains to be improved. For

example, the motion of the sample causes fringe washout in spectrometer-based FD-OCT (Yun et al. 2004). Consequently, a short exposure time is required, which may limit the system sensitivity and image contrast. In addition, for a given source bandwidth, the spectral resolution of the system (i.e. the number of pixels of the CCD camera in spectrometer-based FD-OCT and the spectral line width of the filter in SS-OCT) determines the axial depth range. The finite spectral resolution leads to the sensitivity fall-off across the axial measurement range (or depth range) (Leitgeb, R. et al. 2003b). This is because the larger the axial delays, the higher the loss in fringe visibility will be. Finally, one of the main challenges normally encountered in conventional FD-OCT is that it possesses an auto correlation noise and complex conjugate image that causes structural ambiguity known as *mirror image* or *ghost image*.

## **2.2 Complex Conjugate Ambiguity in FD-OCT**

The mirror image arises from the Fourier transformation of a real function in FD-OCT. Considering a typical FD-OCT system as shown in Figure 2.1(a), the spectral electric field propagating through the reference arm can be defined as

$$\hat{E}_R(k) = K_R \hat{E}_0(k) r_R \exp(ikl_R), \quad (2.1)$$

where the caret denotes a function in the frequency domain,  $k = 2\pi/\lambda$  is the wave propagation number,  $\hat{E}_0(k)$  represents the spectral electric field emitted from the light source,  $K_R$  is a real number representing total losses in the reference path,  $l_R$  is a round-trip optical path length

along the reference arm, and  $r_R$  is the reflectivity of the reference mirror. The spectral electric field from the sample arm is a collection of many backscattering events happening at various depths that can be modeled as

$$\hat{E}_S(k) = K_S \hat{E}_0(k) \int_{-\infty}^{+\infty} r(l_S) \exp(ikl_S) dl_S, \quad (2.2)$$

where  $K_S$  is a real number representing total losses in the sample path,  $l_S$  is a round-trip optical path length along the sample arm, and  $r_S(l_S)$  represents the sample reflectivity profile along the depth as a function of  $l_S$  (Wang and Wu 2007). Therefore, the spectral intensity as detected at the output of an interferometer can be expressed as

$$\hat{I}_D(k) = \left| \hat{E}_R(k) + \hat{E}_S(k) \right|^2, \quad (2.3)$$

$$\hat{I}_D(k) = \left| \hat{E}_0(k) \right|^2 \cdot \left( \begin{array}{l} \left| K_R r_R \right|^2 + 2K_R K_S r_R \int_{-\infty}^{\infty} r_S(l_S) \cos(k(l_S - l_R)) dl_S \\ + \left| K_S \int_{-\infty}^{\infty} r_S(l_S) e^{ikl_S} dl_S \right|^2 \end{array} \right). \quad (2.4)$$

The 1<sup>st</sup> term is regarded as DC-term that can be measured by blocking the signal from the sample arm and hence can be removed through the direct subtraction method. The 3<sup>rd</sup> term is an autocorrelation that is a collection of interference of backscattering signals from different depths in the sample arm. When imaging biological sample, the backscattering signal from the sample is usually much smaller than the reference signal (i.e.  $r_S \ll r_R$ ) and hence the 3<sup>rd</sup> term is relatively

weak compared with the 1<sup>st</sup> and 2<sup>nd</sup> terms so that it can be neglected. A strong autocorrelation from the sample arm can be removed by the subtraction method.

In OCT, only optical path length difference between sample and reference arms is of interest. By setting the optical path length difference  $l_D = l_S - l_R$  and assuming that the DC and auto-correlation terms (1<sup>st</sup> and 3<sup>rd</sup> terms) can be removed, the spectral interference signal can be expressed as

$$\hat{I}_{\text{int}}(k) = 2K_R K_S r_R \hat{S}(k) \cdot \int_{-\infty}^{\infty} r_S(l_D) \cos(kl_D) dl_D, \quad (2.5)$$

where  $\hat{S}(k) = |\hat{E}_0(k)|^2$  represents the power spectral density of the light source and  $r_S(l_D)$  is the sample reflectivity profile as a function of the optical path length difference  $l_D$ . Using the identity  $\cos(x) = \frac{1}{2}(e^{+ix} + e^{-ix})$ , Eq. (2.5) can be further expressed in a desired form as

$$\hat{I}_{\text{int}}(k) = K_R K_S r_R \hat{S}(k) \cdot \left[ \int_{-\infty}^{\infty} r_S(l_D) \exp(ikl_D) dl_D + \int_{-\infty}^{\infty} r_S(l_D) \exp(-ikl_D) dl_D \right], \quad (2.6)$$

Moreover, by defining the Fourier transform as  $\mathfrak{F}\{f(x)\} = \int_{-\infty}^{\infty} f(x) \exp(ikx) dx$  and using the

property  $f(-x) \stackrel{\mathfrak{F}}{\Leftrightarrow} F(-k)$  (Beyer 1991), Eq. (2.6) can be rewritten as

$$\hat{I}_{\text{int}}(k) = K_R K_S r_R \hat{S}(k) \cdot [\mathfrak{T}\{r_S(l_D)\} + \mathfrak{T}\{r_S(-l_D)\}]. \quad (2.7)$$

Consequently, the inverse Fourier transform of Eq. (2.7) is given by

$$I_{OCT}(l_D) = K_R K_S r_R \mathfrak{T}^{-1}\{\hat{S}(k)\} * [r_S(l_D) + r_S(-l_D)]. \quad (2.8)$$

Eq. (2.8) reveals that the sample reflectivity profile along depth can be achieved by the inverse Fourier transform of the measured spectral interference signal, where  $\mathfrak{T}^{-1}\{\hat{S}(k)\}$  serves as an axial point spread function. It also reveals that  $r_S(l_D)$  and  $r_S(-l_D)$  construct an even symmetric function as shown in Figure 2.4.

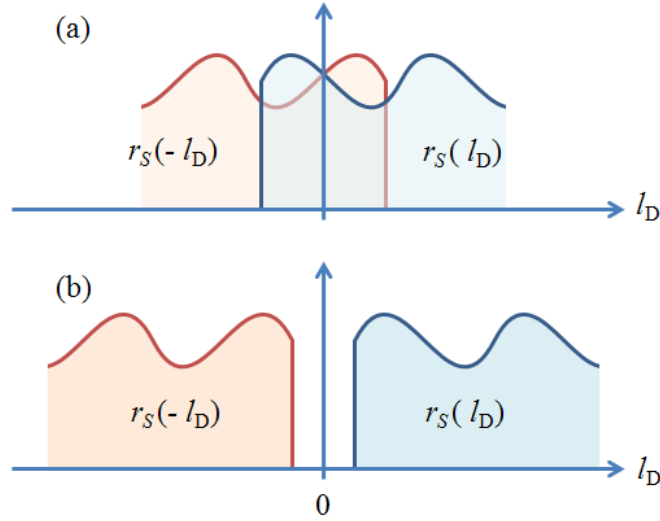


Figure 2.4: Illustration of the depth-resolved reflectivity profile achieved by inverse Fourier transform of the detected spectral interference (a) with and (b) without overlapping.

Nevertheless, only one of them is carrying usable information since they both contain the same information. Therefore, one of them is regarded as a mirror image that may cause confusion when both images are overlapped as shown in Figure 2.4(a). To avoid structural ambiguity, the reference position is usually set at above the sample surface causing the two signals to be completely separated as shown in Figure 2.4(b) and Figure 2.5, and only one half of the Fourier transformed signal is used to form an OCT image.

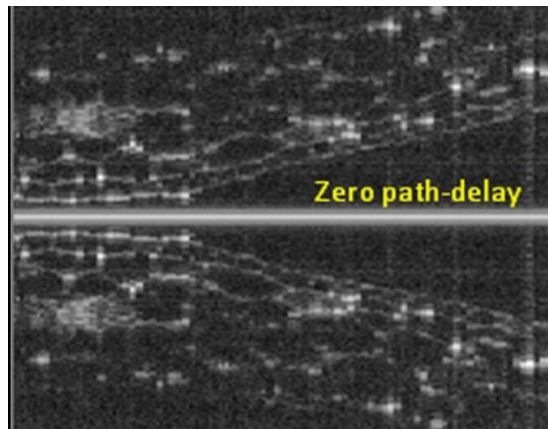


Figure 2.5: Example of mirror image in conventional FD-OCT.

### **2.3 Full-Range FD-OCT**

Using a moderate broadband light source, a typical OCT system is capable of axial resolution of about 10 to 20  $\mu\text{m}$ . The demand for higher axial resolution, e.g. in the order of a few microns or sub micron, requires the employment of an extremely broadband light source. However, achieving of high axial resolution at high acquisition speed requires the sacrifice of spectral resolution that eventually leads to reduction in an imaging depth range (Potsaid et al.



2008). For this reason, the removal of the mirror image in high resolution FD-OCT is desirable to double the usable imaging depth range. A system that is capable of removal of the mirror image and utilizing both positive and negative path-delay position for imaging is typically referred to as a *full-range FD-OCT*. Full-range FD-OCT also allows the use of the region around the zero path delay, where the sensitivity is maximum (Leitgeb, R. et al. 2003b). In the presence of the mirror image, this region cannot be fully utilized.

Based on the fact that the mirror image arises from the Fourier transform of a real function, most full-range FD-OCT techniques reported to date share the basic principle of reconstructing a complex spectral interference signal from measurable real signals. The complex spectral interference can be expressed as  $\tilde{F}(k) = A(k)\exp\{i\Psi(k)\}$ , where  $k = 2\pi/\lambda$  is the wave number, and  $A(k)$  and  $\Psi(k)$  are real functions representing magnitude and phase of the complex spectral interference  $\tilde{F}(k)$ , respectively.

The early attempts of full-range FD-OCT were based on the concept of phase-shifting interferometry (PSI), in which multiple interferograms with certain phase relation between them were sequentially acquired and used to determine the phase information of the complex interference signal (Carré 1966; Bruning et al. 1974; Wyant 1975). The concept of PSI was used to construct the complex spectral interference signal in FD-OCT by directly determining the phase term  $\Psi(k)$  of the spectral interference signal from a set of 3 to 5 acquired spectral interference signals (Wojtkowski et al. 2002; Targowski et al. 2004). However, the conventional phase-shifting method is subject to a reduction in imaging speed and hence is not suitable for *in*

*vivo* imaging. Furthermore, the accuracy of the phase steps limited the mirror image rejection performance of the technique. It was also highly sensitive to small movement of the sample.

To improve the imaging speed, the two-step phase-shifting method was proposed (Leitgeb, R. A. et al. 2003). The proposed method sequentially measured two spectral interference signals having  $\pi/2$  phase difference between them representing the real and imaginary components of the complex spectral interference (i.e.  $\tilde{F}(k) = F(k) + iF(k, \Delta\Psi = \pi/2)$ ). As a result, only two measurements were required at each lateral position. The sequential acquisition of two spectra caused a reduction in frame acquisition speed by half but was sufficient for *in vivo* full-range imaging. Nevertheless, it was extremely vulnerable to sample movement that occurs during the acquisition of the two spectra used to construct the complex signal. To overcome this limitation, several simultaneous detection schemes for the two-step phase-shifting method, such as the 3x3 coupler (Choma, M. A. et al. 2003; Mao et al. 2008), polarization-based demodulation (Vakoc et al. 2006), and dual-reference (Lee et al. 2009) techniques, were proposed.

The 3x3 coupler method utilized the inherent phase shifts of 3x3 fiber-optic couplers to extract the phase information of the complex interferometric signal. The phase information was determined from only two signals simultaneously obtained in the two detectors. However, the uneven wavelength dependent splitting ratios in the 3x3 fiber coupler led to an imperfect performance (Choma, M. A. et al. 2003; Mao et al. 2008). The polarization-based demodulation used a polarization beam splitter in the detection system and utilized the  $\pi/2$  phase difference between two orthogonal (i.e. horizontal and vertical) states of polarization of the light beams

detected by two independent detectors (Vakoc et al. 2006). The performance of the method, nevertheless, is sensitive to birefringence of the sample, i.e. any variation in sample birefringence will significantly affect the mirror image rejection performance. The dual-reference technique achieved a  $\pi/2$  phase relation by using two separated reference arms in a single interferometer. The optical path lengths of the two reference arms were adjusted to be different by about  $\lambda/4$ , which provided a phase difference of  $\pi/2$  between the two interferograms simultaneously detected by two detectors (Lee 2008; Lee et al. 2009). However, the random phase change in two reference arms makes it difficult to maintain the  $\pi/2$  phase difference between two detected interferograms.

A different approach of retrieving the complex interference signal is based on Hilbert-transform methods such as carrier frequency modulation (Zhang et al. 2004) and BM-scan (Yasuno et al. 2006; Wang 2007b) methods. The Hilbert-transform based methods require no extra acquisition to reconstruct each frame of the full-range image and hence maintain the full acquisition speed of the conventional FD-OCT. Zhang et al. first presented the method for construction of the complex spectral interference signal using Hilbert transformation (Zhang et al. 2004). A high speed electro-optics (EO) phase modulator was used in the reference arm to generate a stable carrier frequency of the spectral interferogram. The algorithm as shown in Figure 2.6 was used to achieve the full-range signal. The technique is, however, only valid for the SS-OCT system, in which the spectral interference is detected in a time-sequential manner.

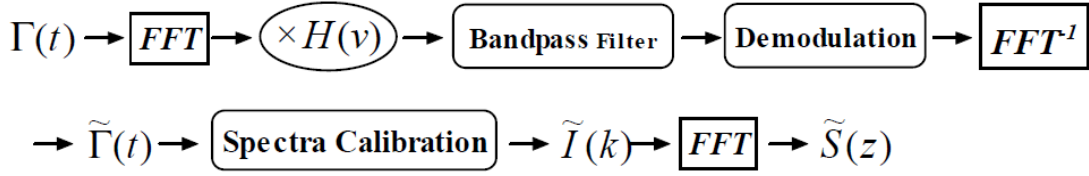


Figure 2.6: The processing algorithm to achieve the full-range depth profile in (Zhang et al. 2004)

Later, Yasuno et al. presented a new acquisition scheme that allowed for reconstruction of the complex spectral interference signal by adding phase modulation along the lateral scanning axis of the acquired spectra, the so-called BM-scan method (Yasuno et al. 2006). The processing diagram of the BM-scan method is illustrated in Figure 2.7. First, the acquired spectra (Figure 2.7a) are Fourier transformed along the time axis (i.e. lateral scanning axis). The transformed signal is subject to frequency shift as shown in Figure 2.7(b) caused by the phase modulation along the lateral scanning direction. Next, the band-pass filter is applied to filter out the negative frequency components. Then, the filtered signal is inverse Fourier transformed yielding the complex spectral interference signal as a result. Finally, the complex interference signal is Fourier transformed along the  $k$  axis yielding a full-range signal as shown in Figure 2.7(c). The main advantage of the BM-scan method is that it retrieves the full-range signal without sacrificing the acquisition speed of the system. Nevertheless, the technique requires extra processing steps such as forward and backward Fourier transformations as well as band-pass filtering to reconstruct complex spectral interference signals prior to normal Fourier transformation.

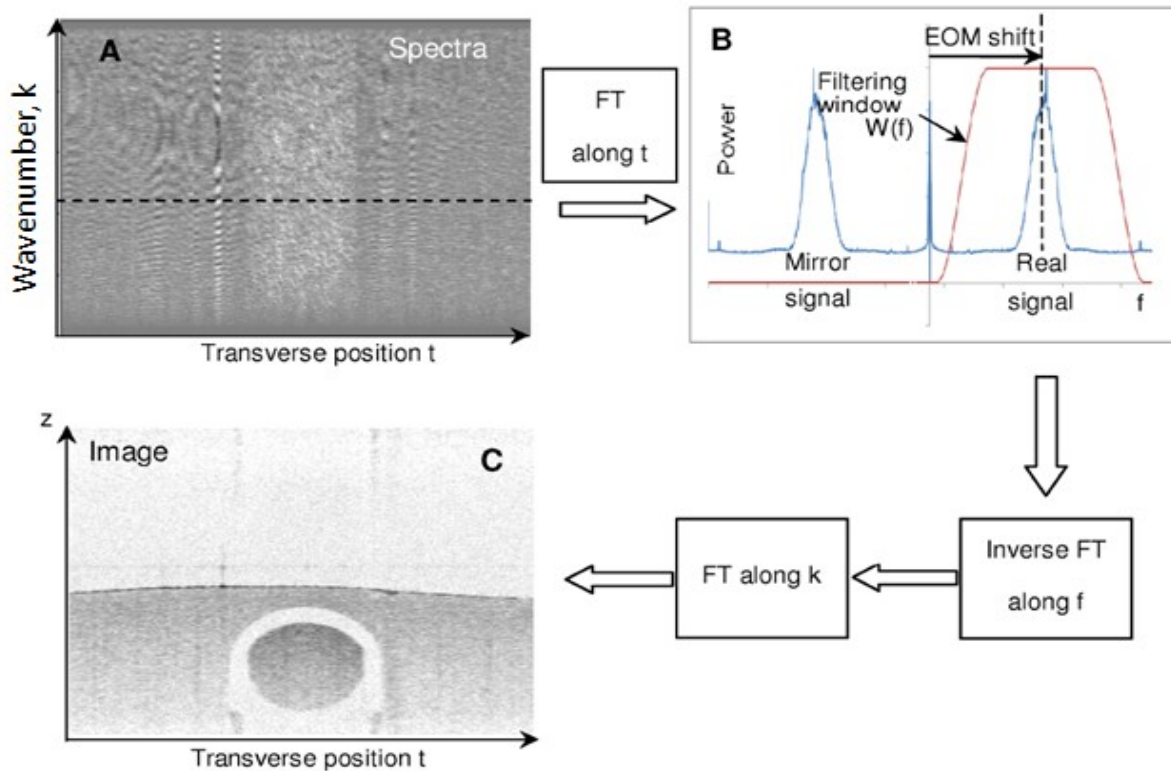


Figure 2.7: Processing diagram of the BM-scan method where (A) is a frame of acquired modulated spectra, and (B) is the 1st Fourier transform along the time axis (lateral direction), in which the band-pass filter is applied to filter out the negative frequency components. An inverse Fourier transform is then performed yielding complex spectral interference signals that give a mirror-free image in (C) after a Fourier transform in the  $k$ -domain (Jaillon et al. 2010).

The BM-scan method proposed by Yasuno et al. was based on phase stepping modulation using a EO phase modulator, which added complexity in the acquisition scheme. Later, Wang reported the technique of achieving linear modulation along the lateral scanning axis by attaching the reference mirror on a piezoelectric translation stage (Wang 2007b). The data processing was also simplified through the use of direct Hilbert transformation. Moreover, the acquisition of the BM-scan method was further improved by simply offsetting the sampling

beam spot away from the pivot point of the scanning mirror to introduce same modulation frequency without additional hardware modification (An and Wang 2007; Baumann et al. 2007; Leitgeb et al. 2007).

## 2.4 Optical Coherence Microscopy

Conventionally, OCT utilizes low NA imaging optics to achieve quasi-invariant lateral resolution over an imaging depth range of about 2 to 3 mm, corresponding with the depth penetration limit of OCT imaging, and hence provides lateral resolution in the range of 10 to 30  $\mu\text{m}$ . In order to improve lateral resolution, Optical Coherence Microscopy (OCM) was introduced by utilizing a high NA microscope objective in the sample arm (Izatt et al. 1994). Consequently, high resolution OCMs capable of lateral resolution of 2 to 3  $\mu\text{m}$  were demonstrated in a time domain OCM (TD-OCM) setup (Drexler et al. 1999; Aguirre et al. 2003). However, this improvement comes at the expense of a reduction in the imaging depth range caused by defocus or blur effect. The reported DOFs were 35  $\mu\text{m}$  in (Drexler et al. 1999) and 30  $\mu\text{m}$  in (Aguirre et al. 2003). In addition, based on full-field illumination, the technique of parallel acquisition of one dimensional time-encoded spectral interference signals without lateral scanning was demonstrated to achieve high speed and mechanical stability volumetric imaging. Nevertheless, utilizing a fixed high NA objective, the depth of imaging was limited to a couple of hundred micrometers (Povazay et al. 2006).

To achieve high lateral resolution over a large imaging depth range, Schmitt et al. introduced a dynamic focusing scheme for OCM, in which the high lateral resolution throughout

the depth of the sample was achieved by not only increasing the NA of the imaging optics but also refocusing into the sample with depth to compensate for the limited DOF (Schmitt et al. 1997). Following the concept of dynamic focusing, many solutions have been proposed, including mechanical refocusing (Lexer et al. 1999; Podoleanu et al. 2000; Cobb et al. 2005; Xie et al. 2006), and refocusing with non-moving-parts single-element optical-systems such as a MEMS mirror (Qi et al. 2004) and a liquid lens (Divetia et al. 2005). However, most of these techniques were applied to TD-OCT. Intrinsic to the principle of FD-OCT is that no refocusing may be applied given that an entire axial scan is obtained from a single measurement of spectral interference.

In FD-OCM, even though the entire reflectivity profile along the depth can be collected at once from the inverse Fourier transform of the spectral interference signal, the use of a high NA objective lens leads to clear distinctions between the in-focus and out-of-focus regions across the imaging depth. Imaging techniques similar to C-Mode scanning in ultrasound imaging have been investigated to recover an out-of-focus portion (Sherar et al. 1987; Huber et al. 2005b). The purpose of these studies was to demonstrate feasibility of high lateral resolution and as such the re-focusing was applied by manual translation of the objective lens. By adopting the methods reported in (Sherar et al. 1987), Huber et al. presented the method of volumetric merging of OCT data, in which manual segmentation of the C-Mode OCT images followed by the summation of the segmented images to form a high-resolution image were implemented (Huber et al. 2005b).

In addition, an approach consisting in using multiple beams to image in parallel at a few depth planes has also been developed, and a four-beam implementation and image fusion have been demonstrated (Holmes and Hattersley 2009). Each beam is focused at a different depth and the NA of the beam is chosen to achieve a DOF equal to one quarter of the total desired focal depth. The NA also determines the lateral resolution. The advantage of this multiple beam approach is faster speed of acquisition since four images in depth are acquired simultaneously. The fused image from the four beams, however, exhibited discontinuities between the depth regions caused by differing signal-to-noise ratios of the OCT images from neighboring beams, an inherent property of the technique. To eliminate the discontinuities, a blending approach was recently developed as reported in (Holmes and Hattersley 2009). Nevertheless, there are still some challenges associated with the technique including the requirement of sufficient source power to accommodate four beams operating at high signal to noise ratio and sensitivity. Also, the presence of crosstalk between the channels has been observed and traced back to scattered light from the reference mirror entering adjacent channels. The coupling of lateral resolution to the required number of beams was also a limitation.

A different approach to maintaining lateral resolution is to use axicon optics, which exhibits the Bessel beam characteristic that intrinsically displays invariant lateral resolution over a larger distance compared with commonly used spherical lenses (Ding et al. 2002), with the best sensitivity achieved to date of about 80 dB in a double pass setup and invariant resolution of approximately 8  $\mu\text{m}$  over 4 mm depth of imaging (Lee and Rolland 2008). This capability allows



the ease of application to FD-OCT. Nevertheless, the best lateral resolution of the axicon lens reported to date is still low compared with OCM.

## **2.5 Endoscopic OCT**

Endoscopic optical coherence tomography (EOCT) combines endoscopy with OCT to offer depth sectioning with high sensitivity as well as high spatial resolution for endoscopic imaging. EOCT is suitable for imaging within tubular organs such as the vascular system, the lung, the gastrointestinal tract, the breast duct, and the urinary tract (Yaqoob et al. 2006).

As in all technologies, the clinical applications set the critical parameters for imaging, which can significantly differ across applications. For example, State of the Art endoscopic OCT currently implemented clinically for cardiovascular imaging utilizes a 0.8 mm diameter catheter with 8 to 10  $\mu\text{m}$  axial resolution and 30  $\mu\text{m}$  at-focus lateral resolution. For cardiovascular imaging, lateral resolution is not the driving parameter, speed is the critical parameter. Furthermore, a catheter with diameter of less than 1 mm enables imaging inside arteries of 1 mm to 5 mm in diameter, a strict requirement for clinical practice. If high lateral resolution images of various artery sizes could be obtained, it would surely be desirable. For cancer screening or guided biopsy on the other end, resolution both in axial and lateral dimensions is the critical parameter and thus there is a keen interest in the development of ultra high resolution EOCT, achieving resolutions in the order of 5  $\mu\text{m}$  and in the future approaching the micron or submicron for cancer-related imaging applications. In addition, while small size catheters may be required

for imaging lungs, breast, prostate tissues to name a few, catheters with a few millimeters in diameter can also find direct application such as for the GI track.

The first side-imaging endoscopic probe for OCT was proposed by Tearney et al. (Tearney et al. 1996) with a 1.1 mm diameter catheter. A 38  $\mu\text{m}$  lateral resolution and a 20  $\mu\text{m}$  axial resolution were reported, and an OCT image of *in vitro* human saphenous vein acquired by the authors' probe was presented. The circumferential scanning was achieved by rotating the whole probe using a gear system and rotary optical coupling at the proximal end. Almost at the same time, Tran et al. (Tran et al. 2004) and Herz et al. (Herz et al. 2004) reported the use of micromotors at the distal end of the endoscopic probe to achieve circumferential scanning without rotating the whole probe. However, the overall probe size was limited by the size of the micromotor. Tran et al. reported a 2.4 mm diameter probe with resolution of approximately 9.5  $\mu\text{m}$  axially and 13  $\mu\text{m}$  laterally, while Herz et al. reported a 5 mm diameter probe with resolution of 5  $\mu\text{m}$  axially and 8  $\mu\text{m}$  laterally.

As previously discussed in section 2.4, axial resolution is quasi-invariant throughout the imaging sample as long as the imaging interferometer is balanced for equal dispersion in both arms of the interferometer. On the other hand, to achieve high lateral resolution, one needs to design imaging optics with high NA while minimizing and balancing residual aberrations. For a high resolution endoscopic probe, axial chromatic aberration can cause a decrease in the effective bandwidth of the light returning from a particular depth inside the sample. Therefore, achromatization of the probe is required not only to improve the lateral resolution but also to maintain the axial resolution. Tumlinson et al. (Tumlinson et al. 2005) reported the use of an

optical system design to achieve an achromatized endoscopic probe with a 4.4  $\mu\text{m}$  FWHM lateral spot size at the focus. The probe was designed to operate in a push-pull longitudinally scanning mode with an imaging depth of 0.5 mm.

Nevertheless, the use of high numerical aperture leads to a small depth of focus and thus a small working range of EOCT (i.e., the high lateral resolution is maintained only close to the focus position). In all these technologies, the lateral resolution reported is at the focus of the imaging probe and dramatically degrades outside the confocal parameter. To maintain a high lateral resolution throughout the depth scanning range, one needs to re-focus the imaging optics to fully benefit from the high numerical aperture across the full depth of the sample (Murali et al. 2007). Doing so with mechanically moving components prohibits high speed scanning and real time imaging (Herz et al. 2004). Xie et al. proposed the use of a GRIN lens rod to dynamically adjust the focus of the endoscopic probe. The authors investigated two different commercially available rod lengths of 127 mm and 219 mm (Xie et al. 2006), however in either case, the length and the non-flexible nature of the GRIN lens rod limited the areas of application. Recently, Lee and Rolland investigated the use of Bessel beam imaging using an axicon lens embedded in an optical system design; results show approximately 6  $\mu\text{m}$  invariant lateral resolution and invariant peak intensity throughout a 1.2 mm imaging depth (Lee and Rolland 2008). The probe can be as small as 2 mm, which is currently limited by a circumferential scanning MEMS motor at the distal end of the probe. Using external rotors, the probe can be less than 1 mm. This invariant resolution comes at the cost of lower illumination power at each focal position compared to a conventional focusing lens, yet large depth of focus was obtained.

## 2.6 Doppler OCT

The Doppler effect was discovered by the Austrian physicist Christian Johann Doppler in the mid 1800s (White 1982; Roguin 2002). For many years, various Doppler imaging techniques have been developed in the field of ultrasound imaging (Sigel 1998). Doppler OCT (DOCT) is an extension of conventional OCT that is capable of not only structural mapping but also real time monitoring of flow characteristics, such as location, direction, speed, and profile, in biological samples (Leitgeb, R. et al. 2003a; Mariampillai et al. 2007; Davis et al. 2008).

Two modes of operation of Doppler imaging are normally performed in DOCT as illustrated in Figure 2.8. One is a *brightness mode* or B-Mode Doppler, in which multiple axial scans (A-scans) are collected while performing a lateral scan (B-scan). An intensity map generated in B-mode represents the cross-sectional image of the sample structure as shown in Figure 2.8(a). Corresponding to the structural map, the magnitude of the local phase shift is represented in 2D color mapping as shown in Figure 2.8(b). Therefore, B-Mode Doppler is useful for locating the flow location inside the mainly static structure.

The other is a *motion mode* or M-Mode Doppler, in which multiple A-scans are collected at a fixed position of the sample beam. The example of an intensity map generated in M-Mode is shown in Figure 2.8(c). M-Mode Doppler generates a 2D map of Doppler signal, in which one axis is a depth profile and the other axis represents the time evolution of the flow as shown in Figure 2.8(d). M-Mode Doppler is useful when the location of the flow is known, and one wants to monitor the flow changes as a function of time.

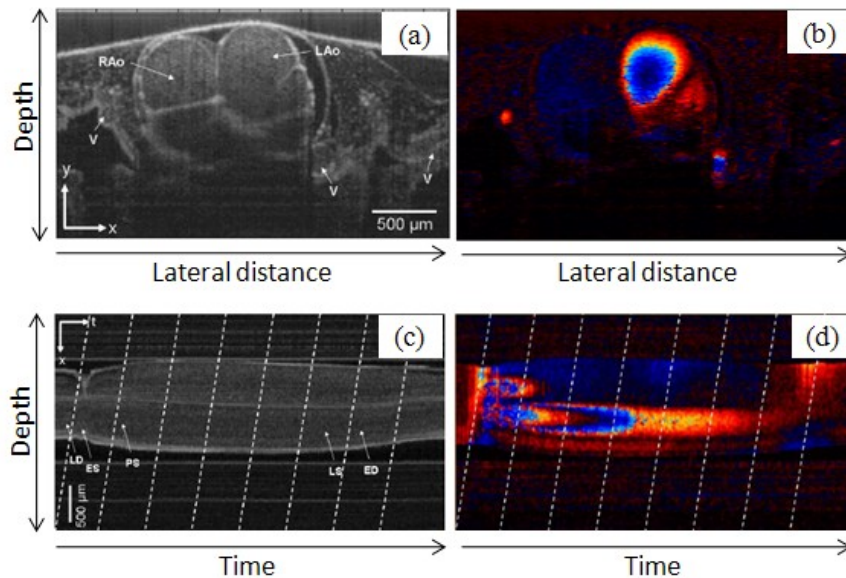


Figure 2.8: Examples of (a) B-Mode intensity map, (b) B-Mode Doppler map, (c) M-Mode intensity map, and M-Mode Doppler map (Mariampillai et al. 2007).

Over the past ten years, various OCT-based flow detection techniques have been actively developed, such as the short time Fourier transform technique (Chen et al. 1997; Izatt et al. 1997), phase-resolved Doppler imaging (Zhao et al. 2000a), resonant Doppler imaging (Bachmann et al. 2007), speckle variant detection (Mariampillai et al. 2008), optical angiography (Wang, R. K. et al. 2007), and time-frequency analysis technique (Szkulmowski et al. 2008a). The first attempt of Doppler imaging using OCT was based-on the short-time Fourier transform technique. At almost the same time, Chen et al. (Chen et al. 1997) and Izatt et al. (Izatt et al. 1997) reported 2D-velocity mapping techniques implemented in TD-OCT systems. Both studies were based on the use of the short time Fourier transform (STFT) to determine a localized Doppler frequency-shift from the TD-OCT signal and both presented the result in the form of a color Doppler map. However, the use of STFT not only required many Fourier transform

operations but also led to the trade-off between the Doppler resolution and Doppler signal quality.

Later, Zhao et al. presented a method of phase sensitive detection scheme for TD-OCT that allowed extraction of Doppler information directly from the phase difference between two axial scans, the so-called phase-resolved DOCT (PR-DOCT) (Zhao et al. 2000a). The phase information of the OCT signal was extracted through the use of Hilbert transformation and band-pass filtering. However, the phase stability of the system limited the velocity sensitivity and accuracy of the technique. In addition, it was sensitive to the random phase of the noise background. Later, the phase stability of phase-sensitive TD-OCT was improved through the use of a combination between a hardware in-phase and quadrature phase (I&Q) demodulator and a computational algorithm based-on Kasai autocorrelation as velocity estimator (Yang et al. 2002).

To avoid the strict requirement of high phase stability as in PR-DOCT, many amplitude-based flow detection techniques were proposed. Evolved from the concept of the BM-scan method for full-range FD-OCT, optical micro-angiography (OMAG) separated the back-scattering signals from the moving and static scatterers by introducing a constant frequency modulation along the lateral dimension (time axis) of each frame acquisition of the spectral interferograms (Wang, R. K. et al. 2007). The constant frequency modulation was generated by moving the reference mirror at a constant speed during each frame acquisition. The mechanism of OMAG is illustrated in Figure 2.9. The acquired 2D spectral interferogram was first Hilbert transformed along the time axis and was then Fourier transformed along the  $k$  axis. The Doppler frequency induced by moving scatterers caused the Hilbert transformations of the signals from

the moving and static scatterers to be complex conjugate of each other. As a result, the signals from moving and static scatterers were separated into positive and negative sides of zero path-delay after the Fourier transformation along  $k$  (wave number). The modulation frequency set a threshold between the moving and statics structures and hence set the velocity sensitivity of the method.

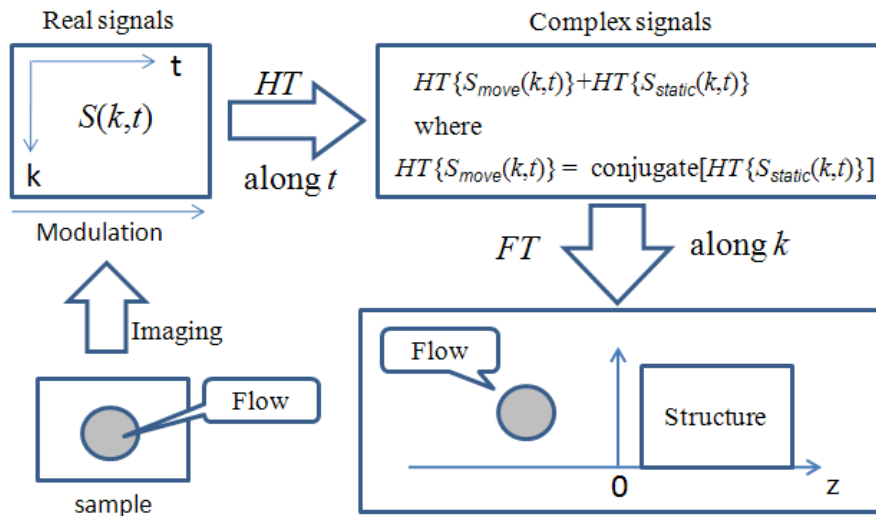


Figure 2.9: Illustration of OMAG algorithm

Furthermore, by moving the reference mirror in opposite direction, the flow in opposite direction was detected, which allowed OMAG to detect bidirectional flow (Wang 2007a). However, the technique required two set of acquired spectra (i.e. one for each direction of flow) and hence the information about the flow direction was achieved at the expense of an increase in both acquisition and processing times. Later, a technique for extracting bidirectional flow from a single set of acquired spectra using software frequency modulation in post processing was

presented (Wang 2008). The technique, however, was still subject to computational load. OMAG has been proven to be capable of *in vivo* 3D flow segmentation of capillary network in biological samples. Nevertheless, the information about flow velocity was not available.

In spectrometer-based FD-OCT, any sample movement within the integration time of a camera causes blurring of interference fringes or *fringes wash-out* that attenuates the amplitude of the OCT signal. Using this concept, resonant Doppler imaging matched the phase of the reference signal to the phase of the signal from the moving sample by moving a reference mirror during the acquisition of the spectral interference signal (Bachmann et al. 2007). This phase matching prevented the fringes wash-out of the interference signal from the moving scatterers. In contrary, the interference signal corresponding to static sample structures was subject to fringes wash-out and hence subject to signal attenuation after the Fourier transformation. The signal attenuation, therefore, provided contrast between flow and static samples. The technique is particularly useful for flow imaging using spectrometer-based FD-OCT.

Most recently, an amplitude-based flow detection technique built on the concept of time-frequency analysis so-called joint spectral and time domain OCT (STdOCT) was presented (Szkulmowski et al. 2008b). STdOCT acquired multiple spectral interference signals over time at approximately the same lateral beam position and then extracts depth-resolved flow information by analyzing the amplitude shifted after the 2D Fourier transformation of the acquired 2D spectral interference pattern. The basic principle of STdOCT is illustrated in Figure 2.10. At each lateral position of the beam, multiple spectra were acquired providing a 2D spectral interferogram. The interferogram was Fourier transformed along the  $k$  axis yielding depth profile



information and then was Fourier transformed along the  $t$  axis causing amplitude shifted along  $\omega$  in the presence of any moving scatterers as shown in Figure 2.10. It should be pointed out that the process illustrated in Figure 2.10 is only for one lateral position. Therefore, the method required large amount of acquired spectra to generate a single frame of flow image. However, STdOCT has been shown to be more robust for flow measurement at low SNR as well as at close to maximum detectable velocity limit.

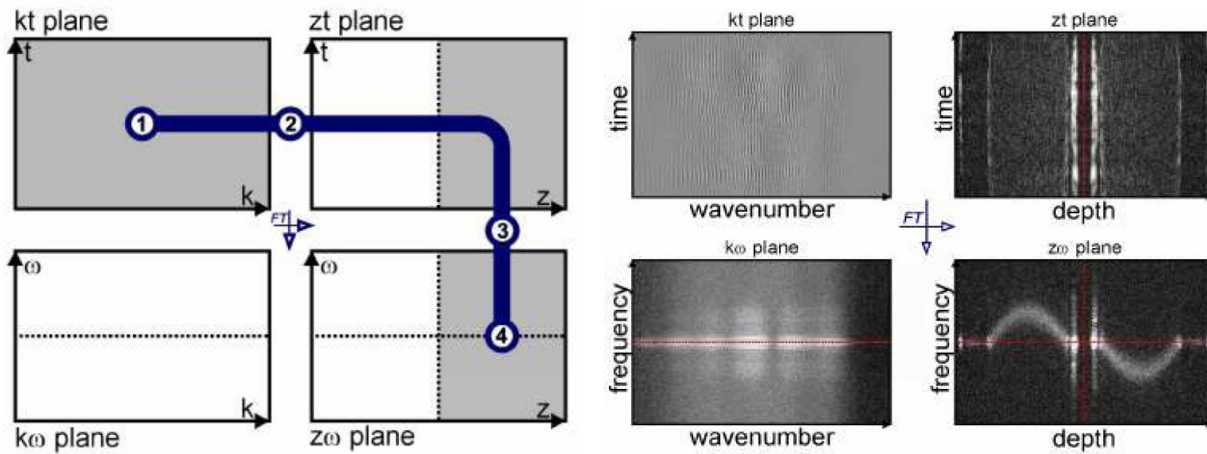


Figure 2.10: Illustration of STdOCT algorithm (Szkulmowski et al. 2009).

Nevertheless, due to its simplicity in acquisition as well as processing, PR-DOCT is the most widely used technique. PR-DOCT measures the amount of phase shift between two consecutive axial lines caused by the local axial movement and hence relies on the accuracy and stability of the detection of the phase difference between points at the same depth and same lateral position of two consecutive axial scans. The early development of phase-resolved DOCT was based on phase sensitive TD-OCT that required mechanical scanning of the reference arm

and hence limited the maximum acquisition speed to a few kHz regime. A time domain DOCT (TD-DOCT) with a speed as high as 30 frames per second for a cross-sectional image size of 250 x 512 pixels was reported (Yang et al. 2003a). The high speed scanning was achieved by using a rapid scanning optical delay-line (RSOD), and the phase sensitive detection was based on a frequency mixing technique. A minimum detectable velocity of 17  $\mu\text{m/s}$ , and a non-aliasing range of 3.9 mm/s at 8.05 kHz scanning rate were reported.

Later, the phase-resolved Doppler technique was also extended to FD-OCT, which not only has speed and sensitivity advantages over TD-OCT but also allows direct access to the phase information immediately following the Fourier transform. A spectrometer based frequency domain Doppler OCT (FD-DOCT) utilizing a continuous readout CCD camera and achieving an acquisition speed of 29.3 kHz line rate was reported (White et al. 2003). Moreover the further increase of imaging speed and the maximum detectable velocity in spectrometer based FD-DOCT, using a high-speed CMOS camera as a detector, was also investigated (Schmoll et al. 2009). However, the increase in maximum detectable velocity accommodated from high-speed acquisition comes with an increase in the minimum detectable velocity since both of them depend on the acquisition rate. With a camera line rate of 200 kHz, the minimum detectable axial velocities as measured with and without lateral scanning were 800  $\mu\text{m/s}$  and 8.2 mm/s, respectively. Nevertheless, the high speed imaging capability of FD-DOCT is attractive for real time *in vivo* monitoring of flow activity in biological samples as well as for flow segmentation in 3D that provides accurate information of flow angle (Davis et al. 2008).

In addition to the improvement in speed and velocity dynamic range, the determination of the Doppler angle measurement is also important in order to measure the absolute flow velocity. To accurately determine the absolute flow velocity, the angle between the illumination beam and the flow direction needs to be precisely determined. Many ideas of Doppler angle determination have been proposed, such as the combination of Doppler shift and Doppler bandwidth measurements (Piao and Zhu 2003), dual incident angle (Dave and Milner 2000; Pedersen et al. 2007; Iftimia et al. 2008), dual plane imaging (Wang, Y. et al. 2007), 3D flow segmentation (Davis et al. 2008), and two scanning cones (Wang et al. 2009) methods.

Pao and Zhu (2003) reported the technique of flow angle measurement by using a combination of Doppler shift and Doppler bandwidth measurements. The Doppler shift measurement yielded the flow velocity in the axial direction, while Doppler bandwidth measurement yielded the flow velocity in the lateral direction. Knowing these two quantities, the absolute flow direction and velocity were determined. The authors reported the accuracy of Doppler angle estimation of about 98% and the accuracy of flow velocity estimation of about 94% (Piao and Zhu 2003). The method, however, requires that the flow vector is in the plane of imaging, and hence is applicable for Doppler angle estimation only in two dimensions.

Dave and Milner used a dual-channel optical low-coherence reflectometry to simultaneously measure the Doppler signal at two different incident angles as shown in Figure 2.11. The separation of the beams were achieved through the use of two Wollaston prisms and polarization of the beams (Dave and Milner 2000). The flow angle was determined through the trigonometric relation of the two incident beams. An error in an estimated Doppler angle of less

than 1 degree was verified at a set flow angle of 80 degree. The two probe beams at different incident angles were simultaneously detected by two detectors. The method relies on the polarization property of the beams and hence is vulnerable to the birefringence of the sample.

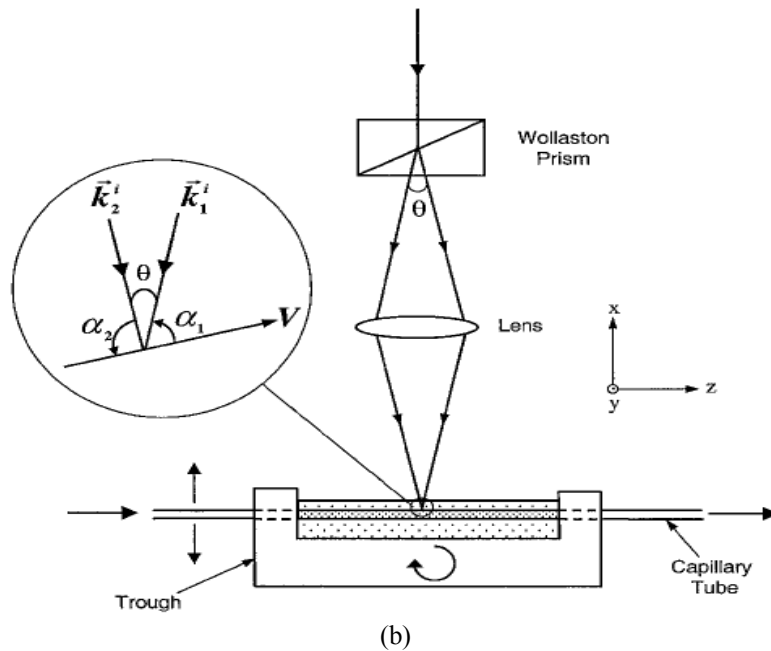
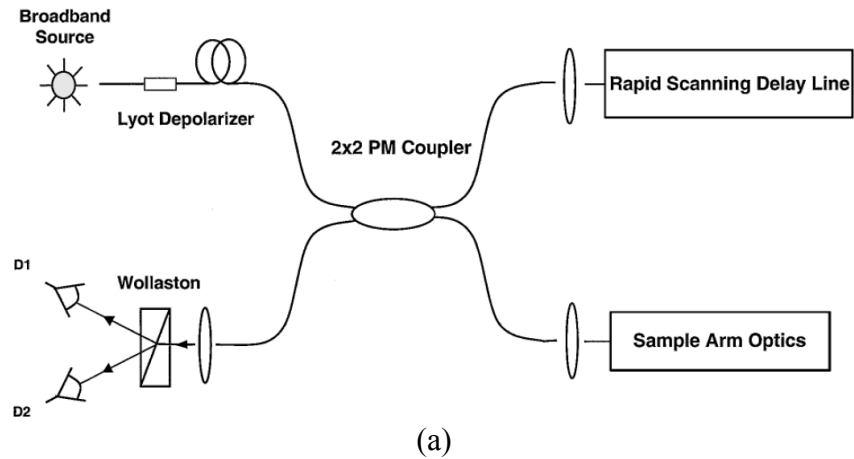


Figure 2.11: (a) The configuration of the dual-angle Doppler measurement; (b) The configuration within the sample arm optics (Dave and Milner 2000).

Moreover, Pedersen et al. used a setup as shown in Figure 2.12 to create dual incident angles encoded in the different path lengths by inserting a glass plate into a half portion of an illumination beam (Pedersen et al. 2007). The method was validated in TD-DOCT, in which three independent OCT images were detected corresponding to three different possible path lengths. In a similar manner to the method in (Dave and Milner 2000), the absolute flow velocity vector then can be fully determined through the trigonometric relation of the two incident beams (see Figure 2.12). The root-mean-square error of the Doppler angle estimation of less than 1 degree was verified over the range of set flow angle from 82 to 98 degree. However, this method was also applicable only when the flow direction is in the plane of two component beams. The angle determination in three dimensions will involve a more complicate optical delay line. Moreover, the path length encoded nature of the method leads to requirement of a longer scanning range and hence reduces the acquisition speed in TD-DOCT. The effect is expected to be more significant in FD-DOCT, in which the imaging depth range is limited.

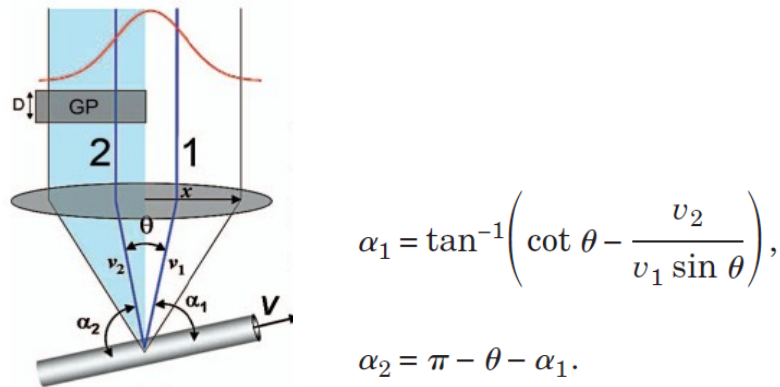


Figure 2.12: The illustration of dual incident angles encoded in the different path lengths (Pedersen et al. 2007)

Following the concept of dual-angle illumination, Iftimia et al. demonstrated the use of dual-beam, dual-angle with two independent FD-DOCT systems as shown in Figure 2.13 (Iftimia et al. 2008). The system utilized two interferometers and two spectrometers in order to simultaneously detect two Doppler signals at the same position but at different angles. A telescope lens was used in the sample arm to ensure that the DOF of two beams were approximately overlapped inside the sample. The average error of a measured absolute flow velocity of 4% was reported. However, the use of two independent FD-OCT systems added complexity and challenge in optical alignment. Moreover, like the previous dual-angle setup, the angle determination was still limited in the 2D plane.

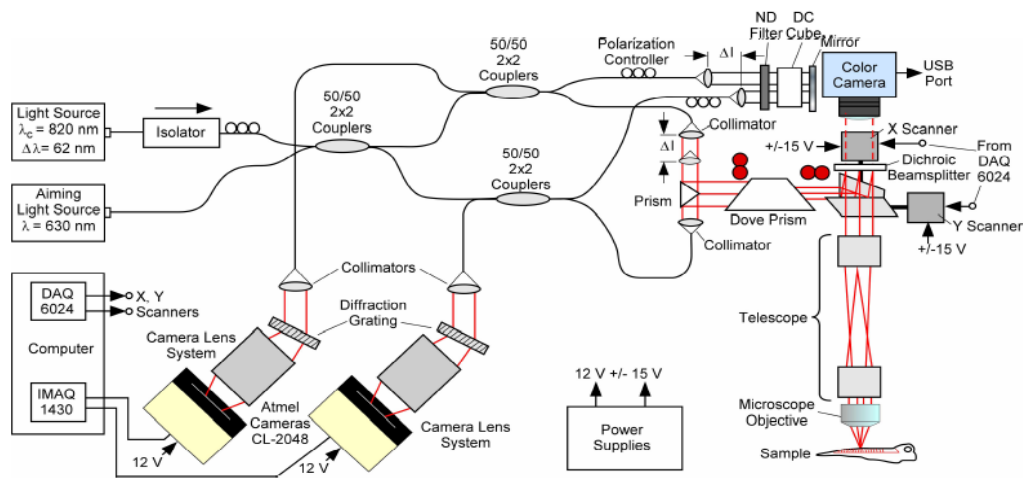


Figure 2.13: The experimental setup of dual-beam, dual-angle FD-DOCT (Iftimia et al. 2008)

In general, the determination of the Doppler angle in 3D-space is desirable and will provide more accurate absolute flow velocity. Wang et al. proposed an alternative method that was capable of measuring the Doppler angle in three dimensions (Wang, Y. et al. 2007). The

method was demonstrated using an FD-DOCT setup capable of 17 frames per second imaging speed. Two B-Mode Doppler images were measured at two different locations ( $S_1$  and  $S_2$ ) as shown in Figure 2.14. Knowing two points coordinate in 3D space, the 3D flow vector was then determined. Then, the angle between this vector and the direction of an incident beam was measured. The proposed technique was used for total retina blood flow measurement, in which the absolute flow velocity was measured and hence the flow volume was determined.

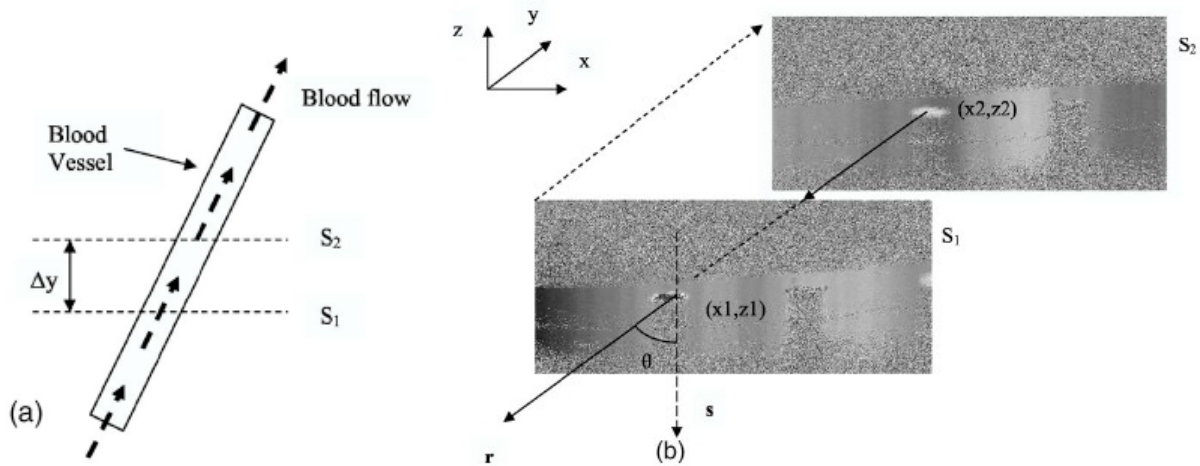


Figure 2.14: The configuration of Doppler angle determination utilizing dual-plane measurement (Wang, Y. et al. 2007)

Utilizing the high speed imaging capability of FD-DOCT, Davis et al. reported the flow angle determination using a method of 3D flow segmentation (Davis et al. 2008). The *in vivo* monitoring of the embryonic chicken heart development using DOCT was investigated. The procedure to acquire flow velocity information at each stage of development was established. First, real time B-Mode Doppler was performed at 13 frames (256x512 pixels) per second to

locate the region of interest (ROI) that is the location of the heart chamber. Then the lateral position was fixed at the center of the flow region, and the Doppler signal was recorded through time (M-Mode Doppler) for 2048 axial lines with 3800 lines per second. Finally, the volumetric dataset of 512x256x256 (lateral x depth x slices) corresponding with 5 mm x 1.8 mm x 5 mm was acquired in about 10 seconds. The volumetric data was used to determine the Doppler angle (see Figure 2.15. This method is probably the most accurate way to determine the Doppler angle. Nevertheless, it is not an efficient means of calculation, and lacks real time processing capability.

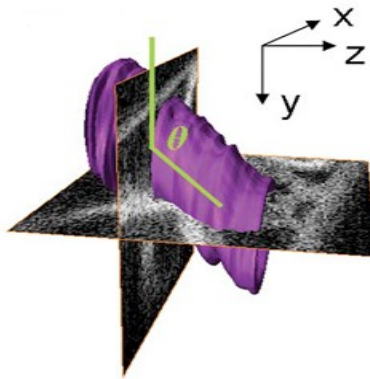


Figure 2.15: A flow angle measurement using 3D flow segmentation technique (Davis et al. 2008)

## 2.7 Summary

FD-OCT provides speed and sensitivity advantage over TD-OCT. FD-OCT systems have recently enabled imaging speeds of up to 10 to 50 times faster than standard TD-OCT. However, two main challenges in FD-OCT are the sensitivity fall-off caused by a finite spectral resolution



and the existence of the complex conjugate signal known as mirror image intrinsic to the Fourier transformation of a real signal. In addition, a further increase in the sweep rate as well as the axial resolution is demanded to enable *in vivo* high resolution 3D imaging. However, achieving high axial resolution at high acquisition speed usually requires sacrificing spectral resolution that leads to a reduction in the imaging depth range. Therefore, the removal of the mirror image in high resolution FD-OCT is desirable to double the imaging depth range.

Beside the imaging speed, another important parameter to medical diagnostics using OCT is high resolution imaging. OCM utilizes a high NA microscope objective in the sample arm to achieve both an axially and laterally high resolution image. An increase in NA, however, leads to a dramatically decreased DOF and hence shortens the imaging depth range so that high lateral resolution is maintained only within a small depth region around the focal plane. One solution to increase the depth of imaging while keeping a high lateral resolution is dynamic-focusing. Following the concept of dynamic focusing, many solutions have been proposed. The main challenge in dynamic focusing OCM is to achieve high lateral resolution over a sufficient imaging depth range at high speed to accommodate *in vivo* cellular imaging in biological sample.

EOCT combines depth sectioning capability of OCT with endoscopy to offer depth information with high sensitivity as well as high resolution for imaging within tubular organs. The lateral resolution of a typical EOCT is limited to about 20 to 30  $\mu\text{m}$ . However, for applications such as cancer screening and guided biopsy, high resolution, both axially and laterally, EOCT over large imaging depth range is in demand. Furthermore, when imaging inside tubular organs, an ability to adjust the focus position of the catheter is extremely limited.

Therefore, an endoscopic probe that is capable of either high resolution over a large imaging range or varying an imaging plane in real time would provide flexibility to locate the region of interest in EOCT.

For diagnostic purpose, conventional OCT image alone may not provide sufficient information. Therefore, an extra contrast mechanism is necessary in order to gather sufficient information for decision making especially in the field of medical diagnostics. Doppler OCT allows visualization and characterization of the location, direction, velocity, and profile of flow activity embedded in a static sample structure. High speed FD-OCT, i.e. in 100 kHz regime, allows real time flow velocity monitoring as well as 3D flow segmentation of biological samples. Nevertheless, the velocity dynamic range of DOCT has to be improved in order to be able to detect a wide range of flow velocity. Moreover, high sensitivity Doppler detection requires a high SNR OCT system.

## **CHAPTER THREE: VARIABLE VELOCITY DYNAMIC RANGE DOPPLER OCT**

This chapter presents an alternative acquisition scheme along with processing technique for a swept-source based PR-DOCT that effectively extends the Velocity Dynamic Range (VDR) of a given PR-DOCT system. The technique extends the minimum detectable velocity for a given phase stability of the system by varying the time interval between two acquired signals used to calculate the Doppler phase shift while maintaining a high phase stability between them. An example of the implementation of the technique is demonstrated in a dual VDR DOCT system, where two Doppler maps having different detectable VDRs were simultaneously detected, processed, and displayed in real time. The technique is particularly useful for high speed frequency domain OCT (FD-OCT) where the acquisition time is extremely short and hence the ability to visualize the slow axial flow is often limited.

### **3.1 Swept-Source OCT System**

#### *3.1.1 System Configuration*

This section details the experimental setup of the OCT system that was used for the Doppler imaging experiment presented in this chapter. The system was implemented with a SS-OCT built on a fiber-based Mach-Zehnder interferometer (MZI) as shown in Figure 3.1. A light source was a FDML laser (Micron Optics), having a central wavelength of 1320 nm with a tuning range of ~158 nm and an average output power of 5.6 mW (Lee 2008). The output from the light source

was coupled to the fiber and then split by an 80/20, 1x2 broadband fiber coupler. The portion of the beam with 80% power was delivered to the sample arm, out coupled by the collimator, and directed on to the mirror surface of a galvanometer beam steering (VM500, GSI Lumonics) allowing the lateral scanning of the sample beam. The sample beam was then focused into the sample through a 20 mm focal length plano-convex spherical lens. The lateral resolution was quantified through *en face* imaging of a 1951 USAF resolution target (Edmund Optics) as shown in Figure 3.2. The lateral resolution of about 10  $\mu\text{m}$  was observed. The 20% portion of the beam was delivered to the reference arm, in which the Fourier domain optical delay line was implemented in order to compensate for dispersion mismatch (Lee et al. 2005). The two beams were coupled back to the fiber passing through fiber circulators and then combined at the 50/50, 2x2 fiber coupler.

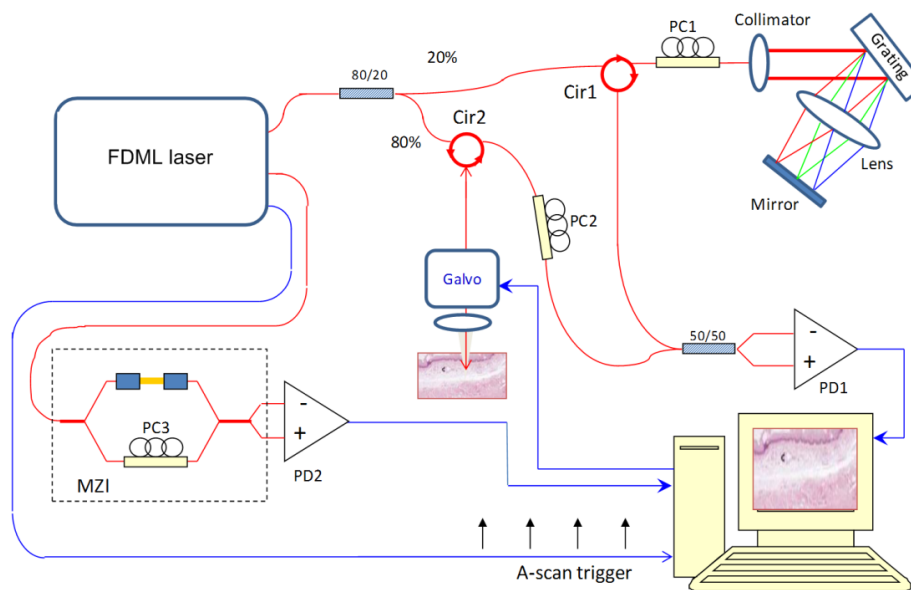


Figure 3.1: The fiber-based swept-source OCT built on Mach-Zehnder interferometer; PD = photo-detector, Cir = circulator, and PC = polarization controller

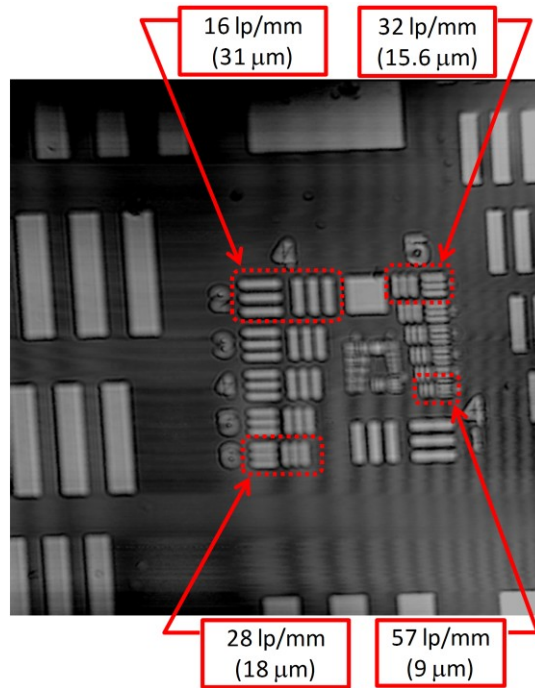


Figure 3.2: An *en face* image acquired over about 4 mm x 4 mm field of view of a calibrated resolution target, where the number of line-pairs per millimeter (lp/mm) and the corresponding lateral resolution in parenthesis of several groups of the target are provided in the red boxes.

The time-encoded spectral interference signal was detected by using a balanced photo-receiver, and then digitized on one channel of a two-channel, high-speed, 12-bit-resolution analog-to-digital converter operating at 200 Msamples/s (NI PCI 5124, National Instrument). The detected signal was recalibrated to the linear frequency-space prior to Fourier transformation to the depth profile. In this system, the recalibration process was done using a time-frequency relation measured by an additional MZI denoted by a dash box in Figure 3.1. Simultaneously with the detection of the main interference signal, the calibration signal was detected by a second photo-receiver and then digitized on another 8-bit-resolution analog-to-digital converter

operating at 250 Msamples/s (NI PCI 5114, National Instrument). The calibration curve was generated from the position of peaks, valleys, and zero-crossing of an interference signal measured by the additional MZI as will be detailed in the next section.

### 3.1.2 *MZI Calibration Curve*

A signal calibration to linear frequency domain prior to the Fourier transformation is a mandatory process in FD-OCT in order to achieve a close-to-theoretical limit axial PSF. It is even more critical in SS-OCT that utilizes a Fiber Fabry-Perot Tunable Filter (FFP-TF), such as the FDML laser used in this system, where the driven waveform is sinusoid. One technique of linear frequency calibration is by using an unbalanced MZI setup (Huber et al. 2005a). An example of the output signal of the unbalanced MZI acquired at 250 MHz sampling rate is shown in Figure 3.3(a). A sinusoidal sweep characteristic of the tunable filter caused non-uniform in the frequency of the acquired MZI signal. To avoid aliasing in the acquired signal, an optical path difference between the two arms of the MZI was set so that the highest frequency of the MZI signal was close to the Nyquist sampling limit (i.e. slightly above twice of the maximum frequency of the fringe) as shown in Figure 3.3(b). To generate a calibration curve from the acquired MZI signal, the locations of peaks and valleys were numerically detected. In addition, the locations of a zero-crossing were approximated by a half way between each consecutive peak and valley positions. The locations of peaks, valleys, and zero-crossings together were used to form a calibration curve as shown in Figure 3.3(c). The curve was then use to resample the acquired spectrum to a linear frequency spectrum as illustrated in Figure 3.4.

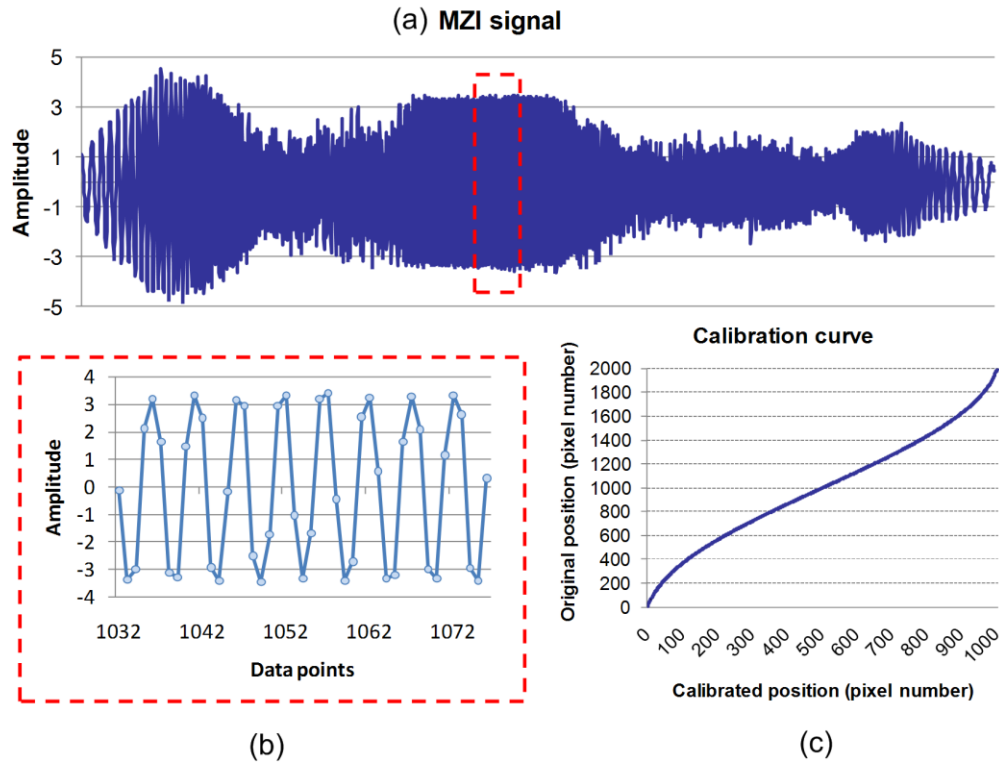


Figure 3.3: (a) The example of an interference signal acquired by an unbalanced MZI; (b) the portion of the MZI signal marked by a red dash box in (a); (c) a calibration curve extracted from peaks, valleys, and zero-crossing position of the MZI signal.

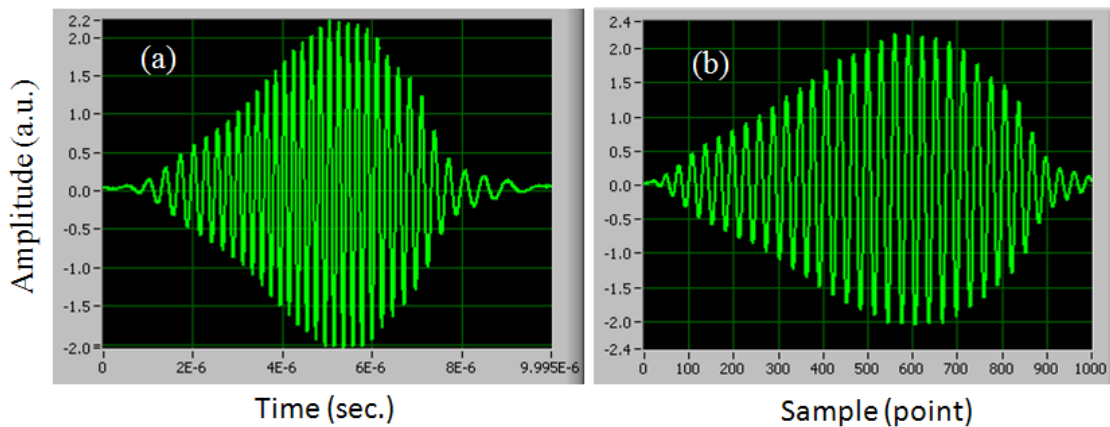


Figure 3.4: Time encoded spectral interference (a) as detected by the photo-receiver and (b) after calibration to linear frequency using the MZI curve in Figure 3.3(c).

### 3.1.3 System Sensitivity

The sensitivity of the system was quantified through the measurement of the intensity signal-to-noise ratio (SNR). A silver coated mirror was used as a sample. A neutral density filter of 30 dB double-pass power attenuation was placed in front of the sample mirror to avoid intensity saturation at the photo-detector. The intensity SNR was computed as  $SNR = (S - \mu_{noise})^2 / \sigma_{noise}^2$ , where  $S$  was a measured signal peak amplitude at the position of the reflector and  $\mu_{noise}$  and  $\sigma_{noise}$  were the mean and standard deviation of the noise floor measured within the region around the signal peak while the sample beam was blocked, respectively (Schmoll et al. 2009). The SNR in dB was defined by  $10 \log(SNR)$ .

The maximum SNR of about 98 dB was achieved as can be observed from the signal peak at the 0.2 mm axial position (red solid line) in Figure 3.5(a). Furthermore, the SNR as a function of depth, i.e. the position of the sample reflector relative to the zero path-delay, was measured to determine the imaging depth range of the system. The -10 dB sensitivity fall-off was achieved at the depth of 1.5 mm in air, corresponding to about 1 mm in biological tissue, as shown in Figure 3.5(a). Furthermore, the sensitivity of the system was improved by adding an external SOA booster amplifier at the output of the FDML laser. The averaged output power after the booster amplifier was approximately 15 mW. Nevertheless, the narrower spectral bandwidth of the booster SOA caused reduction in the frequency sweep range, i.e. from 158 nm to about 143 nm, and hence the small decrease in the axial resolution of the system. The axial resolutions in air were measured to be 12  $\mu\text{m}$  and 8  $\mu\text{m}$  with and without the booster amplifier,



respectively. The maximum SNR of 108 dB was achieved with the booster amplifier. The -10 dB sensitivity fall-off was measured to be 1.3 mm in air as shown in Figure 3.5(b).

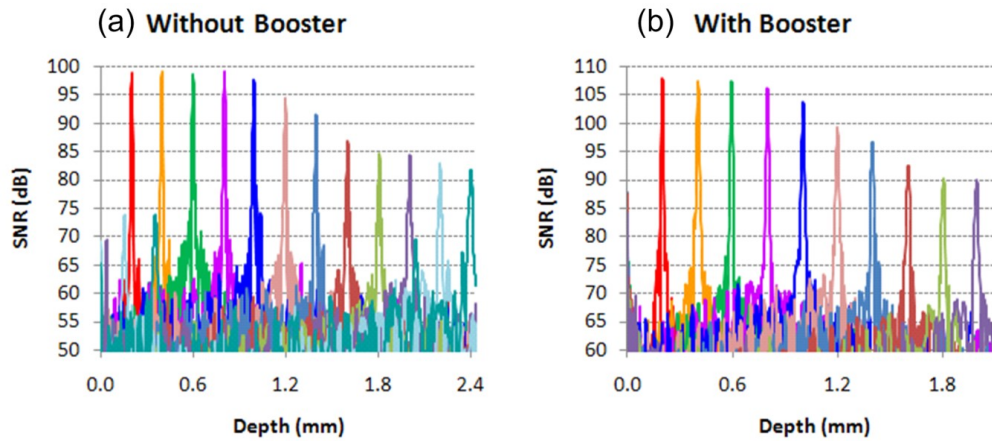


Figure 3.5: Measured SNR as a function of depth (a) without a booster and (b) with a booster amplifier

#### 3.1.4 Volumetric Imaging with SS-OCT

The volumetric imaging of an African frog tadpole (*Xenopus Laevis*) was performed using the SS-OCT system. The 3D dataset of size 400 x 400 x 400 pixels corresponding with 4 x 4 mm<sup>2</sup> lateral field of view and 1 mm along axial direction was acquired. The acquisition speed was 18,000 spectra per second (1120 samples per spectrum). Therefore, the 3D dataset was acquired in about 10 seconds. The acquired spectra were converted to depth profiles by using 2048 points fast Fourier transformed (FFT) and then cropped to 400 points to omit the mirror image part. The data was acquired and processed using Labview software (National Instrument) and then the volumetric rendering was performed using Voxx software developed by the School of Medicine

at Indiana University. A screen capture of a volumetric rendering of the dataset is shown in Figure 3.6.

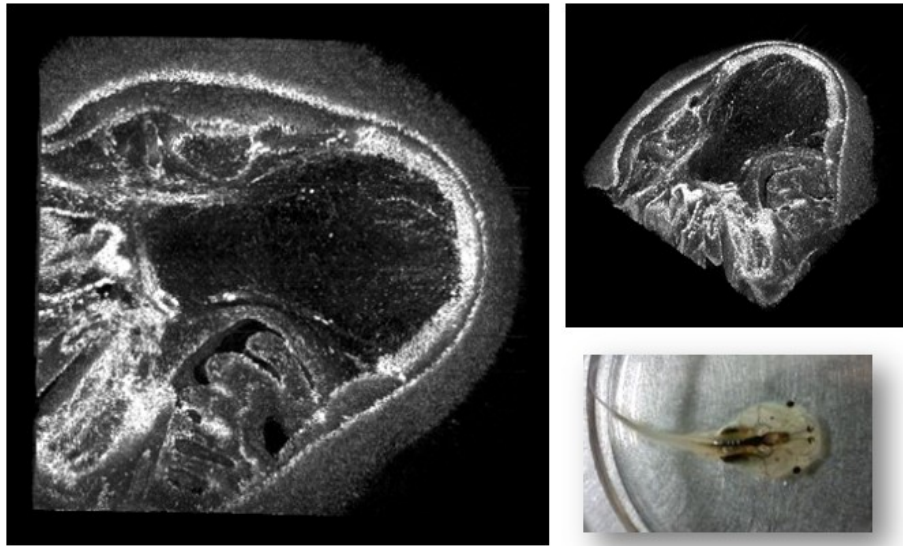


Figure 3.6: A volumetric imaging of an African frog tadpole using the developed SS-OCT system. Image was rendered with Voxx software developed by the School of Medicine at Indiana University.

### 3.2 Phase-Resolved DOCT

This section provides a mathematical description of phase-resolved DOCT (PR-DOCT). In FD-OCT, the Fourier transform of the detected spectral interference signal yields a complex function that can be expressed as

$$I(z) = A(z)\exp\{j\phi(z)\}, \quad (3.1)$$

where  $z$  denotes the axial position,  $A(z)$  and  $\phi(z)$  are the magnitude and phase components of the complex signal  $I(z)$ . The function  $A(z)$  represents the amplitude of the depth-resolved reflectivity profile that arises from the refractive index variation inside a biological sample as previously discussed in section 2.2. The phase term can be further expressed as  $\phi(z) = 2knz$ , where  $k = 2\pi/\lambda$  is the wave propagation number,  $n$  is the refractive index of the medium, and the factor of 2 arises from the round-trip propagation of the light beams in both the sample and reference arms. In the presence of a moving reflector at arbitrary depth  $z$  having axial velocity  $V_{axial}(z)$ , the complex depth profile in Eq. (3.1) can be modified as

$$I(z, t) = A(z, t) \exp\{j2kn(z + V_{axial}(z)t)\}. \quad (3.2)$$

The axial velocity  $V_{axial}(z)$  can be determined from two depth profiles measured at two different times (i.e.  $t_1$  and  $t_2$ ) that can be expressed as

$$I(z, t_1) = A(z, t_1) \exp\{j2kn(z + V_{axial}(z)t_1)\}, \quad (3.3)$$

$$I(z, t_2) = A(z, t_2) \exp\{j2kn(z + V_{axial}(z)t_2)\}. \quad (3.4)$$

By computing the phase difference  $\Delta\phi(z) = \phi_2(z) - \phi_1(z) = 2knV_{axial}(z)(t_2 - t_1)$ , where  $\phi_1(z)$  and  $\phi_2(z)$  are the phase components of the signal  $I(z, t_1)$  and  $I(z, t_2)$ , respectively, the axial velocity can be determined as

$$V_{axial}(z) = \frac{\Delta\phi(z)}{2kn(t_2 - t_1)}, \quad (3.5)$$

$$V_{axial}(z) = \frac{\lambda \Delta \phi(z)}{4\pi n T}, \quad (3.6)$$

where  $T = t_2 - t_1$  corresponds to acquisition time interval between the two signals. Because the measured phase shift only corresponds to the axial component of the flow velocity, the determination of absolute flow speed requires precise information about an angle  $\theta$  between the flow direction and the propagation direction of the illumination beam as illustrated in Figure 3.7. Consequently, the absolute flow speed can be determined from  $V(z) = V_{axial}(z)/\cos\theta$ .

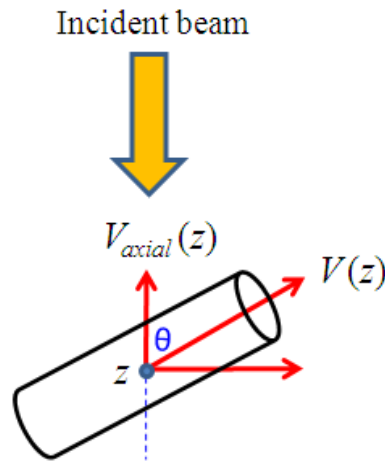


Figure 3.7: An illustration of the flow angle respective to the incident beam direction

In practice, the phase difference  $\Delta\phi$  is normally computed through the use of the inverse tangential function and hence is subject to the  $\pi$  phase ambiguity. Therefore, without phase unwrapping, the maximum detectable phase shift is  $\pi$ , and the maximum detectable axial velocity is given by

$$V_{axial,max}(z) = \frac{\lambda}{4Tn}. \quad (3.7)$$

The theoretical limit of the minimum detectable velocity, on the other hand, is determined by the phase stability of the PR-DOCT system. Different PR-DOCT systems exhibit different Doppler phase stabilities as characterized by a phase error in the absence of axial motion. This phase error determines the minimum detectable phase change and hence limits the velocity sensitivity of each particular PR-DOCT system. The phase error  $\Delta\phi_{err}$  can be statistically quantified as the deviation from the mean of the phase difference measured from a stationary sample. Consequently, the minimum detectable axial velocity is determined as

$$V_{axial,min}(z) = \frac{\lambda \Delta\phi_{err}(z)}{4\pi Tn}. \quad (3.8)$$

The range from the minimum to the maximum detectable velocities, as defined above, determines the axial Velocity Dynamic Range (VDR) of each PR-DOCT system. While in principle, the upper limit can be extended by increasing the acquisition rate (i.e.  $1/T$ ), the latter would cause the lower limit to also increase, which may be undesirable as this may lead to the invisibility of a slow flow (Schmoll et al. 2009). Similarly, the lower limit may be extended by decreasing the acquisition rate but the upper limit would be also decreased, which would limit flow velocity measurement applications (Wang, Y. et al. 2007; Davis et al. 2008; Wang et al. 2009). On the other hand, the lower limit may independently be lowered through the improvement of the stability of the system, which may be achieved in hardware but also in

software by tailoring the algorithm used to calculate the phase difference (Yang et al. 2002). Both the upper and lower limits of the VDR depend on the flow angle ( $\theta$ ) when the absolute flow is concerned. In practice, when monitoring an *in vivo* flow in a biological sample, the flow orientation may vary from zero to 90 degree relative to the incident beam, which leads to a wide dynamic range of axial flow velocity. It is to be noted that the invisibility of a slow flow will be more severe when the flow angle approaches 90 degree (i.e. flow parallels to sample surface), which produces extremely slow axial flow.

Recently, several alternative scanning protocols for different techniques of OCT-based flow detection have been developed to improve the sensitivity to slow flow of capillary blood vessels. The successful implementation of a method to increase flow sensitivity to an extremely slow flow was first demonstrated by Vakoc et al. (Vakoc et al. 2009). Designing for three-dimensional (3D) flow segmentation, multiple axial scans (z-dimension) were acquired while performing two-dimensional (2D) scanning of the sample beam, consisting of fast scanning along the x-dimension and slow scanning along the y-dimension. To achieve high sensitivity to the slow flow, the phase differences were computed along the slow scanning direction. The flow segmentation was performed by computing the amplitude-weighted circular variance of the measured phase differences. The proposed technique required high oversampling (i.e. the ratio between the sample beam width and the lateral sampling interval) along the slow axis. The capability of the technique for *in vivo* 3D imaging of capillary vessel network over a wide field of view in mouse brain was demonstrated.

About the same time, Grulkowski et al. proposed several lateral scan protocols for achieving both fast-flow and slow-flow detections in a single frame acquisition implemented in their own technology called STdOCT (Grulkowski et al. 2009). STdOCT acquires multiple spectral interference signals over time at approximately the same lateral beam position and then extracts depth-resolved flow information by analyzing the amplitude shifted after 2D Fourier transformation of the acquired 2D spectral interference pattern. As a result, the proposed scanning pattern was designed for 2D oversampling as required by the processing algorithm of STdOCT. The technique required a tremendous amount of acquired spectra for each frame acquisition, which however was compensated by an ultrahigh speed spectrometer utilizing a high speed CMOS camera (i.e. 200 kHz line-rate). The detection of both fast-flow and slow-flow information in a single frame acquisition was proven to be useful for enhancing the visualization of the retinal capillary network in a flow segmentation application.

Most recently, an idea analogous to that presented in (Vakoc et al. 2009) was implemented in OMAG, an emerging technology that is capable of *in vivo* high resolution optical angiography (An et al. 2010; Wang et al. 2010). Conventional OMAG introduces a constant frequency modulation along the fast scanning direction (i.e. x-direction) that causes the back-scattering signals from the moving and static scatterers to be separated after applying the OMAG algorithm (An and Wang 2008). The velocity sensitivity of OMAG is determined by the time interval between consecutive axial scans, and hence the high-speed imaging requirement for 3D angiograms limits the sensitivity to slow flow in conventional OMAG. To overcome this limitation, a scanning protocol was modified and the OMAG algorithm was applied along the

slow scanning axis (i.e. y-direction), which dramatically improves the slow flow detection of OMAG (An et al. 2010). The 3D flow segmentation provided by OMAG is promising for the visualization of the 3D structure of the microcirculation of a blood vessel network.

In contrary to STdOCT and OMAG, which extract flow information based-on amplitude information, PR-DOCT extracts flow information directly from the phase shift between two axial scans acquired at different times. Nevertheless, high-speed PR-DOCT is also subject to limitation in the sensitivity to slow flow. The velocity sensitivity of PR-OCT is not only governed by the time interval between the two signals but also the phase stability of the system over that time period as can be observed from Eq. (3.8). As a result, the method of measuring the speed of the flow along the slow scanning axis using PR-DOCT is challenging given the expected low phase stability between the acquisition frames. Furthermore, the method of flow analysis along the slow scanning axis requires 3D scanning together with oversampling of the acquisition frame, adding complexity in the scanning protocol and involving large amounts of data in both the acquisition and processing stages.

It is possible to apply the scanning protocol proposed in (Grulkowski et al. 2009) to PR-DOCT but the increase in phase noise in the slow scanning axis is a potential problem. Theoretically, PR-DOCT is capable of extracting flow information directly from only two axial scans, which is promising for real time flow monitoring. The raster scanning protocol (i.e. the sample beam continuously move during frame acquisition period) is known to be subject to severe degradation in Doppler phase stability unless accompanied by a high oversampling (Park et al. 2005). The degradation in phase stability may overthrow the benefit of having a longer time



interval for slow flow detection. Typically, the ratio between the sample beam width and the lateral sampling interval by a factor of ten is demanded to achieve high phase stability. The high oversampling requirement of the method involves large amount of acquired spectra and computational times that can be challenging for an application that demands real time processing and display.

### 3.3 Method for Multi-VDR DOCT

In this section, an alternative acquisition scheme along with a processing technique for a swept-source-based PR-DOCT that effectively extends the VDR of a given PR-DOCT system is presented. The technique is designed to aim for real time acquisition, processing, and simultaneous display of multiple Doppler images having different detectable VDRs so called *multi-VDR DOCT*. The technique extends the minimum detectable velocity by varying the time interval between two acquired signals used to calculate the Doppler phase shift. Therefore, the sensitivity to slow flow is extended through the use of a longer acquisition time interval for a given phase stability of a PR-OCT system. The proposed technique is particularly useful for high speed frequency domain OCT (FD-OCT) where the acquisition time is extremely short and hence the ability to visualize the slow axial flow may be limited as can be observed from Eq. (3.8).

The system was implemented with the SS-OCT as detailed in section 3.1. The FDML laser was operated at a frequency sweep rate of 44.6 kHz. To extract the Doppler phase shift with multi-VDR capability, a block acquisition technique was implemented, where the number of

sampling points was set so that multiple spectra consisting of both forward and backward sweep signals were recorded at exactly the same lateral position as shown in Figure 3.8. Furthermore, to avoid complexity in data processing and hence accommodate for real time processing and display, the backward sweep signals were omitted and only forward sweep signals as indicated by yellow dash boxes in Figure 3.8 were used in the Doppler phase shift calculation. Therefore, the time interval between two consecutive forward spectra was  $22.4 \mu\text{s}$  corresponding to a theoretical maximum detectable axial velocity of about  $11 \text{ mm/s}$ .

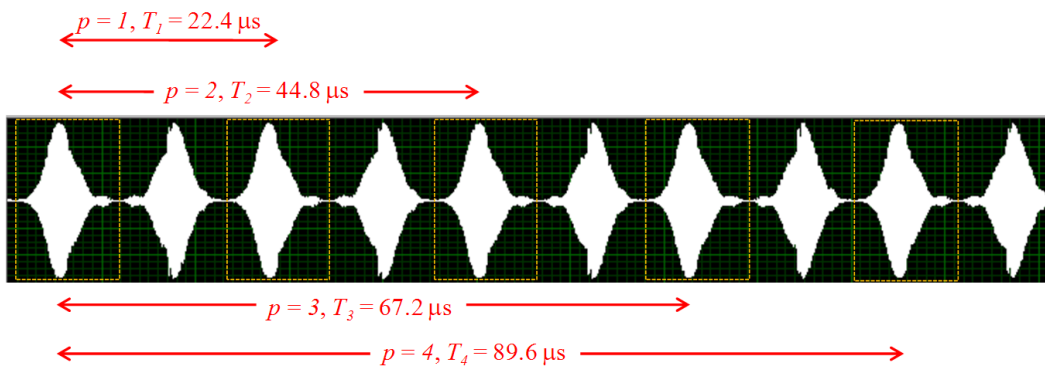


Figure 3.8: Example of acquired spectra consisting 5 sweep cycles

The block of acquired forward sweep signals was then chopped into  $N$  sub-sections containing one forward spectrum per section. Each chopped signal contained 2000 sampled points. After calibration to the linear frequency-space, the number of sampling points per spectrum was approximately 1000 points. A fast Fourier transform (FFT) was performed with zero padding to 2048 points to increase the sampling resolution in the depth profile. Based-on Kasai autocorrelation (Kasai et al. 1985), a technique that is commonly used in phase-resolved

Doppler imaging (Zhao et al. 2000b; Yang et al. 2002; Yang et al. 2003b), the phase shift was then calculated as a function of two variables using

$$\Delta\phi(z; p) = \tan^{-1} \left[ \frac{\sum_{m=1}^{M-1} \text{Im}\{I_m^*(z) \cdot I_{m+p}(z)\}}{\sum_{m=1}^{M-1} \text{Re}\{I_m^*(z) \cdot I_{m+p}(z)\}} \right], \quad (3.9)$$

where  $z$  represents an axial position,  $\Delta\phi$  denotes a Doppler phase shift,  $I_m(z)$  is a complex signal achieved from inverse Fourier transform of the  $m^{\text{th}}$  detected spectral interference,  $I_m^*(z)$  denotes the complex conjugate signal of  $I_m(z)$ , and  $p$  is a positive integer number having a value ranging from 1 to  $N-1$ . Note that  $\Delta\phi(z;p)$  is a function of two variables. For a given value of  $p$ ,  $\Delta\phi(z;p)$  is simply a Doppler phase shift profile along the axial direction. However, using this formalism, the time interval  $T$  in Eq. (3.6) is varied as a function of  $p$  as  $T_p = pT_0$  (see Figure 3.8), where  $T_0 = 22.4 \mu\text{s}$  is the time interval corresponding to the maximum acquisition rate of the system. It should be pointed out that when  $M > 2$  in Eq. (3.9), the measured phase shift is computed as an average of the phase difference between  $I_m(z)$  and  $I_{m+p}(z)$  over  $M-1$  values providing the mean phase shift as a result, which can be used to improve the phase stability (Yang et al. 2002). Nevertheless, throughout this chapter,  $M = 2$  was used to compute the Doppler phase shift, representing the least favorable case of the system phase stability. Following the calculation of the phase difference, the axial flow velocity was then determined as

$$V_{axial}(z) = \lambda_0 \Delta\phi(z; p) / 4\pi p T_0. \quad (3.10)$$

Note that because  $\Delta\phi(z;p)$  is linear with  $p$  (i.e.  $\Delta\phi(z;p)/p$  is a constant for a given flow velocity), the detected velocity  $V_{\text{axial}}$  is only a function of  $z$ . Combining this calculation with the block acquisition technique, the VDR can be varied by changing the  $p$  parameter, which is equivalent to changing the time interval between two axial lines used to calculate the Doppler phase shift as illustrated in Figure 3.8. It should be noted that, at the lower limit of the VDR as defined by Eq. (3.8), the detectable minimum phase shift is governed by the phase stability of the system that may vary as a function of  $p$  as will be shown in section 3.4. Therefore, to fully utilize the advantage of the multi-scale approach for slow flow sensitivity, the variation of the phase stability over  $p$  needs to be minimized so that the minimum detectable velocity decreases as  $p$  increases. At the upper limit of the VDR, the maximum detectable velocity is set by the  $\pi$  phase ambiguity that remains constant over the variation of  $p$ . By plugging  $T = pT_0$  in Eq. (3.7), the maximum detectable velocity therefore decreases as  $p$  increases. As a result, decreasing the time interval  $T$  alone will not extend the detectable VDR of the system. The technique presented here, which is capable of multi-scale measurement (i.e. simultaneous measurement of multiple VDRs), is required to effectively extend the overall VDR. The block acquisition technique was designed to address these two issues.

### 3.4 Phase Stability of Multi-VDR DOCT

The experimental implementation of the proposed technique was demonstrated with the swept-source based PR-DOCT system capable of varying the VDR in real time, which is useful for the detection of flow activity that exhibits a wide dynamic range of velocity. In this particular

example, the number of sampling points was set so that each single block of acquired data contained eight forward sweep spectra ( $N = 8$ ). The Doppler phase shift was then quantified by using Eq. (3.9) with  $M = 2$  and  $p$  as a free-parameter, i.e.  $p = 1, 2, 3 \dots 7$ , that could be changed in real time. The Doppler phase error corresponding to each value of  $p$  was quantified from the same set of acquired spectra by measuring the Doppler phase shift of a stationary mirror over time (White et al. 2003; Schmoll et al. 2009). Examples of computed Doppler and intensity images of the stationary mirror are shown in Figure 3.9 (a) and (b), respectively.

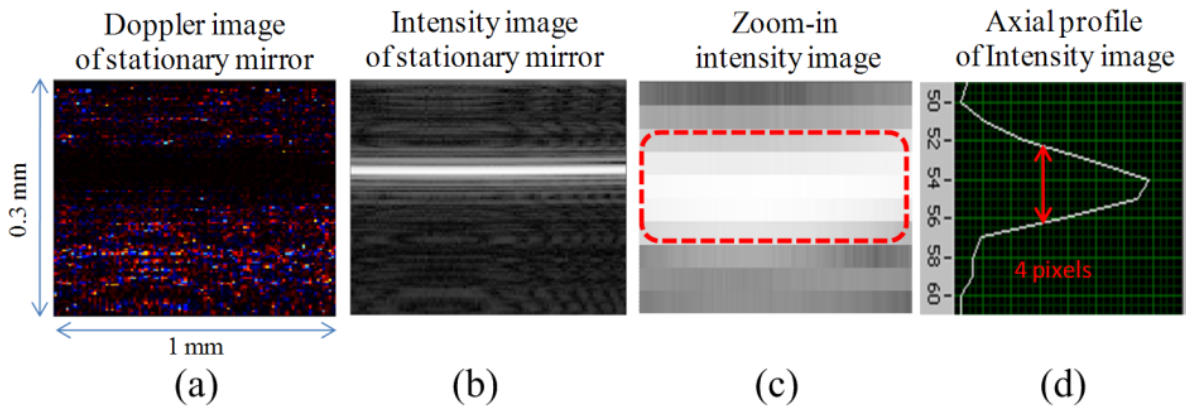


Figure 3.9: Illustration of the Doppler phase stability measurement; (a) Doppler image; (b) Intensity image; (c) zoom-in of the intensity image in (b); (d) axial profile of the intensity image in (c).

Each image consisted of 100 axial lines (A-lines) corresponding with 100 lateral positions of the sample beam with a  $10 \mu\text{m}$  sampling interval covering a lateral scanning range of 1 mm across the mirror surface. For each computed Doppler image, the measured phase shifts within the region around the mirror surface, as indicated in the red dash box in Figure 3.9 (c) (i.e.

4 pixels axially and 100 pixels laterally), were extracted and averaged. The number of pixels along depth was chosen to include only the region approximately within the Full Width at Half Maximum (FWHM) of the intensity axial profile around the signal peak as shown in Figure 3.9 (d), and the number of pixels along the lateral dimension covered the 1 mm lateral scanning range. The measurement was repeated 500 times (i.e. 500 Doppler images) and the histogram distribution was calculated as shown in Figure 3.10 for the case of  $p = 1$  and  $p = 6$  as examples.

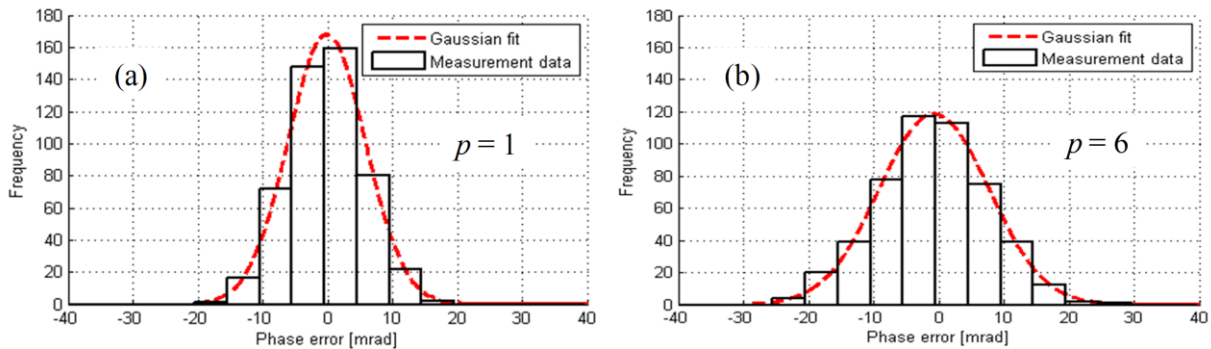


Figure 3.10: An example of histogram distribution of the measured phase shift along with the corresponding Gaussian fitted curve (red dash line) for the case of (a)  $p = 1$  and (b)  $p = 6$ ; The horizontal axis is the phase shift error in mrad.

It should be noted that, in this measurement, an intensity signal-to-noise ratio (SNR) was sufficiently high so that the effect of the background phase noise was negligible and hence the measured phase error represented the phase stability of the system as governed by, for example, the swept source, the interferometer, the scanning mechanics, and the signal processing. The SNR was computed as  $SNR = (S - \mu_{noise})^2 / \sigma_{noise}^2$ , where  $S$  was the measured signal peak amplitude at the position of the mirror surface averaged across the full lateral dimension of the acquired

Doppler image, and  $\mu_{noise}$  and  $\sigma_{noise}$  were the mean and standard deviation of the noise floor measured within the region around the signal peak while the sample beam was blocked, respectively (Schmoll et al. 2009). The SNR in dB was defined by  $SNR_{dB} = 10\log(SNR)$ . Following the analysis in (Park et al. 2005), the theoretical minimum detectable phase difference between two signals was determined as  $\sigma_{\Delta\phi}(\text{rad}) = 1/(SNR)^{-1/2}$ . An average  $SNR_{dB}$  at the signal peak was measured to be about 70 dB in this experiment, yielding a theoretical minimum detectable phase shift of about 0.3 mrad. Given that we will show thereafter that the measured phase error  $\Delta\phi_{err}$  is in the order of 10 to 20 mrad, the  $SNR_{dB}$  of 70 dB, which yields a theoretical phase error of 0.3 mrad, does not limit the phase stability measurement.

The FWHM of the histogram distribution was calculated representing the Doppler phase stability at each  $p$  value, as summarized in Table 3-1. It should be pointed out that the phase error was computed from only two axial lines without averaging ( $M = 2$ ) at each  $p$  value, and therefore represented extreme limit of the system phase stability within the time duration  $pT_\theta$ . Increasing the number of axial lines for each Doppler phase shift calculation, i.e.  $M > 2$ , will further improve the phase stability at the cost of reduction in imaging speed (Yang et al. 2002; Mariampillai et al. 2007). The phase stability tended to decrease as  $p$  was increased as shown in Table 3-1. However, since the time duration between the two axial lines used to determine the phase shift also increased, the minimum detectable velocity decreased as a function of  $p$ , and hence the method extended the total detectable velocity range of the system. From Table 3-1, the case of  $p = 1$  represents the conventional PR-DOCT method, in which the detectable axial velocity is ranging from 46.5  $\mu\text{m/s}$  to 10.9 mm/s, yielding a ratio between the maximum and

minimum detectable velocity of about 230. Using the multi-VDR technique with  $N = 8$ , the detectable axial velocity is ranging from 11.3  $\mu\text{m/s}$  to 10.9 mm/s that yields a ratio between the maximum and minimum detectable velocity of about 970, which is about four times of that achieved by the conventional method.

Table 3-1 Quantification of detectable velocity range corresponds to each value of  $p$

$p$	1	2	3	4	5	6	7
$T_p$ ( $\mu\text{s}$ )	22.4	44.8	67.2	89.6	112.0	134.4	156.8
$V_{axial,max}$ (mm/s)	10.9	5.5	3.6	2.7	2.2	1.8	1.6
FWHM $\Delta\phi_{err}$ (mrad)	13.4	13.8	15.9	18.2	20.6	22.1	22.7
$V_{axial,min}$ ( $\mu\text{m/s}$ )	46.5	23.9	18.5	15.8	14.3	12.8	11.3

### 3.5 *In vivo* Imaging with Multi-VDR DOCT

The application of the multi-VDR algorithm for real time *in vivo* imaging of biological sample is now detailed. The imaging scheme was designed in the way that two Doppler images were simultaneously acquired, processed, and displayed. One was determined at the shortest time interval between two spectra corresponding with the highest sweep rate of the light source that was capable of monitoring an axial flow speed of up to 11 mm/s in the sample. The other was determined at a longer time interval between two spectra ( $p > 2$ ) that improved the sensitivity to the slow flow activity. The time duration  $T$  used to compute the second Doppler map was designed to be adjustable in real time by varying the value of  $p$ . All spectra needed to determine both Doppler images were acquired in a single shot at the same lateral position of the incident



beam. We have shown in section 3.4 that the phase stability of the system was sufficiently high over different values of the  $p$  parameter. Therefore, in this experiment, the Doppler phase shift was extracted from only two spectra for each depth profile of the Doppler phase shift. For two Doppler maps (fast-flow and slow-flow) of size  $N_z \times N_x$  pixels (depth x lateral), the number of processed spectra was  $3N_x$  spectra. With such small amount of processed spectra, the system was capable of real time simultaneous display of the two Doppler maps along with the intensity map at a frame rate of about 3 to 4 frames per second. Each imaging frame consisted of  $500 \times 200$  pixels (axial x lateral). The acquisition of the two Doppler images was considered as simultaneous because the acquisition time interval between them was less than  $200 \mu\text{s}$ . The technique provides Doppler detection with extended velocity dynamic range as compared with a conventional PR-DOCT.

The blood flow activity within the heart of an African frog tadpole was chosen for demonstration of the multi-VDR DOCT technique. Structural images along with Doppler maps computed with  $p = 1$  (VDR1) and  $p = 4$  (VDR2) are shown in Figure 3.11 (a-l). The images were taken at a certain cut plane around the location of the tadpole's heart. The VDR1 alone is equivalent to the Doppler image that can be detected by the conventional PR-DOCT. It can be observed that certain speed of slow flow fell below the minimum detectable threshold of the VDR1 as demonstrated in Figure 3.11 (b). This slow flow however was picked up by the VDR2 as clearly observed in Figure 3.11 (c). Nevertheless, at maximum flow speed, the VDR1 provided un-ambiguity detection of the flow speed while the VDR2 was subject to the  $\pi$  phase ambiguity as shown in Figure 3.11 (k) and (l), respectively. Having both VDRs simultaneously

therefore provides an extended range of detectable flow speed for Doppler imaging in a biological sample.

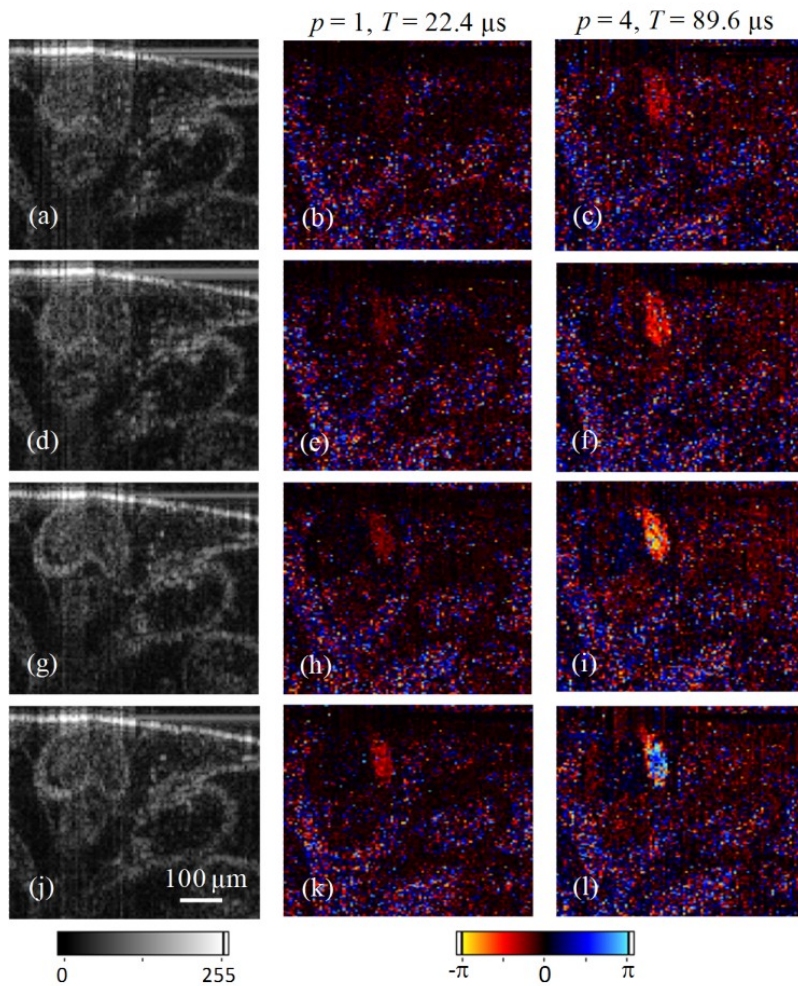


Figure 3.11: Doppler images of an African frog tadpole that were simultaneously acquired at the same location at different times where (a, d, g, and j) are intensity images, (b, e, h, and k) and (c, f, i, and l) are Doppler images corresponding to  $p=1$  and  $p=4$ , respectively.

In practice, even in the same sample, the flow in different regions can exhibit significantly different values in velocity dynamic range caused by, for example, flow orientation, vessel size, and functionality. By increasing the  $p$  value in multi-VDR DOCT, even though the

maximum detectable velocity is limited by the phase wrapping, it is capable of revealing more flow details because of the high sensitivity to slow flow as illustrated in Figure 3.12. The intensity map provides depth cross-sectional of the area of interest around the heart chamber of the tadpole as shown in Figure 3.12 (a). The Doppler image in Figure 3.12 (b) maps an axial flow velocity within a non-ambiguity velocity range from -10.9 mm/s to +10.9 mm/s with the velocity sensitivity of about 47  $\mu\text{m/s}$ . The positive and negative flow velocities represent flow in opposite directions (i.e. positive velocity corresponds to flow moving toward the observer). An axial flow speed of about -6 mm/s is observed at the location pointed by the white arrow in Figure 3.12 (b).

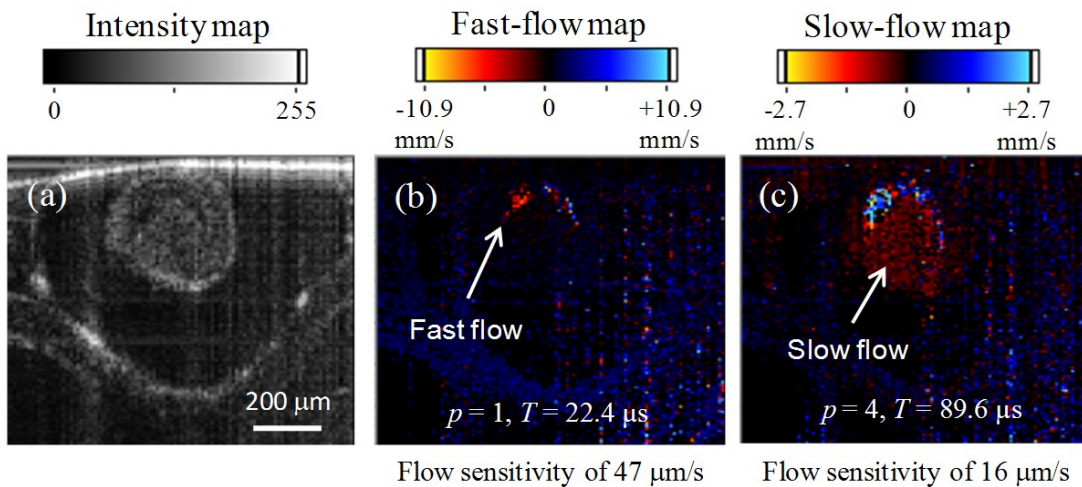


Figure 3.12: (a) Conventional intensity image, (b) fast-flow Doppler image, and (c) slow-flow Doppler image acquired at the same location of the tadpole heart region.

Simultaneously, the Doppler image in Figure 3.12 (c) provides flow information within an axial flow velocity range from -2.7 mm/s to +2.7 mm/s with the velocity sensitivity of about 16  $\mu\text{m/s}$ . Additional flow information is clearly visible in this Doppler map as indicated by the

white arrow in Figure 3.12 (c). The axial velocity within this slow flow region is estimated to be less than -1 mm/s and hence cannot be observed in Figure 3.12 (b). Nevertheless, the fast flow region (i.e. ~6 mm/s axial flow speed) as indicated in Figure 3.12 (b) is subject to phase-wrapping in Figure 3.12 (c) and hence in the slow-flow map, the fast flow velocity cannot be determined without phase unwrapping. Therefore, the technique of multi-scale VDR is useful for real time monitoring of the flow activity in a biological sample.

### 3.6 Summary

In summary, while the maximum detectable flow speed of PR-DOCT can be extended through the shortening of the acquisition time interval, the minimum detectable velocity will also be increased; this approach leads to the invisibility of the slow flow activity whose axial speed is below the minimum detectable threshold of the system. We presented a technique of multi-scale flow velocity measurement that simultaneously acquires, processes, and display multiple Doppler images having different ranges of detectable flow velocity. The technique effectively extends the overall detectable velocity dynamic range of PR-DOCT. The Doppler phase stability and the corresponding minimum detectable velocity at different time intervals ( $T_p$ ) were quantified. A detectable axial velocity ranging from 11.3  $\mu\text{m/s}$  to 10.9 mm/s was achieved. Finally, we demonstrated the implementation of the proposed technique for *in vivo* Doppler imaging of an African frog tadpole. The results demonstrated the extended sensitivity to the slow flow activity that could not be detected by the conventional method.

## CHAPTER FOUR: DUAL DETECTION FULL RANGE FD-OCT

This chapter details the development of a simultaneous detection phase-shifting-based full-range FD-OCT system referred to as the Dual Detection FD-OCT (DD-FD-OCT). The proposed technique constructs a complex spectral interference from two signals having  $\pi/2$  phase relation that is simultaneously obtained by two independent detectors, and therefore removes the complex conjugate ambiguity after the Fourier transformation. The simultaneous acquisition capability of the technique enables full range imaging without any loss of speed and is intrinsically insensitive to the movement of the sample. The full-range DD-FD-OCT provides a simple yet robust solution for real time full range imaging with FD-OCT.

### 4.1 Two Steps Phase Shifting Method

The basic principle of the full-range DD-FD-OCT method is now detailed. In a similar manner to the derivation in section 2.2, considering a typical FD-OCT configuration, a spectral intensity as detected by the detector can be expressed as

$$\hat{I}_D(k) = \hat{S}(k) \cdot \left( \begin{array}{l} |K_R r_R|^2 + 2r_R K_R K_S \int_{-\infty}^{\infty} r_S(z_S) \cos(k(z_S - z_R)) dz_S \\ + \left| K_S \int_{-\infty}^{\infty} r_S(z_S) \exp(ikz_S) dz_S \right|^2 \end{array} \right). \quad (4.1)$$

The 1<sup>st</sup> and 3<sup>rd</sup> terms (the DC and autocorrelation), can be measured by acquiring the signal while blocking the sample and reference arms, respectively, and hence can be removed through

the subtraction process. In practice, the light intensity in the reference arm is adjusted to be much stronger than that backscattered from the biological sample (i.e.  $r_R \gg r_S$ ). As a result, the cross-correlation term (2<sup>nd</sup> term) is much stronger than the autocorrelation term (3<sup>rd</sup> term) and dominates the detected spectral interference signal. The cross-correlation term carries information about the sample reflectivity as a function of optical path delay ( $z_D = z_S - z_R$ ) and hence it carries information about the sample structure through depth. The cross-correlation term alone can be rewritten as

$$\hat{I}_{\text{int}}(k) = 2r_R K_R K_S \hat{S}(k) \cdot \int_{-\infty}^{\infty} r_S(z_D) \cos(kz_D) dz_D, \quad (4.2)$$

$$\hat{I}_{\text{int}}(k) = r_R K_R K_S \hat{S}(k) \cdot \left[ \int_{-\infty}^{\infty} r_S(z_D) \exp(ikz_D) dz_D + \int_{-\infty}^{\infty} r_S(z_D) \exp(-ikz_D) dz_D \right]. \quad (4.3)$$

Following the same derivation as in section 2.1, an inverse Fourier transform of Eq. (4.3) is given by

$$I_{\text{OCT}}(z_D) = \mathfrak{F}^{-1} \{ \hat{I}_{\text{int}}(k) \} = r_R K_R K_S \Gamma(z_D) * [r_S(z_D) + r_S(-z_D)], \quad (4.4)$$

where  $\Gamma(z_D) = \mathfrak{F}^{-1} \{ \hat{S}(k) \}$  represents the complex coherence function of the source (Born and Wolf 1999; Meemon et al. 2008b). It should be pointed out that  $r_S(z_D)$  and  $r_S(-z_D)$  together construct an even symmetric function around a zero path delay set by the distance  $z_R$  (see Figure 2.4). One of them is regarded as a mirror image as previously discussed in section 2.1.

Based on a two-step phase shifting approach, two signals with  $\pi/2$  phase difference are required to construct a complex interference signal. In practice, the second signal with  $\pi/2$  phase shift relative to the first signal can be generated by introducing an optical path length difference between the two signals (Leitgeb, R. A. et al. 2003). The second signal then can be modeled as

$$\hat{I}_{\text{int},\pi/2}(k) = 2r_R K_R K_S \hat{S}(k) \cdot \int_{-\infty}^{\infty} r_S(z_D) \cos(kz_D + k\Delta z_D) dz_D, \quad (4.5)$$

where  $\Delta z_D$  is an induced optical path length difference. For example,  $\Delta z_D$  can be chosen so that  $k_0 \Delta z_D = \pi/2$ , where  $k_0 = 2\pi/\lambda_0$  and  $\lambda_0$  is the central wavelength of the light source. Since the  $\pi/2$  phase shift is chosen based on a specific wavelength, there is a deviation from  $\pi/2$  at other wavelengths over the spectral range of the light source. This error was simulated across the spectral range of a broadband frequency-swept laser as shown in Figure 4.1.

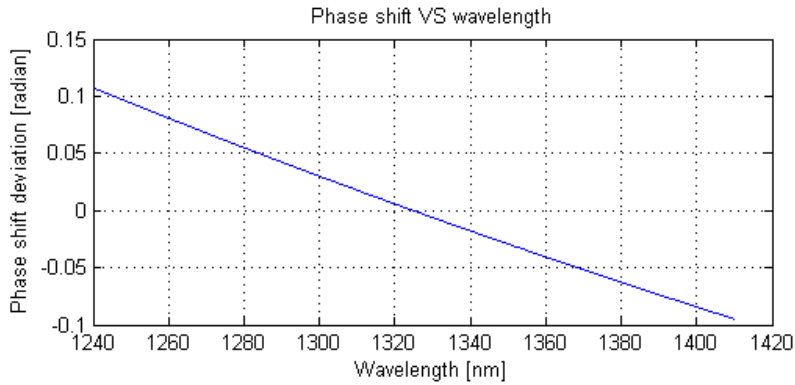


Figure 4.1: A  $\pi/2$  phase shift deviation across the spectral range

Because the deviation from  $\pi/2$  is as small as  $\pm 6\%$ , one may assume a uniform  $\pi/2$  phase shift across the spectral range. Therefore, one can rewrite Eq. (4.5) as

$$\hat{I}_{\text{int},\pi/2}(k) \cong 2r_R K_R K_S \hat{S}(k) \cdot \int_{-\infty}^{\infty} r_S(z_D) \sin(kz_D) dz_D . \quad (4.6)$$

Furthermore, if one multiplies Eq. (4.6) with  $j$ , where  $j = \exp\{j\pi/2\}$ , and then takes a Fourier transformation, one will get

$$I_{OCT,\pi/2}(z_D) = \mathfrak{F}^{-1}\{j \cdot \hat{I}_{\text{int},\pi/2}(k)\} = r_R K_R K_S \Gamma(z_D) * [r_S(z_D) - r_S(-z_D)]. \quad (4.7)$$

Finally, the summation of Eq. (4.4) and (4.7) yields ambiguity free intensity mapping.

## 4.2 The Implementation of DD-FD-OCT

### 4.2.1 *Free-Space DD-FD-OCT*

In principle, the dual detection technique is applicable to both spectrometer-based FD-OCT and swept-source-based FD-OCT. However, considering cost effectiveness, the swept-source system yields an attractive path since the cost of two photo-receivers is much lower than that of two spectrometers. The early development of the DD-FD-OCT was implemented in a free-space Michelson interferometer setup as illustrated in Figure 4.2(a) (Lee et al. 2010a). The light source was a Fourier domain mode locking (FDML) frequency swept laser (Microns Optics) operating at 1320 nm center wavelength with a sweeping range of ~158 nm as determined from -10 dB bandwidth measured by using a calibrated optical spectrum analyzer (HP 86140A, Hewlett Packard). The source sweep rate was 44.6 kHz with 5.6 mW average output power.



The output from the light source was coupled into a fiber system and then out coupled to a free-space system through a 2 mm beam diameter collimator. First, the input beam was split into the reference and sample arms by the first non-polarizing beam splitter (i.e. NPBS1) with a 50/50 split ratio. The reference beam was guided by two mirrors before it was split again by NPBS2 into two identical photo-receivers. An additional beam splitter cube in the reference arm served as dispersion matching as well as attenuator to achieve shot noise limit at both detectors. The sample beam was guided by a galvanometer beam steering (VM500, GSI Lumonics), passing through a 20 mm effective focal length spherical lens, and incident on the sample. Backscattering light from the sample was collected and guided back through the same incident path, passing again through the NPBS1, and then split by the NPBS2 into the two identical photo-detectors. Each reference beam interfered with its associated sample beam.

The two interference signals as detected by the photo-detectors were quantized on each channel of a two-channel, high-speed, 12-bit-resolution analog-to-digital converter (A/D) operating at 200 Msamples/s (National Instrument, Inc., model NI PCI 5124). The MZI signal used for the calibration in the system was recorded on another 8-bit-resolution analog-to-digital converter (A/D) operating at 250 Msamples/s (National Instrument, Inc., model NI PCI 5114). The three channels were synchronized with the external periodic triggering signal generated by the FDML light source. The  $\pi/2$  phase shifted interference signal (compared to another interference signal) was obtained by precisely rotating and shifting the NPBS2, as shown in Figure 4.2(b).

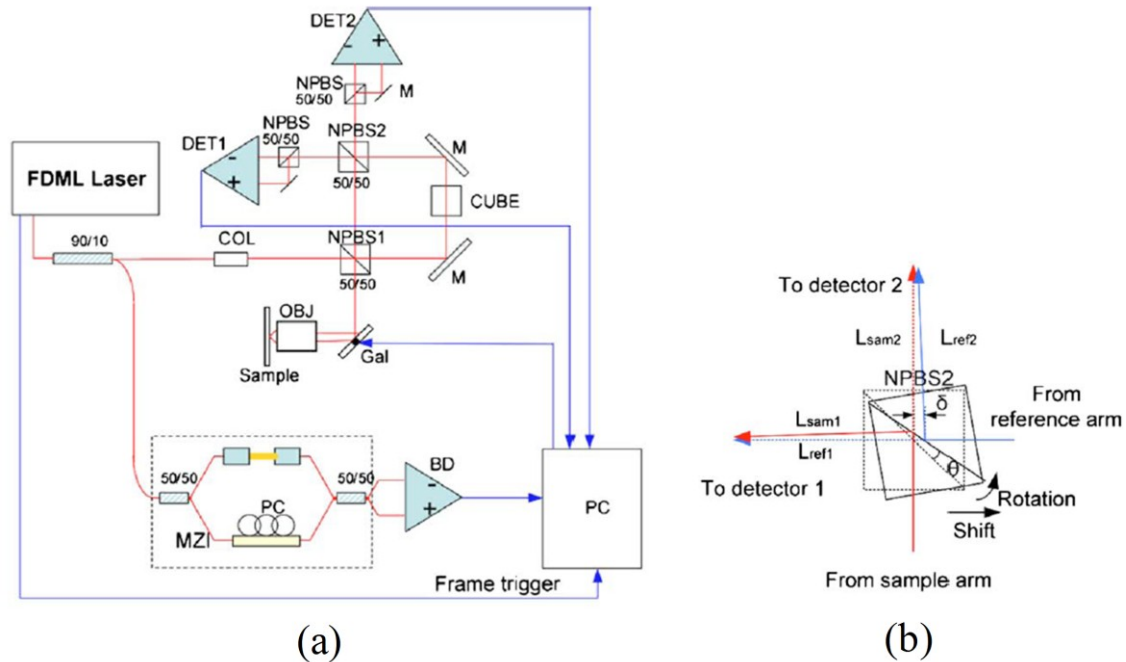


Figure 4.2: (a) A free-space DD-FD-OCT setup and (b) Adjustment of NPBS2 to obtain  $\pi/2$  phase shift between the two interference signals (Lee et al. 2010a)

When the beam splitter NPBS2 is perfectly aligned, the path length differences as seen by the 1<sup>st</sup> detector ( $L_{sam1}-L_{ref1}$ ) and the 2<sup>nd</sup> detector ( $L_{sam2}-L_{ref2}$ ) are perfectly the same. Therefore, there is no phase difference between the two spectral interference signals as detected by the two detectors. However, if the NPBS2 is shifted and/or rotated as shown in Figure 4.2(b), the path length differences are mismatched and therefore, a phase difference between the two detected interference signals is induced. The rotation angle  $\theta$  and shift  $\delta$  were adjusted to make the difference between the two interference signals equal to amount of  $\lambda/4$  at around the center wavelength, which yielded a  $\pi/2$  phase shift at that particular wavelength with slight deviation across the spectral range as previously discussed in section 4.1, in which the maximum phase

shift deviation across the spectral range was calculated to be 0.1 radian corresponding to  $\pm 6\%$  deviation from  $\pi/2$ . By using a mirror (single reflector) as a sample, a suppression of the complex conjugate peak of 35 dB was obtained in the free-space DD-FD-OCT as shown in Figure 4.3.

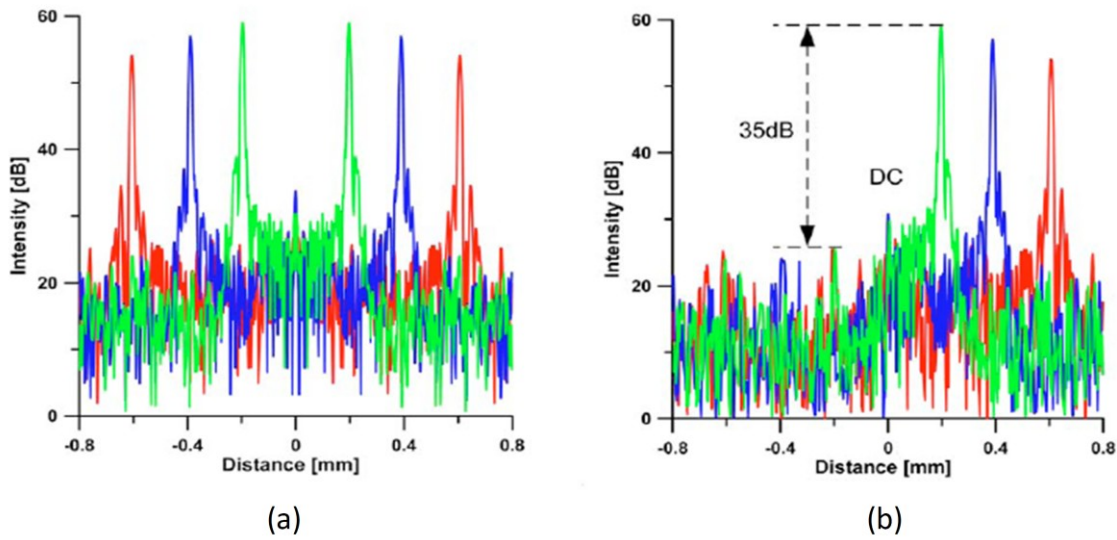


Figure 4.3: A-scan depth profiles of a single reflector in the sample arm (a) with single detection and (b) with suppression of the complex conjugate peak of 35 dB in the DD-FDOCT (Lee et al. 2010a).

#### 4.2.2 Hybrid DD-FD-OCT

Even though the free-space DD-FD-OCT provides a high stability of  $\pi/2$  phase shift between the two detected interference signals, it is subject to limitations that the signal power is not efficiently used since half of the signal power from the sample arm is rejected by the NPBS1. Furthermore, the free-space setup lacks flexibility and portability and is highly sensitive to

alignment. To overcome these limitations, an alternative scheme built on a hybrid of fiber and free-space setup in a Mach-Zehnder interferometer configuration was developed. The fiber part adds flexibility to the system enabling integration with handheld (Murali et al. 2009; Rolland et al. 2010b) or endoscopic devices (Lee and Rolland 2008; Meemon et al. 2008a) while the free-space part provides a stable  $\pi/2$  phase relation between the two detected spectral interference signals.

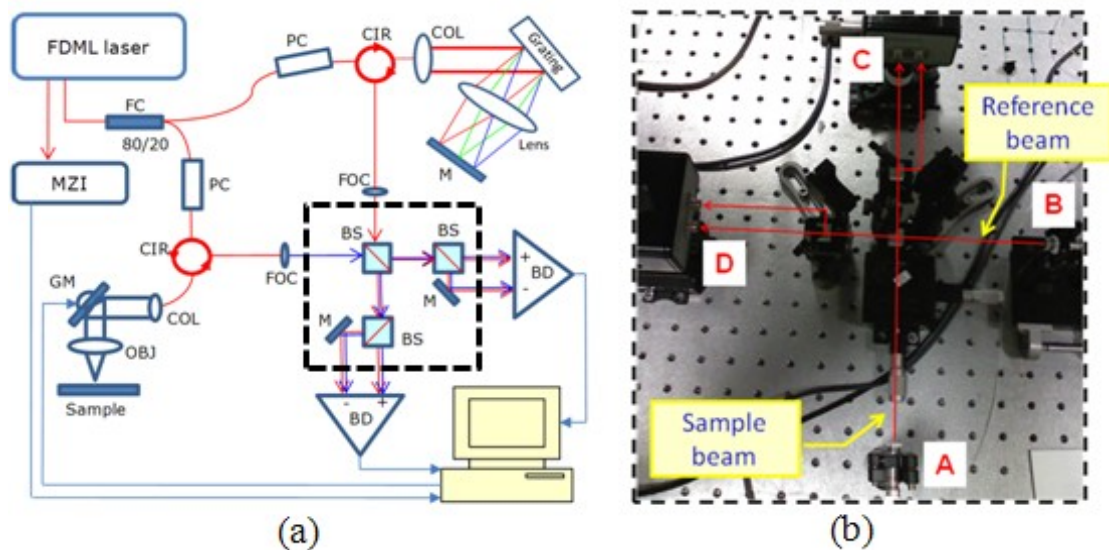


Figure 4.4: (a) The experimental setup of DD-FD-OCT in a hybrid MZI setup. FC: fiber coupler, PC: polarization controller, BS: beam splitter, COL: collimator, M: mirror, GM: galvo mirror, MZI: Mach-Zehnder interferometer, OBJ: Objective, CIR: circulator, FOC: focuser, and BD: balanced detector. (b) The photograph of the free-space section with red arrows indicates optical paths from reference and sample out-couplers to each balanced detector.

The setup of the hybrid DD-FD-OCT is shown in Figure 4.4(a). The MZI configuration allows maximum use of the limited source power as compared with the previously used free space Michelson interferometer setup in section 4.2.1. The output from the light source was

coupled into a fiber system and then split by a 20/80 1x2 fiber coupler. A 20% portion of the power was delivered to the reference arm, in which a Fourier domain optical delay line (FDODL) was implemented in order to compensate for the overall dispersion (Lee et al. 2005). Another portion of the beam was delivered to the sample arm consisting of a collimator, a galvanometer beam steering (VM500, GSI Lumonics), and a 20 mm effective focal length spherical lens. The lateral resolution was estimated to be about 10 to 15  $\mu\text{m}$  as detailed in section 3.1.1. Both sample and reference beams were then coupled back to the fiber system, delivered through fiber circulators and out-coupled through an adjustable focusers to a free space section as indicated by a black dash box in Figure 4.4(a).

In the free-space section, the two beams were interfered and split at the first non-polarizing beam splitter cube with a 50/50 split ratio. The interference signals in both paths were detected by two independent 80 MHz balanced photo-receivers (model 1817, New Focus). A  $\pi/2$  precise and stable phase relation between the two detected signals was achieved through a slight difference in the alignment of the two detection paths in the free space system so that the two optical path length differences, i.e. AC-BC and AD-BD as designated in Figure 4.4(b), were different by the amount of about quarter of the center wavelength of the light source. The two interference signals were then digitized on each channel of a two-channel, high-speed, 12-bit-resolution analog-to-digital converter operating at 200 Msamples/s (NI PCI 5124, National Instrument). The detected spectra were calibrated prior to Fast Fourier Transform (FFT) using the time-frequency relation generated from the position of peaks, valleys, and zero-crossing of an interference signal measured by an additional MZI (Huber et al. 2005a) recorded on another 8-

bit-resolution analog-to-digital converter operating at 250 Msamples/s (NI PCI 5114, National Instrument). The spectral interference signals and the MZI calibration signal were measured synchronously and simultaneously, and the calibration process was done in software (see section 3.1.2).

### 4.3 Results and Discussion

#### 4.3.1 *System Performances*

The example of two acquired spectra with quadratic phase relation, when using a single reflector as a sample, is illustrated in Figure 4.5(a). The two spectra were almost the same except for a  $\pi/2$  phase difference between them. The suppression ratio, which is the ratio between the amplitudes of a signal peak and its mirror counterpart, of about 40 dB (Figure 4.5b) was observed over a long period of operation. It should be pointed out that, in order to get maximum suppression performance, the magnitude of the two spectra should be approximately equal within 2% maximum difference. In this experiment, the 40 dB suppression was achieved by monitoring the plot similar to that in Figure 4.5(b), while adjusting the alignment in the free-space section. Once the maximum suppression was achieved, the magnitudes of the two signals were also well matched. Considering the setup in Figure 4.4, since the two spectra were acquired simultaneously, any movement that occurred in either the reference or the sample arms or both prior to the free-space section equally contributed to the frequency shift in both acquired spectra, and, therefore, did not affect the  $\pi/2$  phase relation between them.

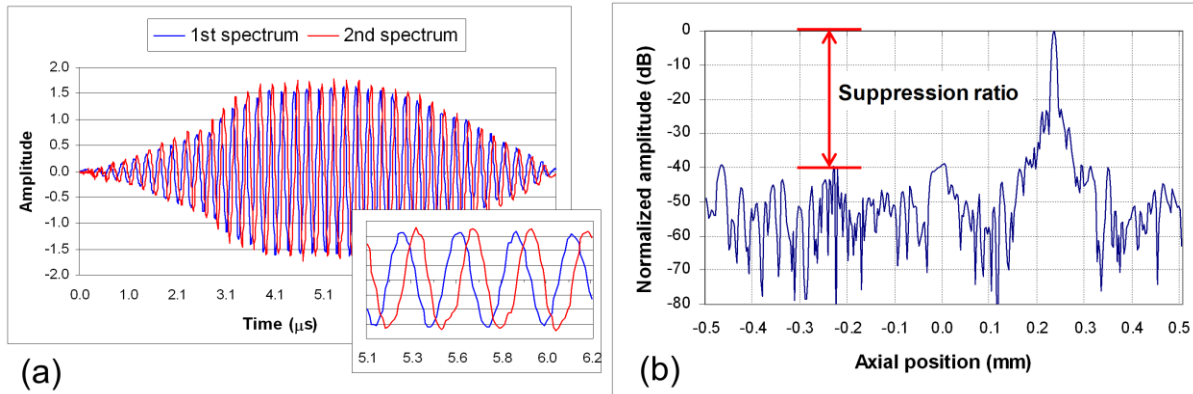


Figure 4.5: (a) Two spectra with quadratic phase relation simultaneously acquired by the dual detection system when imaging a single reflector; (b) A depth profile demonstrates the suppression performance of DD-FD-OCT that corresponds to a case of matching amplitudes of the signals shown in (a) within 2%.

#### 4.3.2 *In Vivo* Imaging of Biological Sample with DD-FD-OCT

In this experiment, an *in vivo* tadpole was anesthetized by embedded inside a 0.001% solution of Tricane mixed with distilled water. The tadpole was left inside the solution for 10 minutes before cross-sectional images were taken. The imaging was performed within a 30 minutes period and then the tadpole was released back to the water chamber after recovery from anesthesia. Figure 4.6 shows a comparison between two images simultaneously taken from an African frog tadpole (*Xenopus Laevis*) with and without full range enabled. A good mirror image suppression performance was observed. The existence of a mirror image causes overlapped structures that are undistinguishable of an actual sample structure. The mirror image was well suppressed by the DD-FD-OCT and hence obscured structures are revealed in the full range image. In addition, an *in vivo* image of a human skin taken from the area around the inner

knuckle joint of the index finger is shown in Figure 4.7. The mirror image removal reveals actual structure at the deep dermis region of the skin.

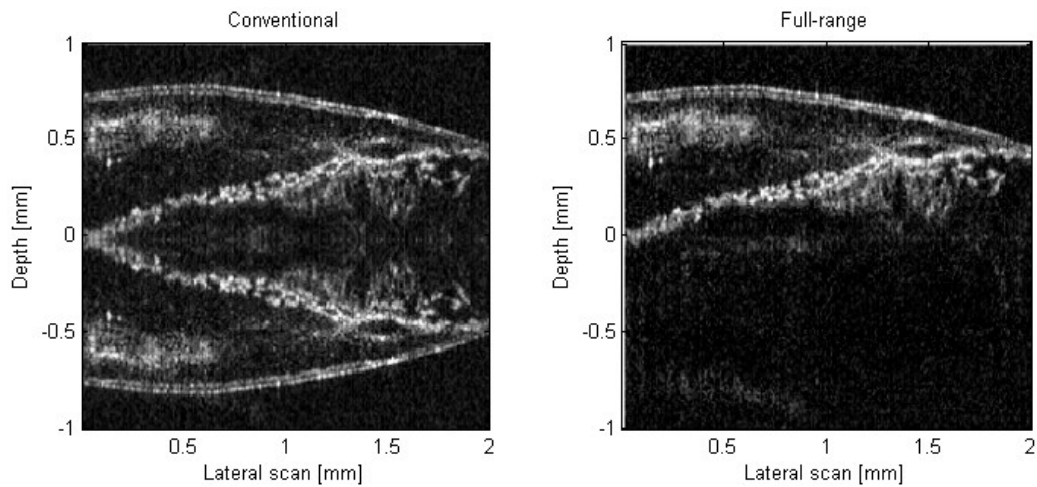


Figure 4.6: *In vivo* full-range images taken from a *Xenopus Laevis* tadpole by using conventional FD-OCT (left) and DD-FD-OCT (right)

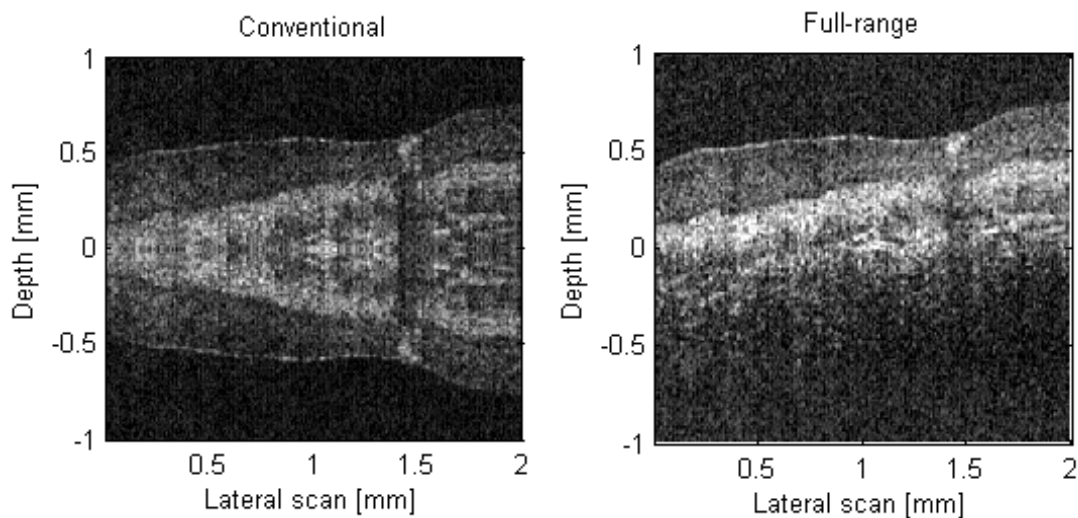


Figure 4.7: *In vivo* image of a human finger joint taken by conventional FD-OCT (left) and full-range DD-FD-OCT (right)



#### 4.4 Summary

A novel technique of full range FD-OCT, namely DD-FD-OCT, has been developed. Using two independent detectors, the technique simultaneously detects two spectral interference signals that have quadratic phase relation. As a result, the two signals construct a complex spectral interference signal that provides an ambiguity-free depth profile after inverse Fourier transform. The simultaneous detection allows retrieval of the full-range signal without loss in acquisition speed as compared to operating with conventional FD-OCT.

Considering cost effectiveness, the technique was implemented in a swept-source based FD-OCT. Both free-space and fiber-based setups were investigated. A fiber-based DD-FD-OCT has the benefits of flexibility, power efficiency, and easy alignment compared with the free-space system. A suppression ratio of up to 40 dB was achieved using the method. The technique allows full-range detection without loss of acquisition speed compared with conventional FD-OCT. The full-range signal acquired by DD-FD-OCT is also less sensitive to the sample motion as compared to other full-range techniques. Moreover, the  $\pi/2$  phase relation between the two signals was well maintained over a long period of operation, which is promising for real time full-range imaging of *in vivo* samples. The *in vivo* images of an African frog tadpole and human finger were demonstrated.

## CHAPTER FIVE: DOPPLER IMAGING WITH DD-FD-OCT

Most of full-range techniques for FD-OCT reported to date utilize the phase relation between consecutive axial lines to construct a complex interference signal, and hence may exhibit degradation in either mirror image suppression performance or detectable velocity dynamic range or both when monitoring a moving sample such as flow activity. This chapter presents the application of DD-FD-OCT to a phase-resolved Doppler imaging without degradation in either mirror image suppression performance or detectable velocity dynamic range that were observed in other full-range Doppler methods.

### 5.1 Introduction

It is evident that the performances of phase-resolved DOCT, such as Doppler sensitivity and accuracy, highly rely on the signal to noise ratio (SNR) of the system (Yang et al. 2003a; Park et al. 2005; Schmoll et al. 2009). Therefore, the ability to employ a maximum SNR out of a given phase-resolved DOCT system is desirable. Unlike conventional FD-OCT, full-range FD-OCT allows the use of the region around the zero-delay position, which is the most sensitive region in FD-OCT. Therefore, the combination of Doppler detection and full-range OCT has the promise to improve both structural and Doppler images.

Nevertheless, the combination of full-range FD-OCT and phase-resolved Doppler imaging is challenging because in most cases, both full-range and Doppler capabilities rely on the phase relation between consecutive axial lines. A Hilbert-transform based full-range DOCT

using the BM-scan method was demonstrated for blood flow imaging of the deep posterior of a human eye (Makita et al. 2009). The technique introduced phase modulation during lateral scanning to produce a frequency shift after Fourier transform and then applied band-pass filtering to remove negative frequency components (see Figure 2.7). However, certain amounts of axial movement cause additional frequency shifts in the transformed domain and could lead to unintentional signal loss after band-pass filtering. Therefore, the presence of high axial motion of the sample could affect mirror suppression performance and lead to a reduction in the detectable velocity range of Doppler imaging as compared to what can be achieved by the same system operated in conventional FD-OCT. Recently, a modified BM-scan method based on a parabolic phase modulation technique was proposed to minimize the effect of sample motion and improve the velocity dynamic range (Jaillon et al. 2010). However, an increase in Doppler phase noise was observed.

A different approach to full-range DOCT was based on a time-frequency analysis technique built on a spectrometer-based FD-OCT system called joint spectral and time domain OCT (Szkulmowski et al. 2008a). Contrary to the phase-resolved technique, the Doppler phase shift information was determined from the amplitudes of Fourier transformations. The Doppler image determined by the proposed technique was demonstrated to be less sensitive with respect to SNR and more accurate at close to maximum detectable velocity limit than that determined by phase-resolved techniques. Nevertheless, the full range signal was achieved by introducing change in the optical path length in the reference arm at a constant speed that caused a reduction in the detectable velocity dynamic range of the Doppler signal by half when operating in the full-

range mode (Szkulmowski et al. 2009). Moreover, the method employed a large number of axial scans, for example 16-40 A-scans, and involved 2D Fourier transformation to determine a single line of velocity map that lead to an increase in both acquisition and processing time compare to phase-resolved DOCT.

Simultaneous phase shifting is promising for Doppler imaging, nevertheless no experimental confirmation has been reported to date. In this chapter, the implementation of DD-FD-OCT for a phase-resolved Doppler imaging is presented. One of the advantages of DD-FD-OCT to Doppler imaging is that the full-range signal is achieved without manipulation of the phase relation between consecutive axial lines. Therefore, the phase information of the full-range signal is almost identical to that acquired by conventional FD-OCT method. Hence the full-range DD-FD-OCT is fully applicable to phase-resolved Doppler detection without reduction in detectable velocity dynamic range as normally encounter in other full-range techniques. In addition, phase-resolved DOCT can utilize the maximum SNR provided by the full-range capability (i.e. the -10 dB sensitivity fall-off range is doubled, and the most sensitive region around the zero path delay can be used).

## **5.2 Experimental Method**

### *5.2.1 Doppler Phase Shift Determination*

The Doppler determination method in a similar manner to that detailed in chapter 3 was employed. Only forward sweep signals were used in the Doppler phase shift calculation. As a

result, the theoretical maximum detectable axial velocity was about 11 mm/s. A block acquisition scheme similar to that detailed in chapter 3 was implemented, where a group of axial profiles used to calculate the Doppler phase shift was acquired at each fixed lateral position of the sample beam. This acquisition scheme minimized the effect of lateral motion of the sample beam to the Doppler phase error (Walther and Koch 2009).

Using the DD-FD-OCT setup, two sets of spectral interference signals were recorded at each lateral position of the sample beam. The signals from both detectors were then quantized by the dual channel analog-to-digital converter as previously detailed in section 4.2. At each channel, the number of sampling points was set so that multiple spectra consisting of both forward and backward sweep signals were recorded. The block of acquired signal was chopped into  $M$  sub-sections containing one forward spectrum per section. Each chopped signal was first calibrated to a linear frequency domain by using the MZI calibration curve (see section 3.1.2), and then Fourier transformed to get the complex depth profile signal. The Doppler phase shift was computed using Eq. (3.9) with  $p = 1$ .

Two scanning protocols were used, namely B-mode and M-mode Doppler imaging. In B-mode Doppler imaging, the step-wise function of voltage was applied to the galvo-mirror. At each position of the galvo-mirror, a block of data containing  $M$  forward spectra were acquired, and then the galvo-mirror was moved to the next position and another set of spectra was acquired. The process was repeated until the desired amount of lateral pixels per image was achieved. Throughout this chapter, a sampling interval of 10  $\mu\text{m}$  was used, (i.e. 200 lateral pixels

correspond to a 2 mm physical dimension). The B-mode Doppler was useful for locating the flow.

In M-mode Doppler imaging, the lateral beam position was fixed at a desired lateral position corresponding to the center of the flow location first determined by the B-mode operation. A constant voltage was applied to the galvo-mirror. Without moving the sample beam, a block of data containing  $M$  forward spectra was acquired. The acquisition was repeated until the desired amount of lateral pixels per image was achieved. The lateral dimension of the M-mode Doppler image provided information about flow characteristics over time. In M-mode acquisition, the time interval between two consecutive lateral pixels was approximately 2 ms. Therefore, an M-mode Doppler image consisting of 200 lateral pixels represents a depth-resolved flow profile over a 400 ms time window. The M-mode Doppler was used in flow measurement verification in section 5.3.3.

### 5.2.2 *Flow Phantom and Pumping System*

To verify the accuracy of the flow velocity measurement of DD-FD-OCT, a flow phantom with known set flow velocity was built. The pumping system is illustrated in Figure 5.1. The flow speed was set by a computer controlled motorized translation stage (DCX-PCI 100 Controller, Precision MicroControl Corp.) with resolution of  $\sim 17$  nm per one revolution of the motor head. The syringe ejected  $200 \text{ mm}^3$  of contained fluid for every 1 mm translation of the stage. Therefore, knowing the translation speed of the motorized stage, the corresponding total flow rate of the system was determined. By assuming a laminar flow profile, the peak flow velocity

( $v_m$ ) was estimated through the relation  $v_m = 2F / (\text{Flow Area})$ , where  $F$  is the flow rate of the system determined by the product of the translation speed of the motorized stage and the ejected fluid volume per millimeter displacement of the syringe (Nave 2010).

The capillary tube was tilted at a fixed angle of  $15.12^\circ$  with respect to the horizontal level as shown in Figure 5.1. This produced the angle between the incident beam and the flow direction of  $74.88^\circ$  at the outer surface of the tube, and hence  $78.86^\circ$  at the flow sample after accounting for refraction in the medium ( $n = \sim 1.35$ ) when the illumination beam was perfectly aligned to the vertical direction. This flow angle was chosen to accommodate for the translation range and the maximum speed of the motorized stage so that the flow speed of up to the maximum detectable limit could be observed.

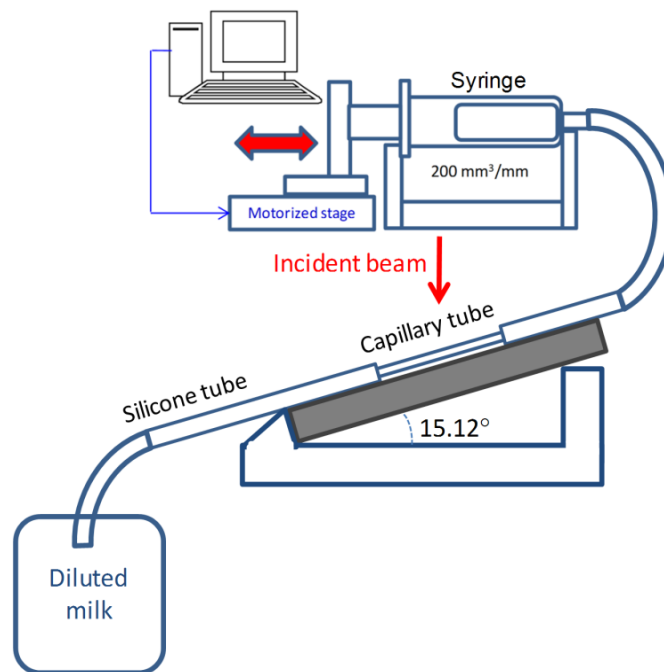


Figure 5.1: Illustration of the flow phantom and pumping system

### 5.3 Results and Discussion

#### 5.3.1 *Phase Stability of the System*

The minimum detectable velocity was determined by the phase stability of the system that could be quantified from the temporal fluctuation of the Doppler phase shift ( $\Delta\phi_{err}$ ) while imaging a static structure, which ideally should be zero. In practice, there was a small deviation of the phase difference even without the presence of moving scatterers. This served as a theoretical limit in velocity sensitivity for each particular DOCT system. Sequentially, the minimum detectable axial velocity was determined by Eq. (3.8).

In this chapter, the minimum detectable axial velocity was quantified in two scenarios: with lateral scanning (B-mode Doppler) and without lateral scanning (M-mode Doppler). Under each imaging scenario, the stability of the Doppler phase shift was monitored over time when using a fixed mirror as a sample (White et al. 2003; Yang et al. 2003a; Schmoll et al. 2009). In this measurement, the SNR was set to be sufficiently high (i.e.  $> 60$  dB) so that the Doppler phase error was solely dominated by the phase stability of the system as set by, for example; the swept source, the interferometer, the scanning mechanics, and the signal processing. The measured phase stability under this condition therefore represented the characteristics and performance of the system. The SNR was quantified by  $(S - \mu_{noise})^2 / \sigma_{noise}^2$ , where  $S$  was the signal peak amplitude at the position of the mirror surface averaged across the full lateral dimension of the acquired Doppler image, and  $\mu_{noise}$  and  $\sigma_{noise}$  were the mean and standard



deviation of the noise floor measured within the region around the signal peak while the sample beam was blocked, respectively (Schmoll et al. 2009). The SNR in dB is defined as  $10\log(\text{SNR})$ .

In the literature, two methods of  $\Delta\phi_{err}$  quantification were used, i.e. by calculating a standard deviation ( $\sigma$ ) (White et al. 2003) and/or a full width at half maximum (FWHM) of the histogram distribution of the Doppler phase shift (Schmoll et al. 2009) measured from a stationary mirror. Since the two methods yield results that differ by a significant order of magnitude, in this experiment, both methods of phase shift error quantification were implemented and compared. The phase shift was averaged over a certain depth range (5 pixels) around the signal peak corresponding with the position of the mirror surface and then averaged across the full lateral dimension (200 pixels) for each acquisition frame of the Doppler image. The measurement was repeated for 500 frames and then both the standard deviation and the FWHM of the histogram of the phase shift errors were computed.

The histogram plots of the measured Doppler phase errors are shown in Figure 5.2. The left (a,c) and right (b,d) columns are histograms of phase shift errors when operating in a conventional FD-DOCT and full-range Doppler imaging using DD-FD-OCT, respectively. To investigate the effect of lateral scanning to the Doppler phase stability, the measurements were performed in both B-mode (a,b) and M-mode (c,d) Doppler imaging. In addition, the minimum detectable axial velocity was calculated by using Eq. (3.8) as shown in Table 5-1.

The results show that high Doppler phase stability was achieved in the implemented DOCT system, i.e. the FWHM Doppler phase error between two consecutive axial lines was less than 3 milliradians (mrad) in all cases. Furthermore, the results quantify the improvement in the

Doppler phase stability and hence the minimum detectable velocity as a function of  $M$ , which was the number of spectra used to calculate the Doppler phase shift (see Eq.(3.9)). In addition, the phase error was slightly increased when operating in the B-mode Doppler compared with the M-mode Doppler demonstrating the effect of scanning mechanics to the system phase stability. In general, one may expect a significant difference in phase errors between the M-mode and B-mode operations. In this experiment, the phase errors were only slightly different since the acquisition scheme was designed so that all spectra used to determine Doppler phase shift were acquired at exactly the same lateral position and hence the effect of transverse motion (Park et al. 2005; Walther and Koch 2009) was suppressed.

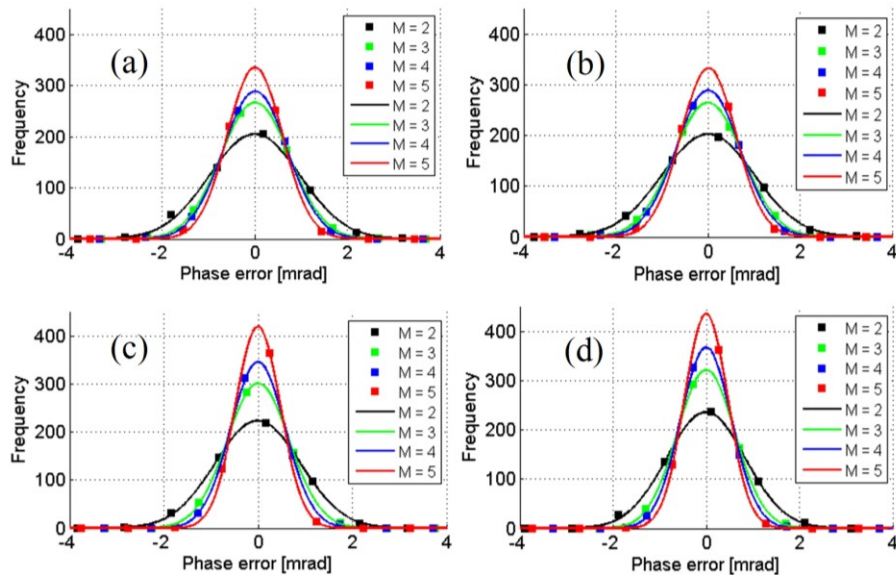


Figure 5.2: Histogram distributions of measured Doppler phase errors where left (a,c) and right (b,d) columns correspond with the measurement data taken with conventional FD-OCT and DD-FD-OCT, and top (a,b) and bottom (c,d) rows correspond with B-mode and M-mode operations, respectively; The measurements were conducted at different values of  $M$ . The filled square markers and the solid lines represent measurement values and the Gaussian fit, respectively.

Table 5-1 The minimum detectable axial velocity at various  $M$  values, where the top (without parenthesis) and bottom (in parenthesis) values in each cell correspond to B-mode and M-mode Doppler imaging, respectively.

$M$	2		3		4		5	
	$\sigma$	FWHM	$\sigma$	FWHM	$\sigma$	FWHM	$\sigma$	FWHM
Conventional FD-OCT								
$\Delta\phi_{err}(\text{mrad})$	1.04 (0.88)	2.29 (2.11)	0.76 (0.66)	1.75 (1.56)	0.69 (0.59)	1.63 (1.36)	0.61 (0.48)	1.41 (1.13)
$V_{a,\min}(\mu\text{m/s})$	3.62 (3.07)	7.98 (7.35)	2.65 (2.30)	6.10 (5.44)	2.40 (2.06)	5.68 (4.74)	2.13 (1.67)	4.91 (3.94)
Full-range DD-FD-OCT								
$\Delta\phi_{err}(\text{mrad})$	0.97 (0.88)	2.33 (1.98)	0.75 (0.63)	1.76 (1.46)	0.69 (0.55)	1.63 (1.28)	0.61 (0.47)	1.40 (1.09)
$V_{a,\min}(\mu\text{m/s})$	3.38 (3.07)	8.12 (6.90)	2.61 (2.20)	6.13 (5.09)	2.40 (1.92)	5.68 (4.46)	2.13 (1.64)	4.88 (3.80)

Moreover, it can be observed from Table 5-1 that the phase stability in conventional FD-OCT and DD-FD-OCT were almost the same, verifying that the phase stability was not affected by the full-range operation in DD-FD-OCT. It should be pointed out that both full-range and conventional results were calculated from the same set of acquired spectra with and without full-range enabled, respectively. Finally, the phase stability quantified by the two methods, i.e. the standard deviation and FWHM, were different by a factor of about two. Therefore, the quantification of Doppler sensitivity by using the standard deviation may have led to an overestimation. The FWHM method should be considered to represent the minimum detectable velocity. The FWHM can be approximated by  $2\sqrt{2\ln 2}\sigma$  or  $2.3548\sigma$  if the measurement data exhibits a Gaussian distribution (Leon-Garcia 2007; Weisstein 2010).

### 5.3.2 Phase Stability in the Presence of Noise

In the previous experiment, the phase stabilities were measured based on high SNR condition, where the noise effect was negligible. Therefore, the phase error was dominated by the system phase error. Under this circumstance, both conventional FD-OCT and full-range DD-FD-OCT exhibited the same phase stability performance. However in the presence of noise, as encountered when imaging biological samples, the phase stability has been shown to degrade as a function of SNR (Yang et al. 2003a; Park et al. 2005; Schmoll et al. 2009).

In this experiment, the Doppler phase stability was measured in B-mode Doppler imaging by using stationary diluted milk as a sample. To demonstrate the effect of SNR fall-off to Doppler phase stability of the system, average Doppler phase errors were measured at different locations of the sample relative to the zero-delay position as shown in Figure 5.3.

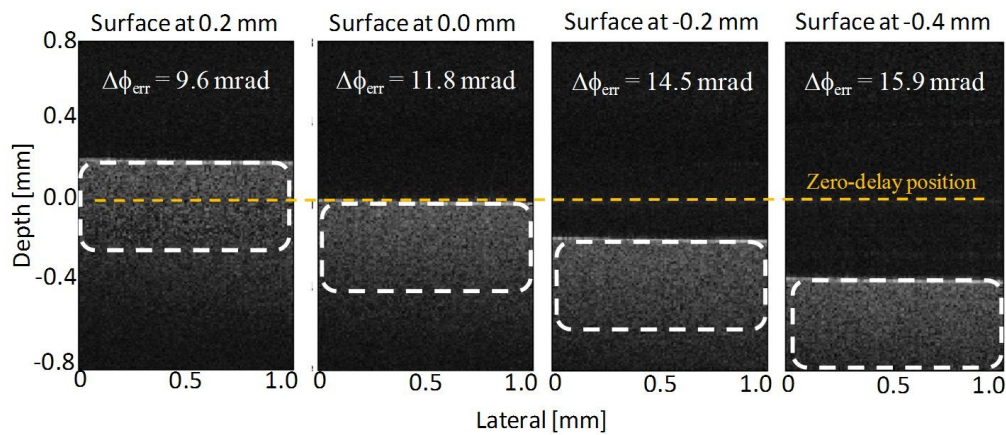


Figure 5.3: Average phase errors measured from stationary diluted milk when the sample surface was placed at different depth positions by changing the optical path length in the reference, where the white dash box indicates the area that the phase error was averaged over in each case, and the orange dash line denotes the zero-delay position.

The position of the sample relative to the zero-delay position was adjusted by changing the optical path length in the reference arm without any modification of the sample arm. The phase error in each case was averaged over the region of interest (ROI) marked by the white dash box in Figure 5.3, i.e. 250 pixels axially and 100 pixels laterally. In each scenario, the measurement was repeated for 200 frames and the standard deviation  $\sigma$  was computed. The Doppler phase sensitivity was then determined as  $2.36\sigma$ , assuming a Gaussian distribution.

The first scenario, where the zero-delay position was placed below the sample surface, only available with full-range imaging, provided best phase stability since the SNR was maximum at the zero-delay position in FD-OCT. The phase error at around the zero-delay position measured at averaged SNR of 20 dB was approximately 10 mrad corresponding to a minimum detectable velocity of about 34  $\mu\text{m/s}$ . This is about a five times degradation from the case of a static mirror measurement. As one may expect, the phase stability degraded as the sample surface was placed further away from the zero-delay position due to the effect of sensitivity fall-off as a function of depth as shown in Figure 5.4.

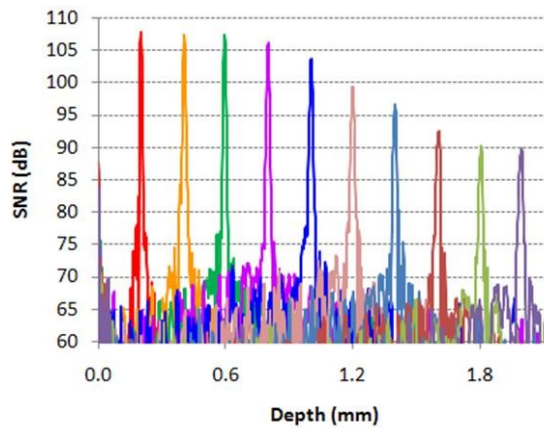


Figure 5.4: Measured SNR (in air) of the system as a function of depth.

The SNR was measured in air by using a perfect mirror as a sample similar to that previously detailed in section 3.1.3. One can observe that the SNR quickly drops at depth beyond 0.6 mm. The 10 dB SNR fall-off distance was at around 1.4 mm in air corresponding to about 1 mm in tissue.

### 5.3.3 *Flow Measurement Verification*

To validate the flow velocity detection capability of the full-range DD-FD-OCT as compared with conventional FD-OCT, we imaged a flow phantom that was diluted milk pumped through a capillary tube of  $\sim 770 \mu\text{m}$  inner diameter by using the pumping system described in section 5.2.2. The cross-sectional intensity images of the flow phantom operated at a flow speed of about 44 mm/s acquired by conventional FD-OCT and DD-FD-OCT are shown in Figure 5.5(a) and (d), respectively. The results demonstrate that the mirror-image removal performance of full-range DD-FD-OCT was not affected by the sample movement caused by the flow activity. Corresponding with the intensity images in Figure 5.5(a) and (d), 2D color maps of B-mode Doppler phase shift detected by conventional FD-OCT and full range DD-FD-OCT are shown in Figure 5.5(b) and (e), respectively. The Doppler phase shift is displayed in colors map, where the amount of Doppler phase shift of  $-\pi$ ,  $-\pi/2$ ,  $0$ ,  $\pi/2$ , and  $\pi$  are mapped to yellow, red, black, blue, and light blue, respectively. In conventional FD-OCT, because of conjugate relation, the mirror image exhibited the same amount of Doppler phase shift but with opposite sign as compared with its counterpart, corresponding to areas appearing in red and blue colors in Figure 5.5(b),

respectively. The mirror Doppler signal is completely invisible in full range DD-FD-OCT as shown in Figure 5.5(e).

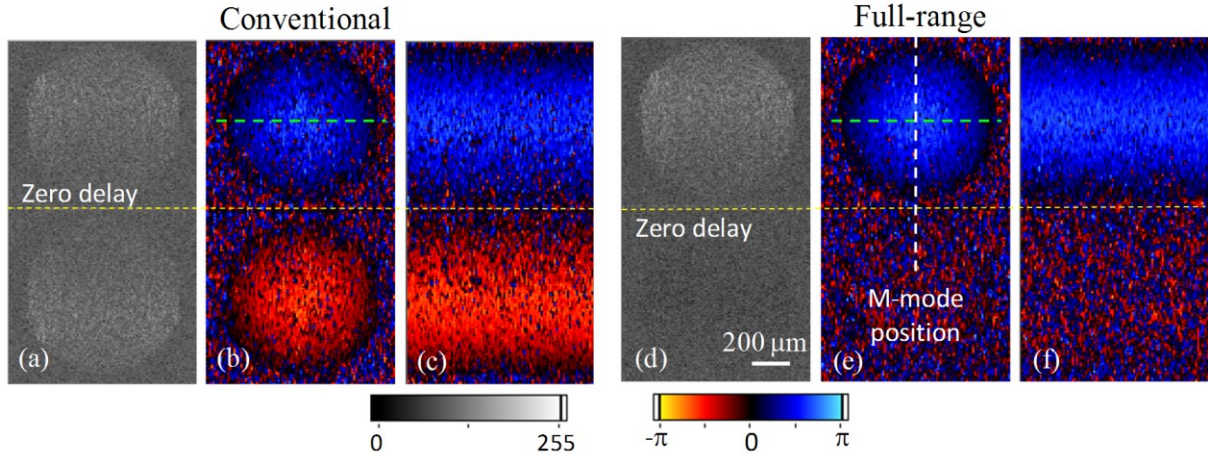


Figure 5.5: (a) and (d) are intensity images, (b) and (e) are B-mode Doppler images, and (c) and (f) are M-mode Doppler images measured by conventional FD-OCT and DD-FD-OCT, respectively, where the yellow horizontal dash line indicate the zero path delay position, the white vertical dash line indicates the lateral position where the M-mode Doppler was operated, and the white solid line at the bottom right of (d) denotes the scale bar that is applied to all images (a-f).

Furthermore, Doppler phase shifts at various set flow speeds of the flow phantom were measured. The phase shift was determined by using Eq. (3.9) with  $p = 1$  and  $M = 5$ . The flow angle was set at approximately 78.86 degree after accounting for the refraction of the beam. Since the incident angle was quite wide, the actual illumination power at the sample was dramatically decreased due to the strong reflection at the outer surface of the capillary tube based on Fresnel reflection. This led to the presence of random phase for the background noise over the flow cross-section area. To minimize this effect and achieve a smooth flow profile, a 1D median filter was applied to every axial line of the M-mode Doppler image. The median filter is an

efficient method for removing salt-and-pepper noise while minimally altering neighbor pixels (Gonzalez and Woods 2002).

At each set flow velocity, two Doppler images, determined by conventional FD-OCT and full-range DD-FD-OCT enabled, were calculated from the same set of acquired spectra. All Doppler images acquired with conventional FD-OCT were established from the signal from one of the two detectors since the measured SNR performances of the 1<sup>st</sup> and 2<sup>nd</sup> detection systems as well as the full-range system were almost identical given that the difference was less than 1 dB. Therefore, Doppler images obtained by both systems exhibit similar Doppler sensitivity. It is most important to compare the performances of conventional FD-OCT and full-range DD-FD-OCT by using the same set of data to ensure that they were measured in exactly the same conditions (i.e. same lateral position of the sample beam and same condition of the flow sample).

To measure the peak flow velocity, the center of the flow area, marked as a white dash line in Figure 5.5 (e), was determined from a B-mode Doppler image (Figure 5.5 (b,e)). Then the lateral position was fixed at that position and an M-mode Doppler image (Figure 5.5 (c,f)) was taken. Each M-mode Doppler image consisted of 800 pixels along the depth axis (vertical axis) centered at zero-delay position as indicated by a yellow dash line in Figure 5.5 and 200 pixels along the time axis (horizontal axis). The M-mode Doppler color maps corresponding with various flow velocities set by the pump from no flow to 59 mm/s are demonstrated in Figure 5.6, where negative and positive velocities represent flow in opposite direction.



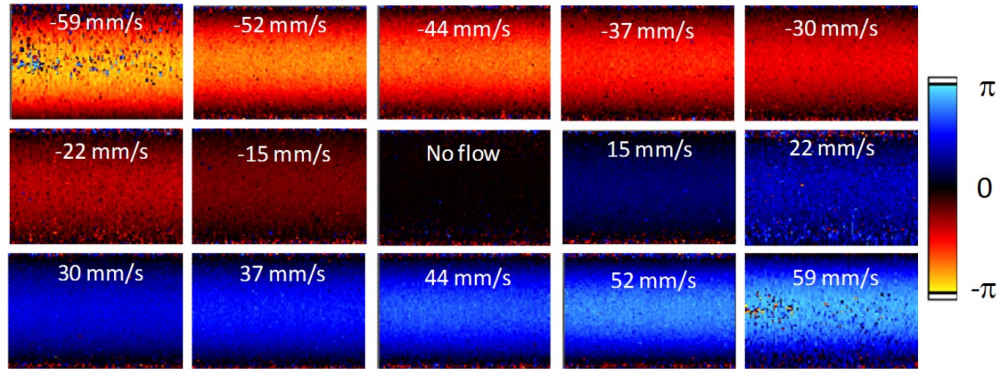


Figure 5.6: M-mode Doppler images calculated from the full-range signal at various flow velocities set by the pump

Sequentially, the peak flow velocity from each acquired M-mode Doppler image was determined. The phase shift was first averaged along the time axis yielding an averaged phase-depth profile, and then averaged from 5 pixels around the peak of the profile. To minimize the effect of slow fluctuation over time of the flow speed intrinsic to the characteristic of the pump, the measurement was repeated for 200 frames of M-mode Doppler images acquired at 2 fps. This frame rate provided measurement data that included several cycles of the slow flow fluctuation over time. The mean and standard deviation were computed representing a Doppler phase shift at the peak of the flow profile for each set flow speed of the flow phantom. Finally, the peak velocities were calculated and compared to those estimated from the pump parameters.

The absolute flow velocities were determined by using  $V(z) = V_{axial}(z)/\cos\theta$ , where  $V_{axial}(z)$  was determined by Eq. (3.6). Using the system's parameters that were  $\lambda_0 = 1320$  nm,  $T = 22.4$   $\mu$ s,  $\theta = 78.86$  degree, and  $n = \sim 1.35$ , Doppler velocity corresponding to each set velocity of the pump was calculated and compared as shown in Figure 5.7. From Table 1, at  $M = 5$ , the

measured Doppler phase error was  $\sim 1$  mrad, and the minimum detectable axial velocity was computed to be  $\sim 4$   $\mu\text{m/s}$  corresponding to an absolute flow speed of 21  $\mu\text{m/s}$  at 78.86 degree. In this measurement, the average SNR at around peak flow location was about 15 dB. When imaging such a weak backscattering sample, the presence of noise degraded the Doppler phase sensitivity to about 24 mrad (FWHM) that corresponded with the minimum detectable absolute flow velocity of about 0.45 mm/s at the flow angle of 78.86 degree in both cases of the conventional and the full-range operations as determined by  $2.36\sigma$  of the measurement data at no flow (see Figure 5.7).

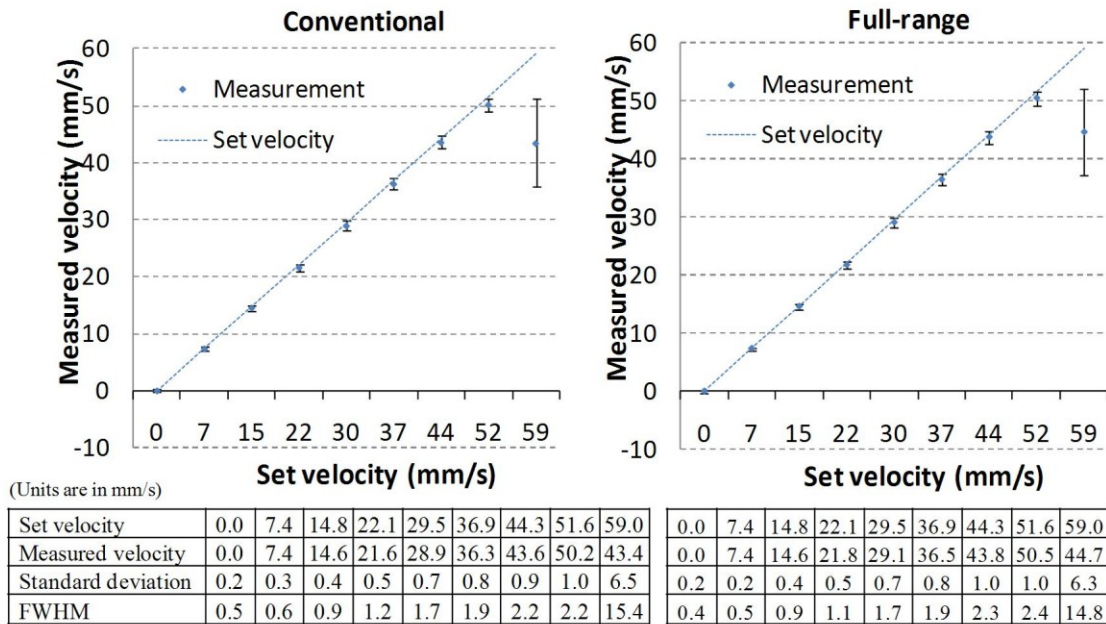


Figure 5.7: Plots of the measured velocity at the peak of the flow profile and the set flow velocity measured by conventional FD-OCT (left) and full-range DD-FD-OCT (right). 200 measurements were performed at each set flow velocity. Each data point corresponds to a mean value, and the size of the error bar at each measurement point represents the FWHM of the distribution of the measured Doppler phase shift estimated by  $2.36\sigma$  assuming a Gaussian distribution.

Furthermore, as the flow speed was increased, the standard deviation of the measured Doppler phase shift was further broadened particularly at high flow velocity, i.e. from 30 mm/s to 59 mm/s. This broadening was induced by flow fluctuation caused by the pump especially when traveling over a long distance of the motorized stage. The fluctuation was intrinsic to the characteristic of the pump and hence affected both the conventional and the full-range measurements by almost the same amount as shown in Figure 5.7. Nevertheless, this fluctuation tended to occur in cycle, and therefore the measured flow speed was still acceptable, compared with the set flow speed, after averaging over a long period of time except for the last measurement at  $\sim 59$  mm/s, which is beyond the maximum detectable velocity of the system as limited by the  $\pi$  phase ambiguity. At the set flow speed of  $\sim 59$  mm/s, the fluctuation tended to occasionally cross the  $\pi$  phase ambiguity boundary, which corresponded to an absolute flow velocity of  $\sim 57$  mm/s, and hence suffered from phase wrapping and could not provide a correct measurement as can be observed in both plots in Figure 5.7.

Finally, Doppler imaging of blood flow inside the heart of an African frog tadpole using the full-range DD-FD-OCT system was demonstrated, as shown in Figure 5.8. Two intensity images of the tadpole heart in comparison between conventional FD-OCT and full-range DD-FD-OCT processed from the same set of acquired spectra are shown in Figure 5.8(a) and (b), respectively. The flow activity can be observed in the corresponding Doppler maps as shown in Figure 5.8(c) and (d), where the mirror Doppler is completely suppressed in the full-range mode (Figure 5.8d) as compared with that processed in conventional mode (Figure 5.8c). The flow activity was observed at the location indicated by a white arrow in Figure 5.8(b). With the full-

range capability, one can place the region of interest close to the zero-delay position, and utilize the high SNR around this region to improve Doppler sensitivity.

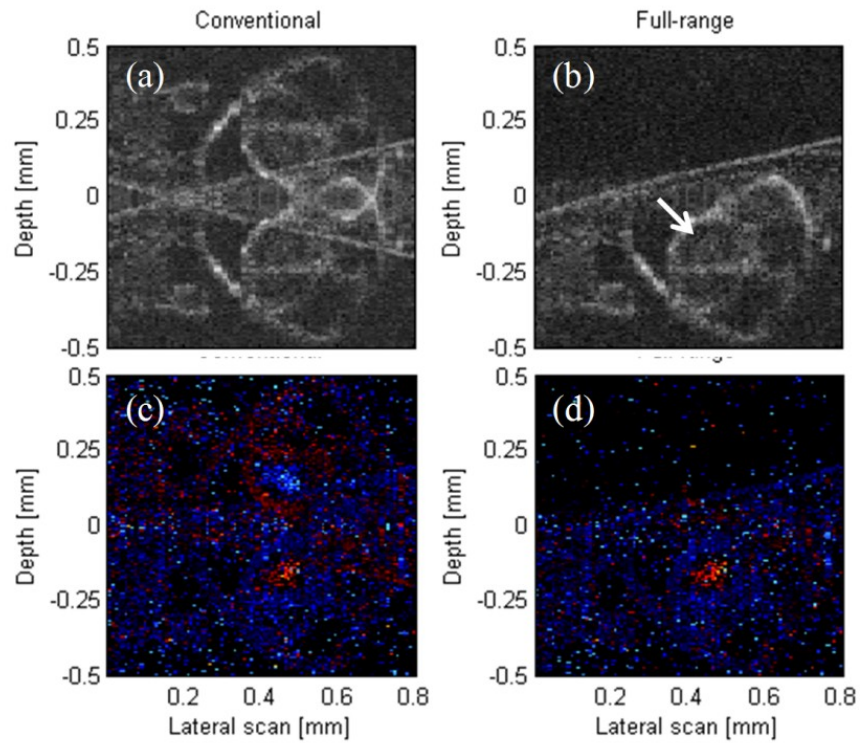


Figure 5.8: (a) and (b) are intensity images and (c) and (d) are corresponding Doppler images of the heart of an African frog tadpole processed with and without full-range enabled, respectively. The white arrow in (b) indicates the location of the flow activity displayed in (d).

#### 5.4 Summary

In summary, the feasibility of the full-range DD-FD-OCT method to achieve Doppler detection without degradation of the mirror image suppression performance and without any loss in velocity dynamic range compared with conventional FD-OCT was demonstrated. The Doppler

phase stability of DD-FD-OCT was quantified and compared with that achieved by the conventional method. In addition, the Doppler phase shifts corresponding to different flow velocities produced by the flow phantom were measured and verified. Finally, the Doppler image of blood flow inside the heart chambers of an African frog tadpole using the full-range DD-FD-OCT was demonstrated. The full-range capability allows for the placement of the flow region close to the zero-delay position and hence improves flow visibility and sensitivity, which is particularly useful for imaging of biological samples.

## CHAPTER SIX: GABOR DOMAIN OPTICAL COHERENCE MICROSCOPY

Gabor-Domain Optical Coherence Microscopy (GD-OCM) utilizes the high speed imaging of FD-OCT, the high lateral resolution of OCM, and the ability of real time refocusing of a custom design dynamic focus objective. GD-OCM acquires multiple cross-sectional images corresponding to a discrete refocusing step along depth enabled by the recently developed dynamic focus probe. By acquiring multiple images that focus differently along depth, a method that efficiently extracts and then fuses together in-focus portions, ultimately in real time, is necessary. In this chapter, the technique of extraction as well as automatic fusion of in-focus portions of the acquired cross-sectional images for GD-OCM is detailed.

### 6.1 Mathematical Description of GD-OCM

The use of high NA imaging optics with a high-speed variable focus capability within an OCM experimental setup (Murali et al. 2009), combined with a Gabor-based image fusion algorithm is referred to as Gabor Domain OCM (GD-OCM) (Rolland et al. 2010a), to distinguish the acquisition and processing from FD-OCM. In conventional FD-OCT (see section 2.2), the Fourier transform of the detected spectral interference signal yields

$$I_{OCT}(z_D) = 2r_R \cdot \mathfrak{F}^{-1}\{\hat{S}(k)\} * r_S(z_D), \quad (6.1)$$

In GD-OCM, the low ( $< 0.1$ ) NA objective lens that is typically used in FD-OCT to ensure long DOF is replaced by a higher NA variable focus objective (e.g.  $NA \geq 0.2$ ). Intrinsic to the use of high NA imaging optics, the illumination power is peaked at the focus point of the objective and rapidly drops as a function of the distance away from that point (Born and Wolf 1999; Dubois et al. 2002; Davis et al. 2007); but most importantly, the lateral resolution is maintained in an even smaller region around the focus point, known as the DOF, which may be based on a variety of image quality criteria. In this work, the DOF is defined by the region over which the MTF exceeded 10% at 177 lp/mm. This region may be shown to be equivalent to about five times the conventional quarter wave criteria established by Rayleigh, which means that the defocus aberration of about 1.25 waves is tolerated (Born and Wolf 1999). Using a window localized at a given focus and extended in depth, only the back-scattering events that happen around the focus, approximately inside the DOF region defined above, will dominantly contribute to the detected spectral interference, and hence the final image. Using the expression for the spectral reflected field given by Eq. (2.2) together with the GD-OCM imaging property, the electric field from the sample arm can be modified as

$$\hat{E}_S(k; z_{S0}) = K_S \hat{E}_0(k) \int_{-\infty}^{+\infty} g(z_S - z_{S0}) \cdot r_S(z_S) \exp(ikz_S) dz_S, \quad (6.2)$$

where  $g(z_S - z_{S0})$  denotes the window whose shape will be described in section 6.3. In all cases, the window shape will be approximated by a function that concentrates around the position  $z_S$  equals to  $z_{S0}$  and has a finite width, which is much narrower than the function

$r_S(z_S)$ . The window serves as a weighting function along the depth centered at the focal plane of the imaging optics located at  $z_{S0}$ . By assuming there is no loss in both paths, i.e.  $K_R = K_S = 1$ , in a similar manner to the derivation of the conventional FD-OCT in section 2.2, the detected spectral interference signal is now given as

$$\hat{I}_{\text{int},c}(k; z_{D0}) = 2r_R \hat{S}(k) \int_{-\infty}^{\infty} g(z_D - z_{D0}) \cdot r_S(z_D) \exp(ikz_D) dz_D . \quad (6.3)$$

It should be pointed out that the spectral interference signal is now a function of two variables, the optical frequency and the position of the focal plane. Furthermore, the integration term is in the form of a local Fourier transform or Gabor transform, where the DOF serves as a weighting window whose center may be shifted by varying the focal length of the dynamic focus probe. In the process of reconstruction of the full depth profile, a new function is defined as

$$\hat{F}(k; z_{D0}) = \int_{-\infty}^{\infty} g(z_D - z_{D0}) \cdot r_S(z_D) \exp(ikz_D) dz_D . \quad (6.4)$$

Hence the depth profile can be reconstructed by means of an *inversion of the local Fourier transform* (Barrett and Myers 2004) defined by

$$r_S(z_D) = \int_{-\infty}^{\infty} \int_{-\infty}^{\infty} \hat{F}(k; z_{D0}) \cdot \frac{g(z_D - z_{D0})}{\|g\|^2} \exp(-ikz_D) dz_{D0} dk , \quad (6.5)$$



where we define  $\|g\| = \left[ \int_{-\infty}^{\infty} |g(z_D)|^2 dz_D \right]^{\frac{1}{2}}$  for the purpose of normalization of the window.

Furthermore, using the concept of the *Gabor's signal expansion* (Barrett and Myers 2004), the sampled version of Eq. (6.5) can be expressed as

$$r_S(z_D) = \sum_{m=-\infty}^{\infty} \sum_{n=-\infty}^{\infty} \hat{F}(k_n; m\delta z_D) \cdot \frac{g(z_D - m\delta z_D)}{\|g\|^2} \exp(-ik_n z_D), \quad (6.6)$$

where the signal  $\hat{F}(k_n; m\delta z_D)$  corresponds to an interference fringe of the detected spectral interference signal acquired for every shift of the focal plane of the dynamic focusing probe by an amount of  $\delta z_D$ . Eq. (6.6) can be rearranged into a desired form as

$$r_S(z_D) = \sum_{m=-\infty}^{\infty} \frac{g(z_D - m\delta z_D)}{\|g\|^2} \sum_{n=-\infty}^{\infty} \hat{F}(k_n; m\delta z_D) \cdot \exp(-ik_n z_D). \quad (6.7)$$

The inner sum is now in the form of an inverse discrete Fourier transform. By defining the second sum in Eq. (6.7) as  $r_{S,m}(z_D, m\delta z_D)$ , which represents a backscattering event that occurs within the optical path length difference  $z_D$  and within the DOF of the dynamic focusing objective when the focal plane is shifted by an amount  $m\delta z_D$ , Eq. (6.7) can then be rewritten as

$$r_S(z_D) = \sum_{m=-\infty}^{\infty} \frac{g(z_D - m\delta z_D)}{\|g\|^2} \cdot r_{S,m}(z_D, m\delta z_D). \quad (6.8)$$

By inserting Eq. (6.8) into Eq. (6.1), one get

$$I_{OCT}(z_D) = 2r_R \cdot \mathfrak{F}^{-1}\{\hat{S}(k)\} * \sum_{m=-\infty}^{\infty} \frac{g(z_D - m\delta z_D)}{\|g\|^2} \cdot r_{S,m}(z_D, m\delta z_D), \quad (6.9)$$

$$I_{OCT}(z_D) = \sum_{m=-\infty}^{\infty} \frac{g(z_D - m\delta z_D)}{\|g\|^2} \cdot 2r_R \cdot \mathfrak{F}^{-1}\{\hat{S}(k)\} * r_{S,m}(z_D, m\delta z_D), \quad (6.10)$$

$$I_{OCT}(z_D) = \sum_{m=-\infty}^{\infty} \frac{g(z_D - m\delta z_D)}{\|g\|^2} \cdot I_{OCT,m}(z_D, m\delta z_D), \quad (6.11)$$

where  $I_{OCT,m}(z_D, m\delta z_D) = 2r_R \cdot \mathfrak{F}^{-1}\{\hat{S}(k)\} * r_{S,m}(z_D, m\delta z_D)$  is the signal acquired at focus position shifted by an amount  $m\delta z_D$ . Eq. (6.11) expresses that the full depth profile of the sample reflectivity can be reconstructed from multiple images acquired by shifting the focal plane along the depth direction, which from this point on will be referred to as *GD-samples*.

## 6.2 GD-OCM Implementation

GD-OCM was implemented using the setup shown in Figure 6.1. The light source was a Ti:Sa femtosecond laser (Integral<sup>TM</sup>, Femtolaser Inc.) centered at 820 nm wavelength and having a full-width half-maximum bandwidth of 120 nm. An output beam was coupled to a fiber-based Michelson interferometer built on an 80/20 split ratio 2x2 fiber coupler (NSF-DARPA/PTAP). A portion of the beam with 20% of the power was delivered to a reference arm consisting of a fiber polarization controller to maximize the interference signal and a Fourier-domain optical delay line for dispersion compensation (Lee et al. 2005). 80% of the power was delivered to the sample

arm and then coupled to the dynamic focus objective. Integrated into the probe, the lateral scanning was performed by a galvo-mirror scanner (VM500, GSI Lumonics). The two beams were coupled back to the fiber system, interfered through the fiber coupler, and then detected by a commercial spectrometer with a 3648 line CCD array (HR4000, Ocean Optics Inc). The signal processing includes DC-subtraction, linear frequency calibration, fast Fourier transform, and logarithmic intensity mapping.

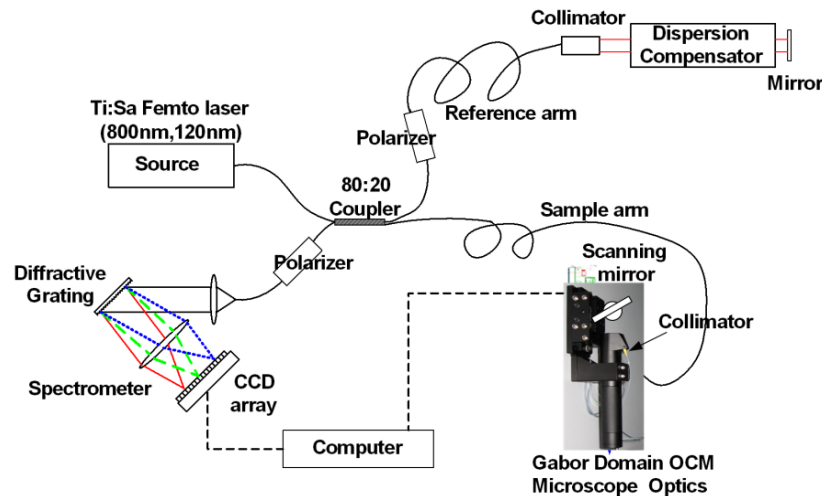


Figure 6.1: An experimental setup for GD-OCM

The image acquisition of GD-OCM involves C-mode scanning adopted from an ultrasound imaging technique, in which multiple cross-sectional images are acquired corresponding with a discrete refocusing step along depth (Sherar et al. 1987; Huber et al. 2005b). However, in GD-OCM, C-mode scanning is enabled by the variable focus objective that changes the focal plane without mechanical movement of the element inside the probe. The focal shift corresponds with an applied voltage that is generated by a digital-to-analog converter (PCI 6115, National Instrument) connected to a personal computer through a standard PCI interface.

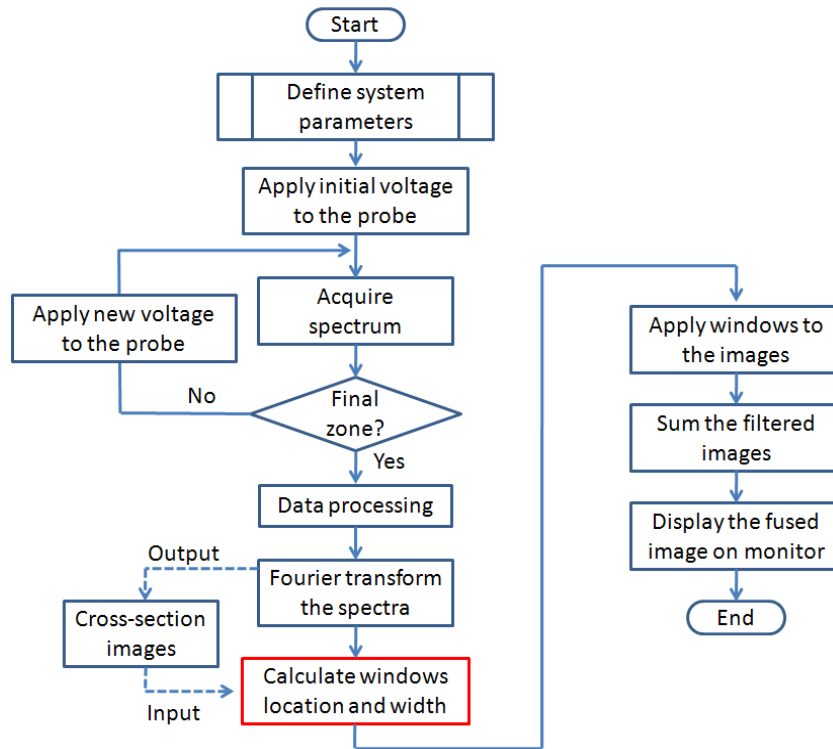


Figure 6.2: Flow diagram of the imaging procedure of GD-OCM

The flow diagram of the GD-OCM system is illustrated in Figure 6.2. First, all system parameters were defined including exposure time of the CCD camera, number of spectra/frame, number of zones, and an applied voltage for each zone. The number of zone was determined by dividing the desire imaging depth range by the DOF. The applied voltages were determined from the measured relation between the applied voltage and the focal shift distance of the DF probe. The first voltage was then applied and the spectra were acquired for a single frame. The process was then repeated for the next applied voltage until all zones were acquired. The data processing included DC subtraction and linear frequency calibration. Sequentially, the calibrated spectra were Fourier transformed yielding multiple intensity images illustrated in Figure 6.3. A filtering

window was calculated and then applied to each corresponding GD-sample as will be detailed in the next section. Finally, the filtered GD-samples were summed yielding the final image that contains mainly in-focus details for an entire cross-sectional area.

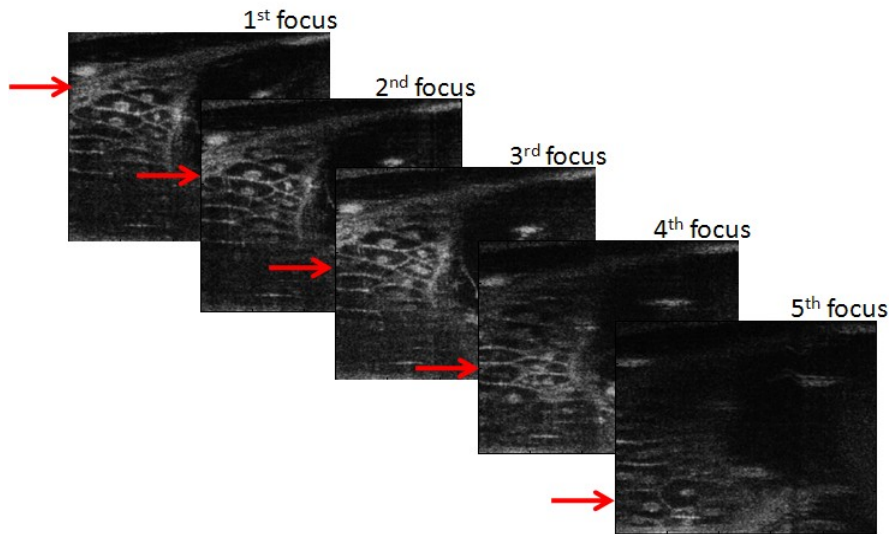


Figure 6.3: Acquired images or GD-samples after Fourier transform and logarithmic intensity mapping

## 6.3 Gabor-Based Fusing Method

### 6.3.1 *Fusing Algorithm*

Given the formalism provided in section 6.1, an automatic fusion algorithm that is capable of extracting and fusing the acquired GD-samples was developed. Each GD-sample is multiplied by a weighting window, whose width is based on the measured DOF of the DF probe, as will be described, and the center is shifted to the position that corresponds to the focus position of that

particular GD-sample. When combined with the variable focus capability of the custom-designed dynamic focusing probe, the image resolution, which is quasi-invariant throughout the imaging depth, can be reconstructed.

To evaluate the imaging capability using the DF probe and the Gabor-based fusion technique, multiple images from the same 0.5 mm x 0.5 mm (lateral x axial) portion of an African frog tadpole (*Xenopus Laevis*) at five different focus positions were acquired as shown in Figure 6.3. The focal plane was shifted by approximately 100  $\mu\text{m}$  along the axial direction that corresponded to the measured DOF of the DF probe. The data in each B-scan or 2D slice contained 500 A-scans with a sampling interval of 1  $\mu\text{m}$ . The measured lateral resolution was 2.8  $\mu\text{m}$  using a 10% MTF criteria at the two edges of the DOF, and 2  $\mu\text{m}$  at best focus position. For each image, the high lateral resolution and sensitivity were observed (as expected) only within a certain region around the focal plane (i.e. within the DOF).

The flow diagram of the construction of the weighting windows used in Gabor based fusing is illustrated in Figure 6.4. A trapezoidal shape that is a flat top with linear transition at both edges was chosen as the windowing function to define and weight the DOF region. The center and width of the windows were automatically and adaptively determined and dynamically applied for each focus position as now detailed. The window's center and width were first estimated from the relation between the applied voltage and the focal shift for each acquired image. The algorithm was then applied to determine the optimal focus position defined as the center of mass (*CM*) of the averaged reflectivity profile for each image over a certain depth range around the estimated focus position.

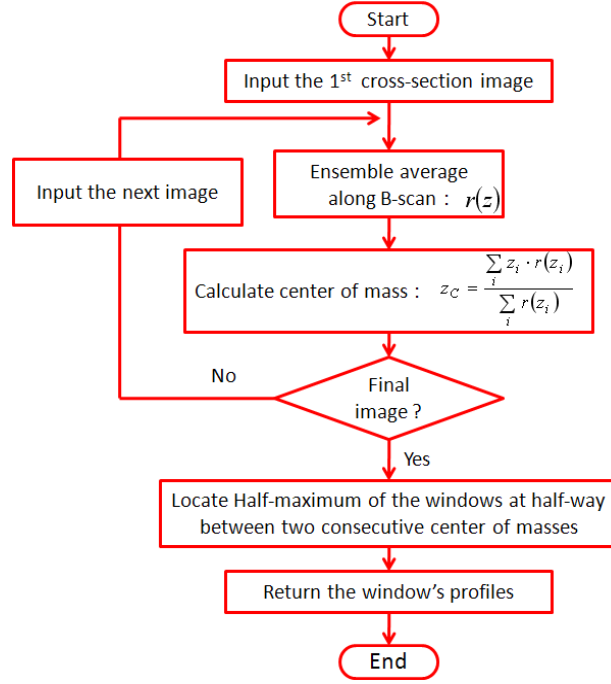


Figure 6.4: Flow diagram of adaptive weighting windows construction

Specifically, the averaged reflectivity profile along the depth was calculated by taking the ensemble average along the lateral scan of each image as  $r_j(z) = (1/N_x) \cdot \sum_x r_j(x, z)$ , where  $r_j(x, z)$  represents the  $j^{\text{th}}$  cross-sectional image,  $x$  and  $z$  are lateral and axial pixels, respectively, and  $N_x$  is a number of axial lines per frame. Then, the  $CM_j$  of each profile  $j^{\text{th}}$  was calculated around the estimated focus position using

$$CM_j = \frac{\sum_z z \cdot r_j(z)}{\sum_z r_j(z)} . \quad (6.12)$$

Sequentially, the left half-maximum point of the  $j^{\text{th}}$  window  $HM_{j,L}$  and the right half-maximum point of the  $j^{\text{th}}$  window  $HM_{j,R}$  were given by

$$\begin{aligned}
HM_{j,L} &= 0.5(CM_j + CM_{j-1}), \\
HM_{j,R} &= 0.5(CM_j + CM_{j+1}).
\end{aligned} \tag{6.13}$$

Finally, the trapezoidal window was constructed as

$$W_j(z) = \begin{cases} \frac{1}{T} \left[ z - \left( HM_{j,L} - \frac{T}{2} \right) \right], & \text{for } HM_{j,L} - \frac{T}{2} < z < HM_{j,L} + \frac{T}{2} \\ 1, & \text{for } HM_{j,L} + \frac{T}{2} \leq z \leq HM_{j,R} - \frac{T}{2} \\ 1 - \frac{1}{T} \left[ z - \left( HM_{j,R} - \frac{T}{2} \right) \right], & \text{for } HM_{j,R} - \frac{T}{2} < z < HM_{j,R} + \frac{T}{2} \\ 0, & \text{elsewhere} \end{cases} \tag{6.14}$$

where  $T$  is a transition width of the window, which is a free parameter. A transition zone of about 20 pixels provides both a sharp cutoff for out-of-focus imagery together with smooth transition between the fused zones. The width of the transition zone is however quite insensitive to variations up to  $\pm 10$  pixels. These linear transitions provide smooth fusion at boundaries. It should be pointed out that summing all windows together yields an overall flat response as shown in Figure 6.5, thus preserving the original intensities in the images around each focus point.

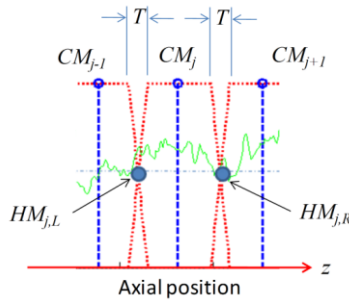


Figure 6.5: Mathematical definition of the window for Gabor domain OCM



### 6.3.2 *Imaging Speed*

In this early implementation, spectra were acquired by using a commercial spectrometer with a 3648 line CCD array (HR4000, Ocean Optics Inc) with an exposure time of 50  $\mu$ s and 4 ms readout time corresponding to a readout speed of 250 spectra/s; thus 500 spectra that form one frame were acquired in precisely 2.025 seconds. Using Labview software, performing the FFT on 500 spectra currently takes less than 5 seconds, and other operation times are negligible. Five frames are thus acquired and processed in about 35.5 seconds, accounting for the 100 ms refocusing of the liquid lens between frames. The fusion algorithm is currently implemented in Matlab and embedded in the Labview code and takes about 400 ms, thus yielding a current processing time of less than 36 seconds.

### 6.3.3 *Fusing Results*

Figure 6.6(a) shows GD-samples acquired at five different focus positions. Each GD-sample was multiplied by a corresponding trapezoidal window (see Figure 6.6b), yielding only in-focus portion as shown in Figure 6.6(c). The filtered images were then summed to form a high-resolution image with extended DOF image as shown in Figure 6.6(d). If one considers the image in position 4 that contributed to the GD-OCM image, the white arrow points to a dominant feature that could be thought to be problematic in accurately computing the placement of the window. It should be pointed out that this feature is out of focus in the 3<sup>rd</sup> position image.

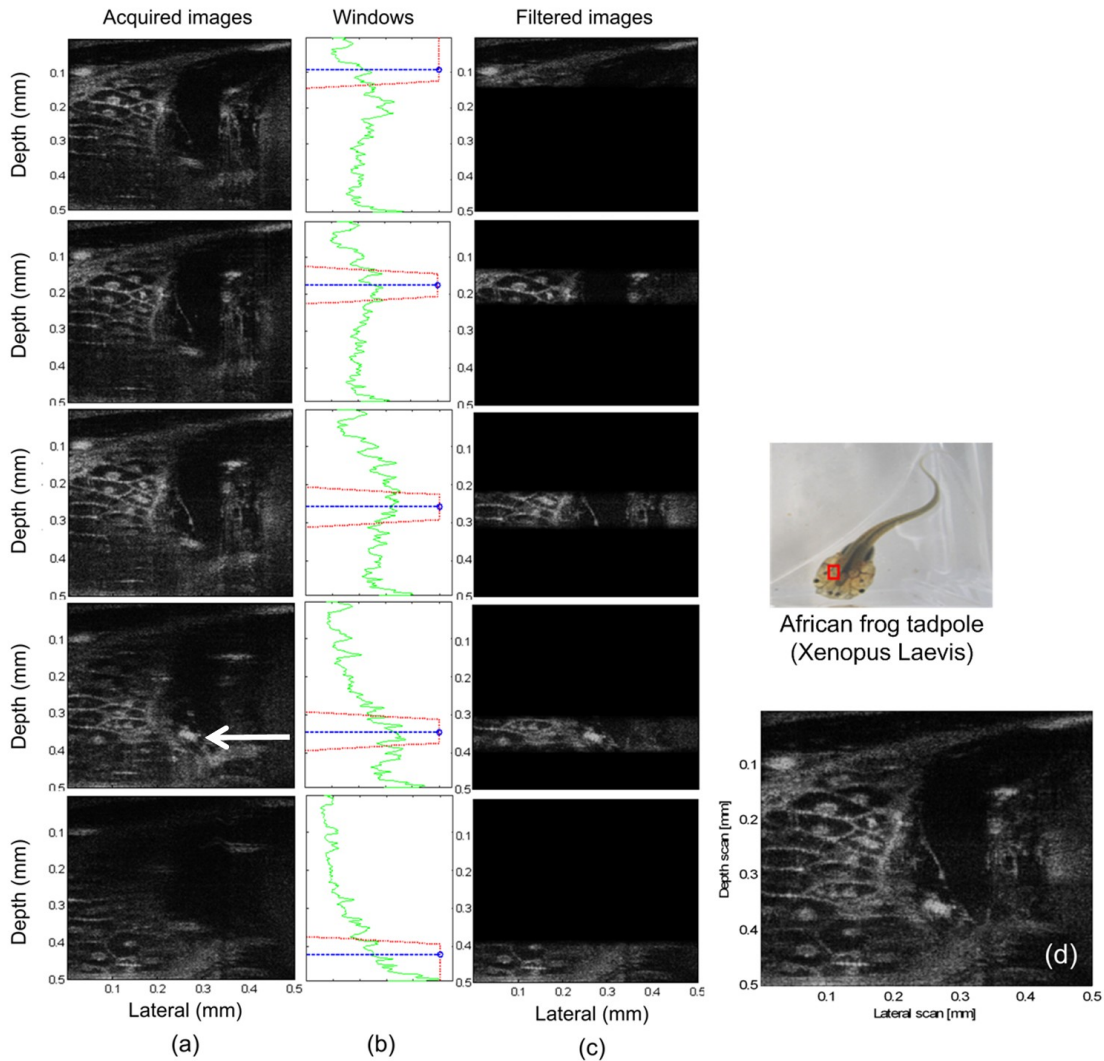


Figure 6.6: (a) OCM Images of an African Frog Tadpole (*Xenopus laevis*) each acquired with the optics focused every 100  $\mu\text{m}$  apart in depth from 0 to 0.5 mm; the white arrow points to a dominant feature (b) A plot of each window profile superimposed on top of an averaged reflectivity profile (c) Filtered images (d) The filtered images were then summed using a Gabor-based fusion algorithm.

While a dominant feature could create a critical issue if the window placement was computed based on an entire depth scan, it is important to note that the computation of the centroid location was carried out only within the DOF region around the estimated location of

the focus based on an initial calibration of the probe. Thus, strong reflections outside the estimated focus range were excluded. Furthermore, the calculated positions of CMs were only used to locate the half-maximum points of the windows, where the linear transition took place. Therefore, the actual center of the window was not necessarily the same as the position of the CM. While a slight shift in the placement of the centroid for a specific image may still occur, the approach has been found to be robust to the precise placement of the window when computed within the estimated focus position of the focusing probe.

In addition, two images acquired using the same probe by GD-OCM and that acquired with conventional FD-OCM image are shown in Figure 6.7(a) and (b), respectively. The image acquired by GD-OCM shown in Figure 6.7(a) provides better details across larger depth range compared to that of a conventional FD-OCM image shown in Figure 6.7(b) acquired using the same probe.

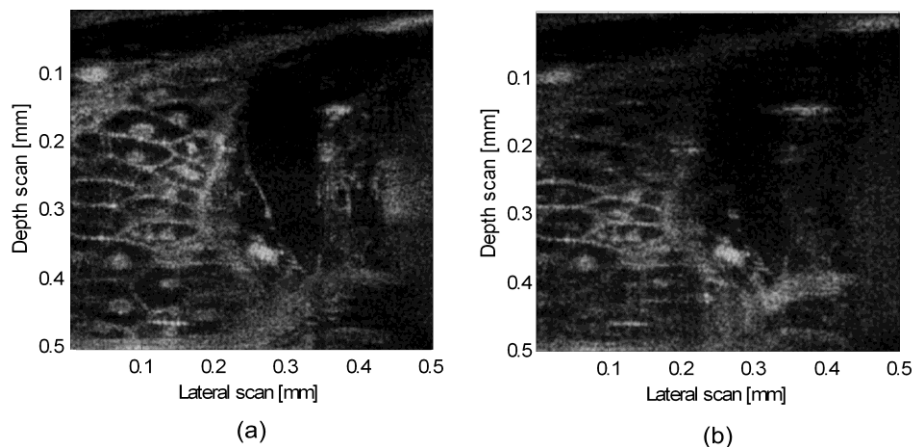


Figure 6.7: (a) Sub-cellular resolution cross-sectional imaging of an African frog tadpole acquired by GD-OCM (b) in comparison, an image acquired by FD-OCM with the same custom objective.

To validate high resolution capability across the full-field of view of the probe, the 2 mm lateral dimension sampled at 1  $\mu\text{m}$  interval of fat cells of an *ex vivo* human tissue obtained from breast reduction surgery was acquired using the same GD-OCM setup. The fused image was reconstructed from six refocus steps with a focal shifted distance of about 60  $\mu\text{m}$  per step covering approximately 500  $\mu\text{m}$  imaging depth range in high resolution as shown in Figure 6.8.

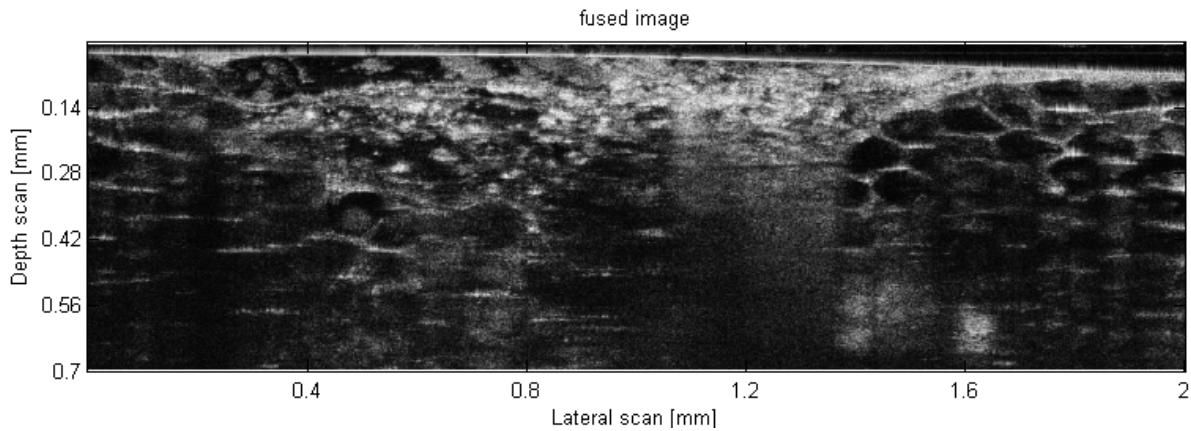


Figure 6.8: GD-OCM imaging of fat cells of an *ex vivo* human skin sample covering a 2 mm lateral field of view

Finally, *in vivo* imaging of human skin is shown in Figure 6.9. The top image was taken around the nail fold region of the little finger, and the bottom one was taken from the area around the finger joint. The boundary between dermis and epidermis regions is clearly observed in both images. The features indicated by arrows are believed to be blood vessel network that typically locates in the dermis region.

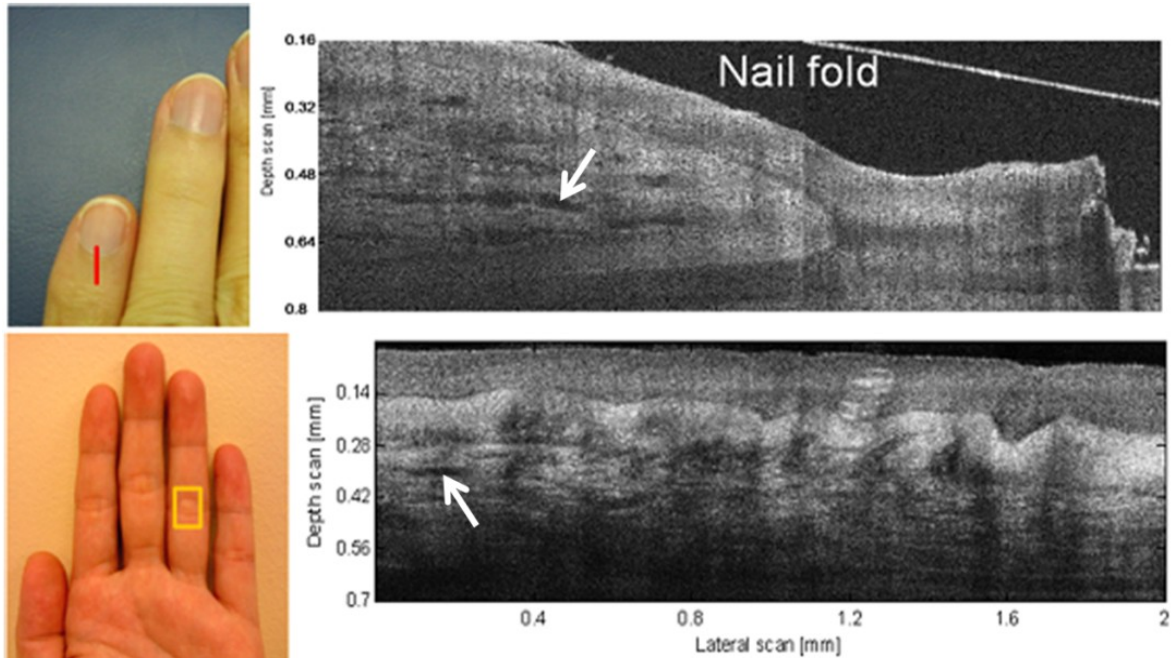


Figure 6.9: *In vivo* GD-OCM images of human skin taken from a nail fold (top) and a finger joint (bottom)

#### 6.4 Volumetric Imaging with GD-OCM

In this section, the fusing technique used in GD-OCM is demonstrated to be easily extended to 3D imaging when accommodated with a high speed spectrometer. For volumetric imaging, at each focus position, a 3D dataset is acquired, and then the focus is shifted to the next position and so on. This approach to scanning minimizes the number of the focal shift operation of the probe and hence the response time of the probe can be neglected. In addition, by shifting the focal plane per volume, the filtering window can be calculated from a single frame and then applied to the whole volume since the focus position can be approximately the same for each acquired volume. The acquired data is first stored in a computer's hard drive. The data

processing starts once all 3D datasets are collected. The post processing of the data consists of DC subtraction, linear frequency domain calibration, fast Fourier transform, fusing, and volumetric rendering.

Using the system detailed in section 6.2, a 3D dataset consisting of 1000 x 500 spectra covering the field of view of 2 mm x 1 mm was acquired at each refocusing step. Four 3D datasets were acquired with focal shift interval of about 100  $\mu\text{m}$  capable of providing an invariant lateral resolution over 400  $\mu\text{m}$  in depth. The fusing process was implemented in Labview software with a total fusing time of about 30 minutes. The fusing was performed in a frame by frame basis. The fused dataset consisted of 500 fused frames of 1000 x 600 pixels per frame. A full size 3D image of a skin fat is shown in Figure 6.10, where fat cells are clearly distinguished as well as connective tissues on the top. In addition, 3D images of the skin fat captured at different orientations are displayed in Figure 6.11.

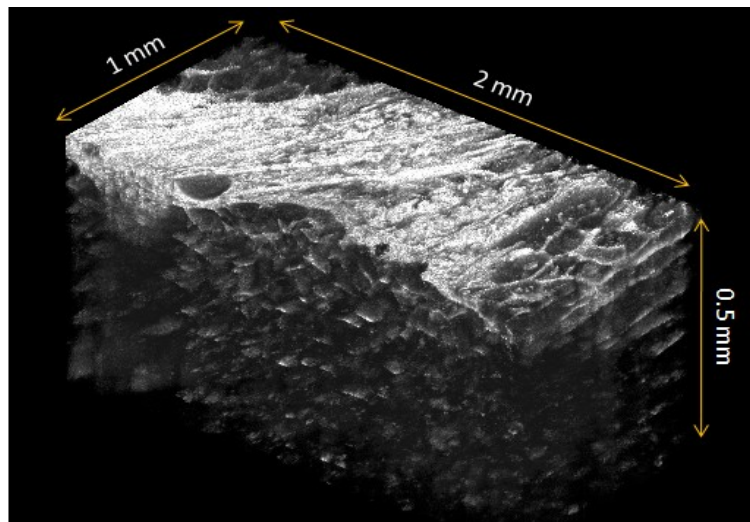


Figure 6.10: A volumetric image of the fat cells of an *ex vivo* skin acquired by GD-OCM

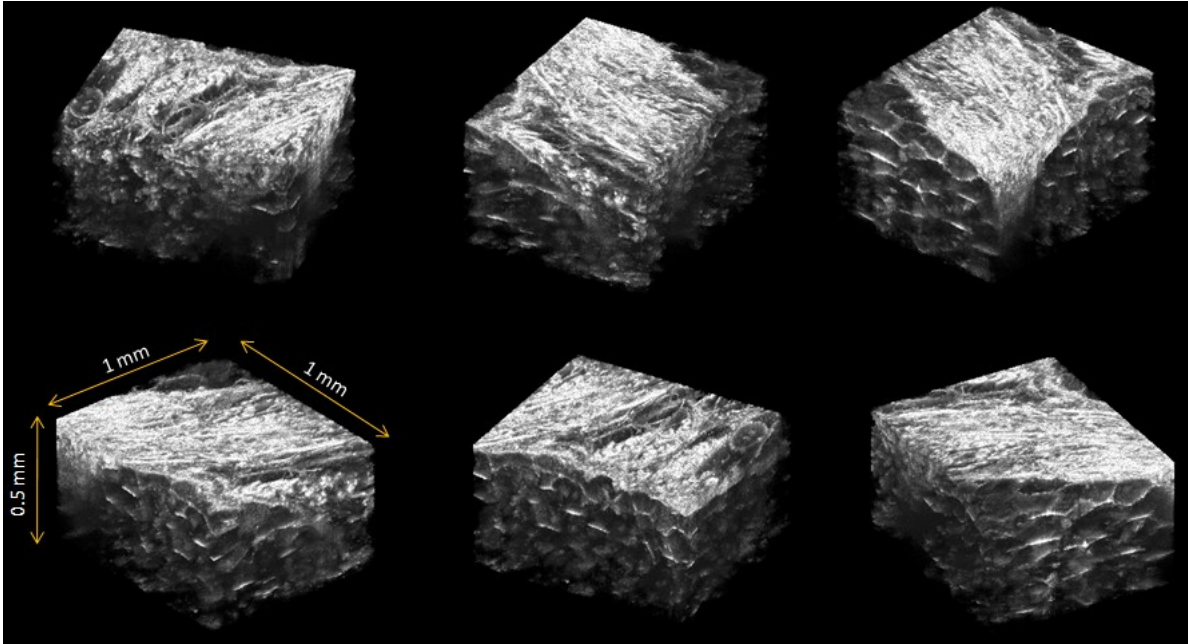


Figure 6.11: A cut portion of the 3D data displayed in various angles

Furthermore, by using a high speed CMOS camera (spL8192-70km, Basler Vision Technologies) embedded in a custom designed spectrometer as a detector, the feasibility of *in vivo* volumetric GD-OCM was investigated. A volumetric imaging of *in vivo* human skin was performed. Each volumetric dataset, consisting of 200 A-lines per frame and 150 frames per volume, was acquired at imaging speed of 40 frames per second. Three datasets were acquired at about 100  $\mu\text{m}$  focal shift interval. Each volumetric dataset was Fourier transformed and then fused together using the method in section 6.3. The volumetric rendering of the fused data is displayed in Figure 6.12(a). Furthermore, multiple *en face* images were extracted from the fused dataset for every 20  $\mu\text{m}$  along the axial direction as shown in Figure 6.12(b). Cells can be observed at the dermis region as designated by the red dash box.

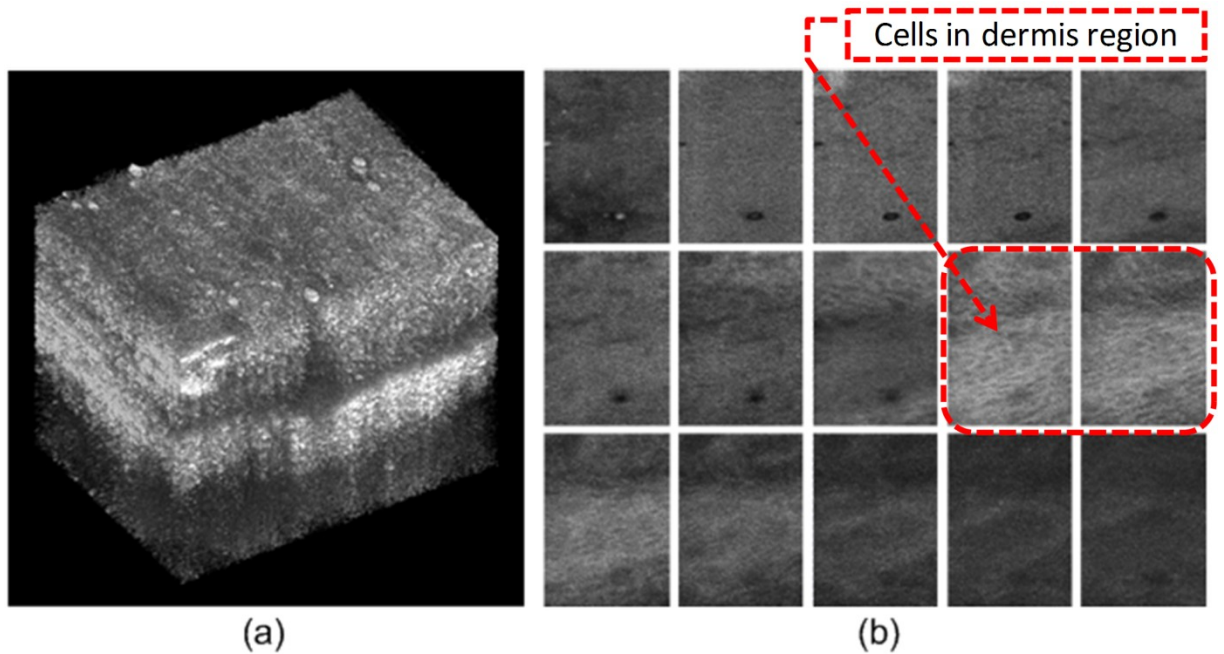


Figure 6.12: (a) volumetric rendering of *in vivo* human finger skin acquired by high speed GD-OCM; (b) *En face* images extracted from every 20  $\mu\text{m}$  along the axial direction of the fused 3D dataset.

## 6.5 Summary

GD-OCM is a developing imaging technology that builds on the high speed imaging capability of FD-OCT, the high lateral resolution of OCM, and the ability of real-time refocusing of the dynamic focusing microscope objective. GD-OCM is capable of high lateral resolution images (2-3  $\mu\text{m}$ ) throughout the imaging depth of up to 2 mm. The combination of FD-OCM and the dynamic focusing technique, however, requires an acquisition scheme similar to the C-Mode acquisition in ultrasonography, which yields multiple images contained in-focus details at different depth as the output. Therefore, a method of extracting and fusing these details together



to form a final image that contains only in-focus information is required. Moreover, driven by the capability of the technique to acquire images at high speed, a real time fusing algorithm is demanded.

This dissertation detailed the mathematical description of GD-OCM; including the effect of high NA optics to the FD-OCM signal, the mathematical model of dynamic focusing, and the reconstruction of the full depth profile. Consequently, a fusion method was developed based on the concept of the inverse local Fourier transform and the Gabor's signal expansion. The developed fusion algorithm is capable of automatic reconstruction of the full depth image in real time. The Gabor-fused image provides a final image that is high resolution and invariant over the cross-section area. The technique requires no human intervention and adaptively determines the width and position of the window for each fused image. Moreover, the fusion process involves only summation and multiplication, and is therefore fast.

Finally, several examples of cellular level imaging of biological samples were presented; such as *ex vivo* African frog tadpole, *ex vivo* skin fat, and *in vivo* human nail fold. Furthermore, the feasibility of high resolution volumetric imaging using GD-OCM was also investigated. The proposed technology is capable of high-resolution volumetric imaging and has the potential to impact many other areas of surgery and diagnostic applications.

## **CHAPTER SEVEN: OPTICAL DESIGN OF DYNAMIC FOCUS CATHETER FOR ENDOSCOPIC GD-OCM**

This chapter presents the optical design of a circumferential scanning probe for endoscopic GD-OCM. The aberration induced by a cylindrical exit window needed to protect the catheter as well as a solution to minimize this effect is discussed. Moreover, the by-design performances of the catheter are presented. The catheter is capable of remotely controlling the focus position in real time while maintaining a good image quality throughout the depth penetration range.

### **7.1 Optical Design of a Dynamic Focus Catheter**

The catheter was designed to be used with a Titanium:Sapphire (Ti:Sa) laser source with a FWHM spectral width of 120 nm centered at 800 nm, corresponding to approximately 2.5  $\mu\text{m}$  axial resolution in air. A circumferential imaging probe was designed by using a 2 mm fold mirror attached with a 1.9 mm micromotor at the distal end in order to rotate the beam 360 degree (Herz et al. 2004; Tran et al. 2004). To advance the technology an order of magnitude in resolution in comparison to commercial devices, the catheter was designed to have a NA of approximately 0.1 that corresponds to less than 10  $\mu\text{m}$  lateral resolution throughout the working depth range. Furthermore, the optics was designed to reach the diffraction limit. A factor that significantly limits the image quality and resolution is a cylindrical transparent exit window, which causes astigmatism that increases as a function of the window thickness and the distance from the window to the focus position. To remedy this problem, the design utilizes a micro

cylindrical lens after the fold mirror to compensate for astigmatism caused by this cylindrical window.

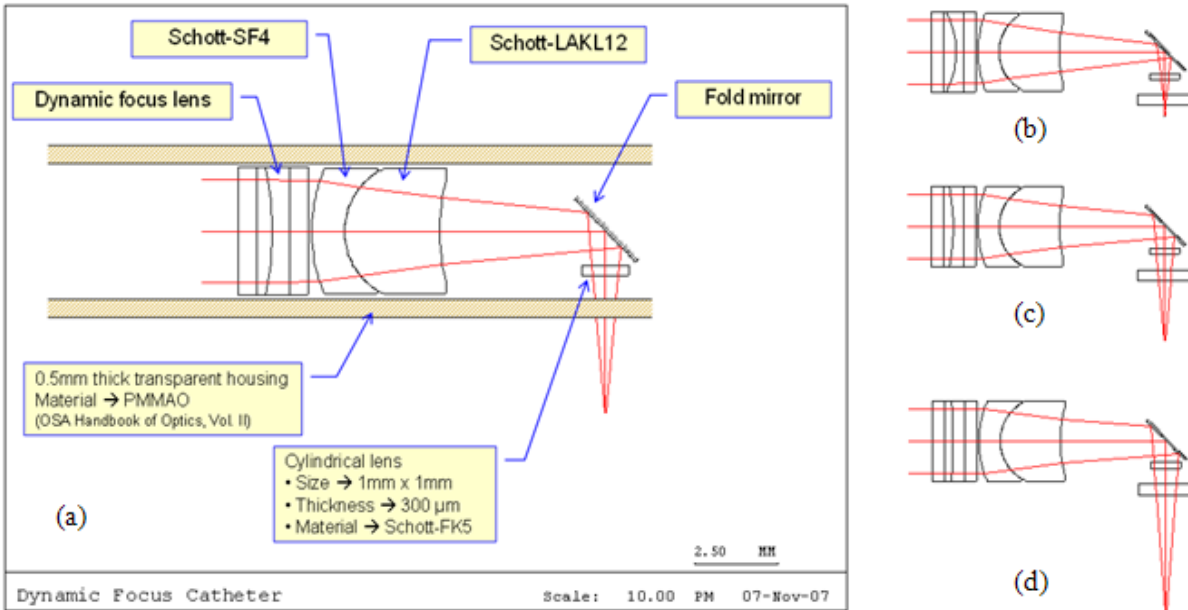


Figure 7.1: The catheter design layout

Figure 7.1(a) and Table 7-1 show the optical layout and specification of the designed dynamic focus catheter, respectively. The first element is a liquid lens (ARCTIC 320, Varioptic) that is capable of changing its focal length from 44 mm to 1 m according to an applied voltage (i.e., up to 60 volts) within 20-80 milliseconds as shown in Figure 7.2 (Lee et al. 2010b). The variable focal length allows overcoming a limitation on depth of focus (DOF) that dramatically decreases as NA increase (i.e.  $DOF \propto 1/NA^2$ ). Figure 7.1(b-d) shows the catheter's layout at three different focus positions. Also, for small optics of less than 1 mm in diameter as needed for endoscopy, the liquid lens may be replaced by a custom design liquid crystal lens that can operate at significant higher speeds for this small size (Murali et al. 2007). For liquid crystal lens technology, the smaller the diameter of the lens, the faster. However, one needs to be concerned

about polarization properties when designing an optical system incorporating a liquid crystal lens.

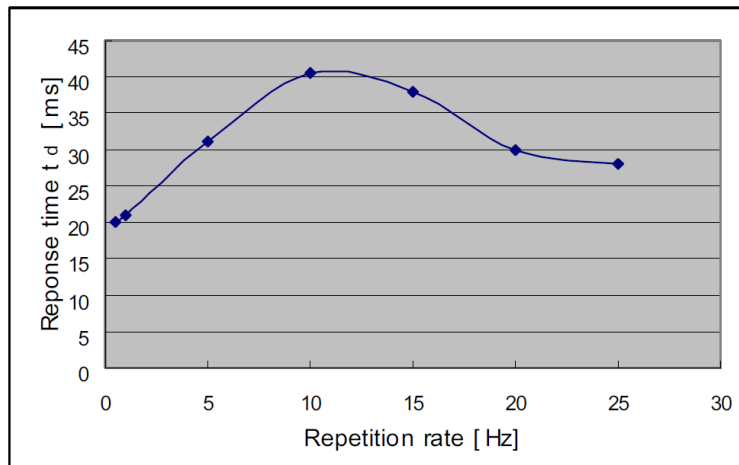


Figure 7.2: Response times of the liquid lens at different repetition rates (Lee et al. 2010b).

Table 7-1 Design specification

<b>Fixed parameters</b>					
Source	Titanium:Sapphire Laser: 800nm center wavelength, 120nm FWHM				
Field of view	On axis with 360 degree circumferential scan				
Entrance pupil diameter	3mm				
Physical length	12mm (excluding collimator and micromotor)				
Overall diameter	5mm				
Estimated % transmission	> 85% , Based on 94% transmission of the liquid lens, 99% transmission of the doublet and the cylindrical lens, 95% transmission of the mirror, and 98% transmission of the housing window.				
<b>Dynamic parameters</b>					
Working distance*	0.5 mm	1.5 mm	3.0 mm	4.5 mm	5.5 mm
Numerical aperture	0.12	0.11	0.10	0.09	0.08
Diffraction limited res.**	4.07 $\mu\text{m}$	4.44 $\mu\text{m}$	4.88 $\mu\text{m}$	5.42 $\mu\text{m}$	6.10 $\mu\text{m}$

\* The distance from outer surface to the imaging plane

\*\* Based-on the Rayleigh criterion

A doublet as a combination of SF4 and LAKL12 from the Schott catalog, as an example, was added between the liquid lens and the reflector in order to shorten the catheter length. This configuration led to a high NA and the use of a doublet minimized the axial chromatic aberration throughout the working distance as shown in Figure 7.3. The overall ray aberration is shown however to be optimum at a  $\sim 1.5$  mm working distance. In addition, a miniature 1 mm x 1 mm cylindrical lens (Schott FK5) that is 300  $\mu\text{m}$  thick was added after the fold mirror to pre-compensate the astigmatism caused by the cylindrical window. This lens is attached and rotated together with the fold mirror.

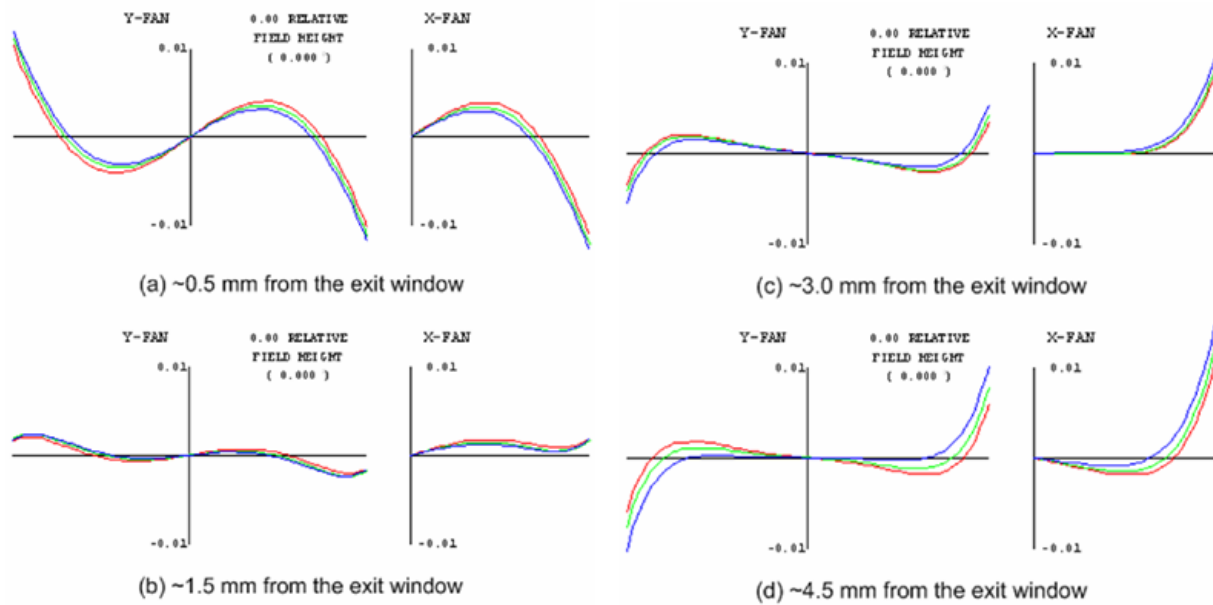


Figure 7.3: The ray aberration curves at arbitrary focus (a-d) plotted within  $\pm 10$   $\mu\text{m}$  maximum scale. The chromatic aberration was optimized at the working distances of 0.5, 1.5 and 3 mm; a slight degradation is observed at a distance of  $\sim 4.5$  mm from the exit window

The housing material was chosen to be a polymethylmethacrylate (PMMA), which is transparent in the wavelength range from ultraviolet (UV) to near infrared (NIR), easy to fabricate into a product with various shapes, of reasonable cost, and biologically compatible (Lee et al. 1995). In this design, we used PMMA that is transparent in the wavelength region ~365 nm to 1014 nm with a ~1.492 refractive index (Lytle 1995). The transparent housing allows fully 360 degree field of view in lateral scanning. The catheter was designed, optimized, and analyzed using CODE V™ software (Optical Research Associates, California). The clear aperture diameter of the liquid lens was 3 mm, and the catheter was designed to have an overall diameter equal to 5 mm, as currently limited by the size of the liquid lens.

## **7.2 Effects of the Cylindrical Exit Window**

Without the cylindrically shaped exit window, the lateral resolution as verified by a two point source separation analysis was almost diffraction limited throughout the working range. When accounting for the exit window, the lateral point spread function (PSF) was severely degraded by astigmatism, particularly at the maximum depth scanning of 5 mm, as shown in Figure 7.4(a). The aberration caused by the exit window not only degraded the lateral resolution but also reduced the Strehl ratio (SR) leading to a decrease in system sensitivity when the sample was far away from the exit window. The challenge was how to optimize for this astigmatism throughout the working range while performing the dynamic scan of the imaging plane. Doing so by further minimizing the window thickness was not practically feasible. As shown in Figure 7.4(a), the PSF was rapidly degraded even with a 50  $\mu\text{m}$  thick window. In this design, a cylindrical

microlens was added right after the fold mirror in order to compensate the effect of the cylindrical window. The PSF after compensation was dramatically improved as shown in Figure 7.4(b) and led to invariant resolution throughout the 5 mm working range. The attachment of the microlens to the rotating mirror enables the  $\sim 360$  degree scan.

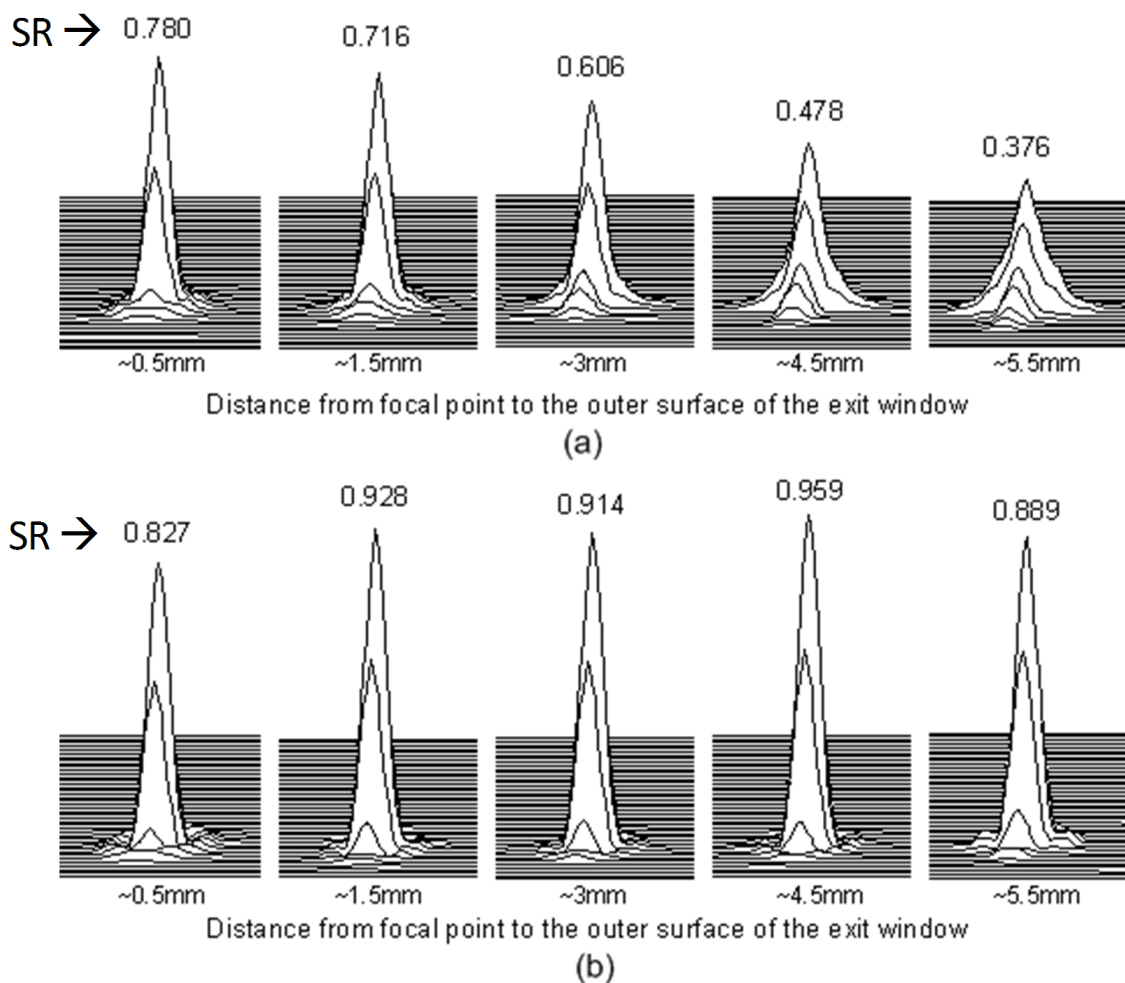


Figure 7.4: Lateral point spread function (PSF) and Strehl ratio (SR) throughout the working range (a) without the cylindrical microlens and using an already ultrathin 50 microns window thickness, and (b) with a cylindrical microlens and a 500 microns window thickness.

### 7.3 As Designed Performance

The lateral resolution of the system was assessed at each focal plane throughout the working range starting from 0.5 mm from the last surface of the system, which is the outer surface of the probe, to 5.5 mm from that surface yielding approximately 5 mm working range as shown in Table 7-2. Using the two-point source analysis in Code V, the system is shown to resolve approximately 4  $\mu\text{m}$  separation at the close focal plane and 6  $\mu\text{m}$  separation at the far focal plane. Furthermore, the modulation transfer functions (MTFs) and SRs are diffraction limited (i.e.  $\text{SR} \geq 0.8$ ).

Table 7-2 Dynamic focusing performance throughout the working range i.e. lateral resolution as determined by convolution of two PSFs, averaged MTF at 100 cycles/mm, and SR at best focus.

	<b>Imaging distance as measured from the exit window to the focal plane</b>				
	~ 0.5 mm	~ 1.5 mm	~ 3.0 mm	~ 4.5 mm	~ 5.5 mm
<b>Resolution</b>	~ 4.2 $\mu\text{m}$	~ 4.5 $\mu\text{m}$	~ 5.0 $\mu\text{m}$	~ 5.5 $\mu\text{m}$	~ 6.0 $\mu\text{m}$
<b>MTF</b>	~ 43 %	~ 50 %	~ 45 %	~ 40 %	~ 35 %
<b>SR</b>	0.827	0.928	0.914	0.959	0.889

### 7.4 Fabrication and Assembly Tolerances

In addition, the fabrication and assembly tolerances together with compensations were analyzed using the precision quality from OPTIMAX (Optimax Systems, Inc.) as tolerance limits as shown in Table 7-3. When operating at proximal focus (0.5 mm from the exit window), the probable drop in MTF is less than 11 % measured at 100 cycles/mm with the compensator range,



the probable displacement of the imaging plane, which is estimated to be around  $\pm 0.2$  mm. At the distal focus (5.5 mm from the exit window), the probable drop in MTF is 12 % at 100 cycles/mm with a probable change of the imaging plane of approximately  $\pm 0.3$  mm. The drop of MTF is less than 15% and meets the as-built specification in both cases. The slight shift in the image plane can be calibrated once the probe is built. By further tightening the tolerances assembly, such shift could also be further minimized at the expense of increased fabrication cost.

Table 7-3 Fabrication and assembly tolerance analysis

	Imaging distance as measured from the exit window to the focal plane				
	0.5 mm	1.5 mm	3.0 mm	4.5 mm	5.5 mm
Probable MTF drop (%)	11	10	12	13	12
Probable shift of focus (mm)	0.21	0.23	0.25	0.29	0.3

## 7.5 Summary

In summary, a high lateral resolution and long working range dynamic focusing catheter without mechanical refocusing for an endoscopic GD-OCM was designed by embedding a dynamic focusing liquid lens. The doublet was used to minimize the axial chromatic aberration as well as to reduce the overall focal length of the system and hence the probe's length was 12 mm from the first surface of the liquid lens to the fold mirror (Figure 7.1). The image quality of the system at the far focal plane was severely affected by the transparent cylindrical window needed to protect the catheter when acquiring the image inside the human body. This aberration can be compensated by adding a cylindrical microlens, which can correct astigmatism caused by

the window regardless of its thickness. With this design, diffraction limit resolution was achieved over a 5 mm imaging distance. The lateral resolution is less than 6  $\mu\text{m}$  with more than 0.8 SR over the 5 mm scanning range (i.e.  $\sim 4 \mu\text{m}$  with 0.84 SR at proximal focus and  $\sim 6 \mu\text{m}$  with a 0.9 SR at distal focus).

In clinical imaging situations, the sample size can be varied based on applications; for example, the different sizes between an artery and a GI track and the local size of the sample at different location of interest. In addition, the sample sizes can be varied among different patients. Combining a dynamic focus probe with a high speed OCT (i.e. video rate) enables imaging at invariant high lateral resolution as the sample size is naturally varying. Furthermore, the ability to dynamically change the focus does not only help maintain high lateral resolution but also improve the system sensitivity as demonstrated by many prior works (Herz et al. 2004; Murali et al. 2007).

## CHAPTER EIGHT: SUMMARY AND FUTURE DIRECTION

### 8.1 Summary

Since it started in 1991, OCT has been introduced for almost 20 years. Providing non-invasive *in vivo* optical depth sectioning in the micrometer regime resolution, OCT has been proven to be a useful tool for medical imaging, filling the gap between ultrasonography and optical microscopy. The imaging contrast of conventional OCT relies on the natural refractive index fluctuation within biological samples. The variation of refractive index leads to variations in the strength of backscattering signals as a function of depth. As a result, a depth-resolved reflectivity profile can be measured by either scanning the reference arm of a low coherence interferometer in the case of TD-OCT, or Fourier Transformation of the spectral interference signal in FD-OCT. Nevertheless, conventional measurements only provide details about sample structures. For many years, scientists have investigated extended OCT system that can measure not only the object structure but also its functional information, such as birefringence, flow, and elastic properties.

This dissertation has developed one such functional OCT imaging so-called Phase-Resolved Doppler OCT or PR-DOCT. The detectable velocity dynamic range of PR-DOCT was limited by the system phase stability at the lower boundary and the  $\pi$  phase ambiguity at the upper limit. Application of DOCT for flow imaging is an increasing area of interest. This is mainly due to the rapid technological advancements in imaging speed. The improvement in acquisition speed of FD-OCT accommodated by a high speed CMOS camera allows PR-DOCT

to monitor high axial flow speed of up to 45 mm/s (Schmoll et al. 2009). However, this capability comes with the cost of an increase in the minimum detectable velocity that could lead to invisibility of the slow flow activity whose axial speed is below the minimum detectable threshold of the system. At a camera line rate of 200 kHz, the minimum detectable axial velocity was 0.46 mm/s. This is about 60 times higher than the smallest minimum detectable velocity of 7.4  $\mu\text{m/s}$  previously reported by White et al. (White et al. 2003). In this system, the maximum detectable axial velocity was limited to 4.5 mm/s, yielding a ratio between the maximum and minimum detectable velocity of about 600.

In this dissertation, an alternative acquisition scheme for swept-source based PR-DOCT was presented. The technique acquires multiple Doppler images having different detectable velocity ranges in a single measurement and hence extends the overall detectable velocity dynamic range of the system. Specifically, the technique extends the lower limit of the velocity dynamic range, while maintaining the maximum detectable velocity of a given PR-DOCT system. The developed system exhibits high phase stability. A FWHM of histogram distribution of the measured Doppler phase shift error is about 13 mrad that corresponds to the minimum detectable axial velocity of 11.3  $\mu\text{m/s}$  as discussed in section 3.4. It should be pointed out that, most of the reported minimum detectable velocity of PR-DOCT in the literature was quantified from the standard deviation of the measured Doppler phase shift error of the system. In this system, the standard deviation of the measured Doppler phase shift error is computed to be 5.5 mrad, yielding the minimum detectable axial velocity of about 5  $\mu\text{m/s}$ . The maximum detectable axial velocity of the system is 11 mm/s, yielding a ratio between the maximum and

minimum detectable velocity of about 2200. The technique extends detectable velocity dynamic range of PR-DOCT by at least five times of that typically achieved in a conventional method. In addition, the technique involves small amount of processed data as discussed in section 3.5 and therefore is capable of real time monitoring of wide velocity dynamic range of the flow activity in biological samples.

A limitation in flow imaging in practical applications, such as studying microvasculature and embryonic heart development, is the imaging depth. Even though, the high speed imaging capability of FD-OCT is attractive for real time *in vivo* monitoring of flow activity in biological samples as well as flow segmentation in 3D, the main challenges in conventional FD-OCT are the existence of the mirror image and the limited spectral resolution of the detected spectral interference signal. These two issues motivate a quest to remove the mirror image in FD-OCT in order to double the imaging depth range as well as efficiently utilize the maximum sensitivity out of a FD-OCT system. This dissertation addressed these issues in a novel method called Dual-Detection Full-Range FD-OCT or DD-FD-OCT. The DD-FD-OCT simultaneously detects two spectral interferences that have a  $\pi/2$  phase relation representing real and imaginary components of the complex spectral interference signal (Lee et al. 2010a). As a result, it is capable of retrieval of the full-range depth profile without loss in acquisition speed as compared to conventional FD-OCT and it is insensitive to sample motion.

One main advantage of DD-FD-OCT over other full-range techniques is that the full-range signal is achieved without manipulation of the phase relation between consecutive axial lines. Hence the full-range DD-FD-OCT is fully applicable to PR-DOCT without reduction in

either detectable velocity dynamic range or mirror image rejection performances as detailed in chapter five. Moreover, by combining the full-range capability with phase-resolved Doppler imaging, the flow region can be placed close to the zero-delay position and the highest SNR around this region can be utilized to improve flow visibility and sensitivity in biological samples.

Another important factor necessary for medical diagnostic applications using OCT is resolution. Conventional OCT utilized low NA ( $< 0.1$ ) imaging optics to cover an imaging depth range of about 2 to 3 mm governed by the depth penetration limit of OCT. Using such low NA limits the lateral resolution of OCT to about 20 to 30  $\mu\text{m}$ . OCM achieves high lateral resolution in order of a few microns at the expense of the shorter depth of focus. Consequently, OCM is subject to short imaging depth range of less than 100  $\mu\text{m}$ . Recently, GD-OCM, a novel technique for high lateral resolution imaging over an extended imaging depth range covering the whole depth penetration range, has been reported (Rolland et al. 2008). GD-OCM embeds a liquid lens within a custom designed microscope objective that allows acquisition of multiple images at different focus position in real time (Murali 2009). Such acquisition scheme, however, requires a method that efficiently extracts and then fuses together in-focus portions from acquired images.

This dissertation detailed the technique to automatically and adaptively fuse those acquired images together to form a final image that contains mainly in-focus information throughout the entire imaging depth range (Rolland et al. 2010a). The technique provides a smooth fusing result without the need of human intervention, which is important to transfer this technology to the clinic. Furthermore, cellular level images of an *ex vivo* African frog tadpole as well as *ex vivo* skin fat tissues using the GD-OCM were presented. Moreover, using a recently

developed high speed spectrometer built on a high speed CMOS camera that is capable of 70,000 axial scan per second, an *in vivo* imaging of human skin was demonstrated revealing cells in the dermis region. Such high acquisition rate motivates the need of an automatic fusion algorithm in order to do real time display with GD-OCM.

In addition, this dissertation investigated an optical design of a dynamic focus catheter for endoscopic imaging with GD-OCM (Meemon et al. 2008a). Endoscopy is a useful tool for imaging within tubular organs inside the human body, such as the vascular system, the lung, the gastrointestinal tract, the breast duct, and the urinary tract. The dynamic focus capability is based on a liquid lens technology that provides variable focus by changing its curvatures in response to an electric field variation. In this design, a liquid lens was embedded in the optical design of a circumferential scanning endoscopic probe providing a capability of remotely controlling the focus position in real time while maintaining a good image quality throughout the depth penetration range. Furthermore, the effects of a cylindrical exit window, which is presented in practice to shield the catheter, were accounted for and the degradation in image quality caused by such window was corrected to yield diffraction limited imaging performance. As a result, a dynamically focusing catheter with a lateral resolution of less than 6  $\mu\text{m}$  through a  $\sim 5$  mm imaging distance was achieved by design without mechanically re-focusing the system.

## **8.2 Future Directions**

As part of future work, the implementation of a phase-resolved Doppler imaging in GD-OCM technology will be investigated. The combination is promising for high resolution Doppler

imaging that will allow resolving small vessels in biological samples. However, for real time monitoring of the flow activity, the processing speed of the GD-OCM needs to be improved. One viable solution is by utilizing the power of parallel processing capability of a graphic processing unit (GPU).

Moreover, one potential application of Doppler imaging, besides flow monitoring, is displacement tracking because any axial movement will cause a Doppler phase shift in the detected interference signal. The displacement information can be used to compute a strain profile as a function of depth that can be related to the elastic property of the tissue. It is commonly known that most pathological changes are associated with changes in tissue stiffness. Therefore, the use of the elastic properties of tissues such as hardness or stiffness as an indicator of abnormal pathological tissues is known. For centuries, physicians have relied on palpation technique in order to detect the hard areas of tissues that are usually correlated to tumor regions such as breast tumors. For many years, several groups of scientists have reported the quantification of tissue elasticity. For example, Parker et al. reported the *in vitro* measurement of the elastic moduli of a set of tissue phantoms and prostate tissues using a triple beam balance setup (Parker et al. 1990). Moreover, Sarvazyan et al. presented the study of shear acoustic properties of 162 *in vitro* biological samples of normal and cancerous tissues. The result indicated that normal breast tissue is approximately four times softer than fibroadenomatous breast tissue (benign tumor), and the range of shear moduli of breast cancer is approximately seven times higher than those of normal tissue (Sarvazyan 1993). In addition, Walz et al. reported an *in vivo* study of 250 breast lesions. The result indicated that fibroadenomas are



approximately eight times softer than carcinomas (a malignant cancer that arises from epithelial cells) (Walz et al. 1993). All of these works were focused on the global elastic properties of the samples in order to study the difference in elastic properties between normal and cancerous tissues. Nevertheless, for diagnostic purposes, the localization of the stiffness is demanded.

A method of quantifying the local stiffness or elastic properties of tissues through a non-invasive imaging technique is known as *Elastography* (Ophir et al. 1991). Elastography had been under development in ultrasonography for more than 15 years. The basic idea of Elastographic imaging is to image the displacements of individual tissue elements as they are stretched, compressed, or vibrated. When mechanical compression or vibration is applied, the tumor deforms less than surrounding tissue, hence its strain is less than the surrounding tissue. (Ophir et al. 1991; Parker et al. 1996). Various techniques of elastography have been developed using different excitation forces, different detection schemes, and by extracting different elastic properties of the tissue.

Schmitt first introduced and demonstrated OCT elastography (OCE) in 1998 (Schmitt 1998). Combined with the high resolution capability of OCT, OCE is believed to be capable of quantifying local displacement as small as a few micrometers at a depth of up to 2 mm below the surface of optical dense tissue. Therefore, the minimum resolvable displacement is at least an order of magnitude below that measured with the highest frequency ultrasonic transducers used routinely in clinical practice, and exceeds the minimum displacement that has been measured by MRI by an even larger magnitude. Conventional OCT elastography utilized the technique of speckle tracking invented in ultrasound elastography. The technique measured a local

displacement from two OCT images acquired before and after compression. However, the speckle tracking method involved local cross-correlation and hence required a massive amount of computational time.

Displacement tracking using a Doppler technique is more interesting due to its real time processing capability. The measure of tissue elasticity through Doppler imaging was first introduced by Lerner et al. around 1988. It is a tissue elasticity imaging technique based on the estimation of the amplitude response of the tissues under harmonic mechanical excitation so called *vibrational sonoelastography* (Lerner et al. 1988). In this method, a low frequency mechanical vibration (20-1000 Hz) is externally applied to a sample introducing internal vibration patterns inside the sample. The vibration pattern is then detected by color Doppler imaging in real time. The hypothesis is that stiff tissues will respond to an applied mechanical vibration differently than normal soft tissues (Parker et al. 1996).

Recently, a vibrational amplitude elastography using OCT was investigated by Wang et al. (Wang et al. 2006). The results verified the feasibility of OCT Doppler imaging for real time mapping of a strain profile within a soft tissue. Nevertheless, several issues —such as a method of *in vivo* excitation, an excitation magnitude, the sensitivity of the method, and an ability to differentiate normal, benign, and pathological tissues— have to be investigated in order to bring the technique to clinical use. In addition, the potential application of OCT elastography is to differentiate between hard pathological and soft normal skin tissues, particularly in the early stage. Therefore, high resolution imaging beyond that of conventional OCT is desirable. For this purpose, the implementation of GD-OCM to elastography is of interest.

## LIST OF REFERENCES

- Abramowitz, M., K. R. Spring, B. O. Flynn, J. C. Long, M. Parry-Hill, K. I. Tchourioukanov, and M. W. Davidson, "Basic Concepts in Optical Microscopy." from <http://www.olympusmicro.com/primer/anatomy/anatomy.html> (2009).
- Aguirre, A., N. Nishizawa, J. Fujimoto, W. Seitz, M. Lederer, and D. Kopf, "Continuum generation in a novel photonic crystal fiber for ultrahigh resolution optical coherence tomography at 800 nm and 1300 nm," *Optics Express* **14**(3), 1145-1160 (2006).
- Aguirre, A. D., P. Hsiung, T. H. Ko, I. Hartl, and J. G. Fujimoto, "High-resolution optical coherence microscopy for high-speed, in vivo cellular imaging," *Optics letters* **28**(21), 2064-2066 (2003).
- Akcaay, A. C., E. Clarkson, and J. P. Rolland, "Effect of source spectral shape on task-based assessment of detection and resolution in optical coherence tomography," *Applied optics* **44**(35), 7573-7580 (2005).
- An, L. and R. K. Wang, "Use of a scanner to modulate spatial interferograms for in vivo full-range Fourier-domain optical coherence tomography," *Optics letters* **32**(23), 3423-3425 (2007).
- An, L. and R. K. Wang, "In vivo volumetric imaging of vascular perfusion within human retina and choroids with optical micro-angiography," *Opt. Express* **16**, 11438-11452 (2008).
- An, L., J. Qin, and R. K. Wang, "Ultrahigh sensitive optical microangiography for in vivo imaging of microcirculations within human skin tissue beds," *Optics Express* **18**(8), 8220-8228 (2010).
- Bachmann, A. H., M. L. Villiger, C. Blatter, T. Lasser, and R. A. Leitgeb, "Resonant Doppler flow imaging and optical vivisection of retinal blood vessels," *Optics Express* **15**(2), 408-422 (2007).
- Barrett, H. H. and K. Myers, *Foundations of image science*. Hoboken, NJ: John Wiley & Sons (2004).
- Baumann, B., M. Pircher, E. Göttinger, and C. K. Hitzenberger, "Full range complex spectral domain optical coherence tomography without additional phase shifters," *Optics Express* **15**(20), 13375-13387 (2007).
- Beyer, W. H., *CRC standard mathematical tables and formulae*, CRC press Boca Raton (1991).
- Born, M. and E. Wolf, *Principles of Optics, seventh expanded edition*, Cambridge University Press (1999).
- Bouma, B., G. J. Tearney, S. A. Boppart, M. R. Hee, M. E. Brezinski, and J. G. Fujimoto, "High-resolution optical coherence tomographic imaging using a mode-locked Ti: Al<sub>2</sub>O<sub>3</sub> laser source," *Optics Letters* **20**(13), 1486-1488 (1995).
- Bouma, B. E. and G. J. Tearney, *Handbook of optical coherence tomography*, Marcel Dekker, Inc. (2002).
- Broadly, A. S. and C. A. Gooding, "Magnetic Resonance Imaging," *Pediatrics in Review* **8**, 87-92 (1986).

- Bruning, J. H., D. R. Herriott, J. E. Gallagher, D. P. Rosenfeld, A. D. White, and D. J. Brangaccio, "Digital wavefront measuring interferometer for testing optical surfaces and lenses," *Appl. Opt* **13**, 2693-2703 (1974).
- Carré, P., "Installation et utilisation du comparateur photométrique et interférentiel du Bureau International des Poids et Mesures," *Metrologia* **2**, 13 (1966).
- Cense, B., N. Nassif, T. Chen, M. Pierce, S. H. Yun, B. Park, B. Bouma, G. Tearney, and J. de Boer, "Ultrahigh-resolution high-speed retinal imaging using spectral-domain optical coherence tomography," *Optics Express* **12**(11), 2435-2447 (2004).
- Chen, Z., T. E. Milner, D. Dave, and J. S. Nelson, "Optical Doppler tomographic imaging of fluid flow velocity in highly scattering media," *Optics Letters* **22**(1), 64-66 (1997).
- Chinn, S. R., E. A. Swanson, and J. G. Fujimoto, "Optical coherence tomography using a frequency-tunable optical source," *Optics Letters* **22**(5), 340-342 (1997).
- Choma, M., M. Sarunic, C. Yang, and J. Izatt, "Sensitivity advantage of swept source and Fourier domain optical coherence tomography," *Optics Express* **11**(18), 2183-2189 (2003).
- Choma, M. A., C. Yang, and J. A. Izatt, "Instantaneous quadrature low-coherence interferometry with 3x3 fiber-optic couplers," *Optics letters* **28**(22), 2162-2164 (2003).
- Cimalla, P., J. Walther, M. Mehner, M. Cuevas, and E. Koch, "Simultaneous dual-band optical coherence tomography in the spectral domain for high resolution in vivo imaging," *Opt. Express* **17**, 19486-19500 (2009).
- Cobb, M. J., X. Liu, and X. Li, "Continuous focus tracking for real-time optical coherence tomography," *Optics Letters* **30**(13), 1680-1682 (2005).
- Dave, D. P. and T. E. Milner, "Doppler-angle measurement in highly scattering media," *Optics letters* **25**, 1523-1525 (2000).
- Davidson, M., K. Kaufman, I. Mazor, and F. Cohen, "An application of interference microscopy to integrated circuit inspection and metrology." *Integrated Circuit Metrology, Inspection, and Process Control*, Proc. SPIE (1987).
- Davis, A. M., F. G. Rothenberg, N. Shepherd, and J. A. Izatt, "In vivo spectral domain optical coherence tomography volumetric imaging and spectral Doppler velocimetry of early stage embryonic chicken heart development," *Journal of the Optical Society of America A* **25**(12), 3134-3143 (2008).
- Davis, B. J., S. C. Schlachter, D. L. Marks, T. S. Ralston, S. A. Boppart, and P. S. Carney, "Nonparaxial vector-field modeling of optical coherence tomography and interferometric synthetic aperture microscopy," *Journal of the Optical Society of America A* **24**(9), 2527-2542 (2007).
- De Boer, J. F., B. Cense, B. H. Park, M. C. Pierce, G. J. Tearney, and B. E. Bouma, "Improved signal-to-noise ratio in spectral-domain compared with time-domain optical coherence tomography," *Optics Letters* **28**(21), 2067-2069 (2003).
- Denk, W., J. H. Strickler, and W. W. Webb, "Two-photon laser scanning fluorescence microscopy," *Science* **248**(4951), 73 (1990).

- Ding, Z., H. Ren, Y. Zhao, J. S. Nelson, and Z. Chen, "High-resolution optical coherence tomography over a large depth range with an axicon lens," *Optics Letters* **27**(4), 243-245 (2002).
- Divetia, A., T. H. Hsieh, J. Zhang, Z. Chen, M. Bachman, and G. P. Li, "Dynamically focused optical coherence tomography for endoscopic applications," *Applied Physics Letters* **86**, 103902 (2005).
- Drexler, W., U. Morgner, F. X. Kärtner, C. Pitris, S. A. Boppart, X. D. Li, E. P. Ippen, and J. G. Fujimoto, "In vivo ultrahigh-resolution optical coherence tomography," *Optics Letters* **24**(17), 1221-1223 (1999).
- Dubois, A., L. Vabre, A. C. Boccara, and E. Beaurepaire, "High-resolution full-field optical coherence tomography with a Linnik microscope," *Appl. Opt.* **41**, 805-812 (2002).
- Erikson, K. R., F. J. Fry, and J. P. Jones, "Ultrasound in medicine-a review," *IEEE Transactions on Sonics and Ultrasonics* **21**(3), 144-170 (1974).
- Fercher, A. F., K. Mengedoht, and W. Werner, "Eye-length measurement by interferometry with partially coherent light," *Optics Letters* **13**(3), 186-188 (1988).
- Fercher, A. F., C. K. Hitzenberger, G. Kamp, and S. Y. El-Zaiat, "Measurement of intraocular distances by backscattering spectral interferometry," *Optics Communications* **117**(1-2), 43-48 (1995).
- Fercher, A. F., W. Drexler, C. K. Hitzenberger, and T. Lasser, "Optical coherence tomography-principles and applications," *Reports on progress in physics* **66**(2), 239-303 (2003).
- Gonzalez, R. C. and R. E. Woods, *Digital Image Processing (2nd Edition)*. New Jersey, Prentice Hall (2002).
- Grulkowski, I., I. Gorczynska, M. Szkulmowski, D. Szlag, A. Szkulmowska, R. A. Leitgeb, A. Kowalczyk, and M. Wojtkowski, "Scanning protocols dedicated to smart velocity ranging in Spectral OCT," *Opt. Express* **17**, 23736-23754 (2009).
- Herz, P. R., Y. Chen, A. D. Aguirre, K. Schneider, P. Hsiung, J. G. Fujimoto, K. Madden, J. Schmitt, J. Goodnow, and C. Petersen, "Micromotor endoscope catheter for in vivo, ultrahigh-resolution optical coherence tomography," *Optics Letters* **29**, 2261-2263 (2004).
- Hitzenberger, C. K., "Optical measurement of the axial eye length by laser Doppler interferometry," *Investigative ophthalmology & visual science* **32**(3), 616-624 (1991).
- Holmes, J. and S. Hattersley, "Image blending and speckle noise reduction in multi-beam OCT." *Optical Coherence Tomography and Coherence Domain Optical Methods in Biomedicine XIII, Proc. of SPIE* (2009).
- Hounsfield, G. N., "Computerized transverse axial scanning (tomography): Part 1. Description of system," *Neurosurgical Classics*, 8 (1992).
- Huang, D., E. A. Swanson, C. P. Lin, J. S. Schuman, W. G. Stinson, W. Chang, M. R. Hee, T. Flotte, K. Gregory, C. A. Puliafito, and J. G. Fujimoto, "Optical coherence tomography," *Science* **254**(5035), 1178-1181 (1991).
- Huber, R., M. Wojtkowski, K. Taira, J. Fujimoto, and K. Hsu, "Amplified, frequency swept lasers for frequency domain reflectometry and OCT imaging: design and scaling principles," *Optics Express* **13**(9), 3513-3528 (2005a).

- Huber, R., M. Wojtkowski, J. G. Fujimoto, J. Y. Jiang, and A. E. Cable, "Three-dimensional and C-mode OCT imaging with a compact, frequency swept laser source at 1300 nm," *Optics Express* **13**(26), 10523-10538 (2005b).
- Huber, R., M. Wojtkowski, and J. G. Fujimoto, "Fourier Domain Mode Locking (FDML): A new laser operating regime and applications for optical coherence tomography," *Optics Express* **14**(8), 3225-3237 (2006).
- Iftimia, N. V., D. X. Hammer, R. D. Ferguson, M. Mujat, D. Vu, and A. A. Ferrante, "Dual-beam Fourier domain optical Doppler tomography of zebrafish," *Optics Express* **16**(18), 13624-13636 (2008).
- Izatt, J. A., M. R. Hee, G. M. Owen, E. A. Swanson, and J. G. Fujimoto, "Optical coherence microscopy in scattering media," *Optics Letters* **19**(8), 590-592 (1994).
- Izatt, J. A., M. D. Kulkarni, S. Yazdanfar, J. K. Barton, and A. J. Welch, "In vivo bidirectional color Doppler flow imaging of picoliter blood volumes using optical coherence tomography," *Optics Letters* **22**(18), 1439-1441 (1997).
- Jaillon, F., S. Makita, M. Yabusaki, and Y. Yasuno, "Parabolic BM-scan technique for full range Doppler spectral domain optical coherence tomography," *Opt. Express* **18**, 1358-1372 (2010).
- Kalender, W. A., "X-ray computed tomography," *Physics in Medicine and Biology* **51**(13), 29 (2006).
- Kasai, C., K. Namekawa, A. Koyano, and R. Omoto, "Real-time two-dimensional blood flow imaging using an autocorrelation technique," *IEEE Trans. Sonics Ultrason* **32**(3), 458-464 (1985).
- Lee, H. B., S. S. Kim, and G. Khang, *Polymeric Biomaterial. The Biomedical Engineering Handbook*, CRC Press, Boca Raton, FL, in cooperation with the IEEE Press. **Section IV**: p. 588 (1995).
- Lee, K. S., A. C. Akcay, T. Delemos, E. Clarkson, and J. P. Rolland, "Dispersion control with a Fourier-domain optical delay line in a fiber-optic imaging interferometer," *Applied optics* **44**(19), 4009-4022 (2005).
- Lee, K. S. and J. P. Rolland, "Bessel beam spectral-domain high-resolution optical coherence tomography with micro-optic axicon providing extended focusing range," *Optics Letters* **33**(15), 1696-1698 (2008).
- Lee, K. S., *Extended Focus Range High Resolution Endoscopic Optical Coherence Tomography*, Ph.D., The College of Optics and Photonics, University of Central Florida, (2008).
- Lee, K. S., P. Meemon, K. Hsu, W. J. Dallas, and J. P. Rolland, "Dual-reference full-range frequency domain optical coherence tomography." *Design and Quality for Biomedical Technologies II*, Proceedings of SPIE (2009).
- Lee, K. S., P. Meemon, and J. P. Rolland, "Dual detection full range frequency domain optical coherence tomography," *Optics letters* **35**(7), 1-3 (2010a).
- Lee, K. S., P. Vanderwall, and J. P. Rolland, "Two-photon microscopy with dynamic focusing objective using a liquid lens." *Multiphoton Microscopy in the Biomedical Sciences X*, Proceedings of SPIE (2010b).

- Leitgeb, R., L. Schmetterer, W. Drexler, A. Fercher, R. Zawadzki, and T. Bajraszewski, "Real-time assessment of retinal blood flow with ultrafast acquisition by color Doppler Fourier domain optical coherence tomography," *Optics Express* **11**(23), 3116-3121 (2003a).
- Leitgeb, R., C. Hitzenberger, and A. Fercher, "Performance of fourier domain vs. time domain optical coherence tomography," *Optics Express* **11**(8), 889-894 (2003b).
- Leitgeb, R. A., C. K. Hitzenberger, A. F. Fercher, and T. Bajraszewski, "Phase-shifting algorithm to achieve high-speed long-depth-range probing by frequency-domain optical coherence tomography," *Optics letters* **28**(22), 2201-2203 (2003).
- Leitgeb, R. A., R. Michaely, T. Lasser, and S. C. Sekhar, "Complex ambiguity-free Fourier domain optical coherence tomography through transverse scanning," *Optics letters* **32**(23), 3453-3455 (2007).
- Leon-Garcia, A., *Probability, statistics, and random processes for electrical engineering*, Prentice Hall (2007).
- Lerner, R. M., K. J. Parker, J. Holen, R. Gramiak, and R. C. Waag, "Sono-elasticity: Medical elasticity images derived from ultrasound signals in mechanically vibrated targets," *Acoust Imaging* **16**, 317-327 (1988).
- Lexer, F., C. K. Hitzenberger, W. Drexler, S. Molebny, H. Sattmann, M. Sticker, and A. F. Fercher, "Dynamic coherent focus OCT with depth-independent transversal resolution," *Journal of Modern Optics* **46**(3), 541-553 (1999).
- Liu, Y. C. and A. S. Chiang, "High-resolution confocal imaging and three-dimensional rendering," *Methods* **30**(1), 86-93 (2003).
- Lytle, J. D., Polymeric Optics. *Handbook of Optics*, McGraw Hill, New York. **Vol. II:** p. 7 (1995).
- Makita, S., T. Fabritius, and Y. Yasuno, "Blood flow imaging at deep posterior human eye using 1 m spectral-domain optical coherence tomography." *Optical Coherence Tomography and Coherence Domain Optical Methods in Biomedicine XIII (San Jose, CA, USA )*, Proceedings of SPIE (2009).
- Mao, Y., S. Sherif, C. Flueraru, and S. Chang, "3x3 Mach-Zehnder interferometer with unbalanced differential detection for full-range swept-source optical coherence tomography," *Applied Optics* **47**(12), 2004-2010 (2008).
- Mariampillai, A., B. A. Standish, N. R. Munce, C. Randall, G. Liu, J. Y. Jiang, A. E. Cable, I. A. Vitkin, and V. X. D. Yang, "Doppler optical cardiogram gated 2D color flow imaging at 1000 fps and 4D in vivo visualization of embryonic heart at 45 fps on a swept source OCT system," *Optics Express* **15**(4), 1627-1638 (2007).
- Mariampillai, A., B. A. Standish, E. H. Moriyama, M. Khurana, N. R. Munce, M. K. K. Leung, J. Jiang, A. Cable, B. C. Wilson, and I. A. Vitkin, "Speckle variance detection of microvasculature using swept-source optical coherence tomography," *Opt. Lett* **33**, 1530-1532 (2008).
- Meemon, P., K. S. Lee, S. Murali, and J. Rolland, "Optical design of a dynamic focus catheter for high-resolution endoscopic optical coherence tomography," *Applied optics* **47**(13), 2452-2457 (2008a).

- Meemon, P., M. Salem, K. S. Lee, M. Chopra, and J. P. Rolland, "Determination of the coherency matrix of a broadband stochastic electromagnetic light beam," *Journal of Modern Optics* **55**(17), 2765-2776 (2008b).
- Minsky, M., *Microscopy Apparatus*, U. S. patent No. 3,013,467 (December 19, 1961)
- Murali, S., K. S. Lee, and J. P. Rolland, "Invariant resolution dynamic focus OCM based on liquid crystal lens," *Optics Express* **15**(24), 15854-15862 (2007).
- Murali, S., K. P. Thompson, and J. P. Rolland, "Three-dimensional adaptive microscopy using embedded liquid lens," *Optics letters* **34**(2), 145-147 (2009).
- Murali, S., *Gabor Domain Optical Coherence Microscopy*, Ph.D., The College of Optics and Photonics, University of Central Florida, (2009).
- Nave, R., "Effective Fluid Speed in a Tube." Retrieved February 10, from <http://hyperphysics.phy-astr.gsu.edu/Hbase/pftric.html#veff> (2010).
- Nelson, J. S., K. M. Kelly, Y. Zhao, and Z. Chen, "Imaging blood flow in human port-wine stain in situ and in real time using optical Doppler tomography," *Archives of dermatology* **137**(6), 741 (2001).
- Ophir, J., I. Cespedes, H. Ponnekanti, Y. Yazdi, and X. Li, "Elastography: A quantitative method for imaging the elasticity of biological tissues," *Ultrasonic imaging(Print)* **13**(2), 111-134 (1991).
- Park, B. H., M. C. Pierce, B. Cense, S. H. Yun, M. Mujat, G. J. Tearney, B. E. Bouma, and J. F. de Boer, "Real-time fiber-based multi-functional spectral-domain optical coherence tomography at 1.3  $\mu\text{m}$ ," *Optics Express* **13**, 3931-3944 (2005).
- Parker, K. J., S. R. Huang, R. A. Musulin, and R. M. Lerner, "Tissue response to mechanical vibrations for sonoelasticity imaging," *Ultrasound in medicine & biology* **16**(3), 241-246 (1990).
- Parker, K. J., L. Gao, R. M. Lerner, and S. F. Levinson, "Techniques for elastic imaging: A review," *IEEE Engineering in Medicine and Biology Magazine* **15**(6), 52-59 (1996).
- Pedersen, C. J., D. Huang, M. A. Shure, and A. M. Rollins, "Measurement of absolute flow velocity vector using dual-angle, delay-encoded Doppler optical coherence tomography," *Optics Letters* **32**(5), 506-508 (2007).
- Piao, D. and Q. Zhu, "Quantifying Doppler angle and mapping flow velocity by a combination of Doppler-shift and Doppler-bandwidth measurements in optical Doppler tomography," *Applied optics* **42**(25), 5158-5166 (2003).
- Podoleanu, A., J. Rogers, D. Jackson, and S. Dunne, "Three dimensional OCT images from retina and skin," *Optics Express* **7**(9), 292-298 (2000).
- Potsaid, B., I. Gorczynska, V. J. Srinivasan, Y. Chen, J. Jiang, A. Cable, and J. G. Fujimoto, "Ultrahigh speed Spectral/Fourier domain OCT ophthalmic imaging at 70,000 to 312,500 axial scans per second," *Optics Express* **16**(19), 15149-15169 (2008).
- Povazay, B., A. Unterhuber, B. Hermann, H. Sattmann, H. Arthaber, and W. Drexler, "Full-field time-encoded frequency-domain optical coherence tomography," *Optics Express* **14**(17), 7661-7669 (2006).



- Qi, B., A. Phillip Himmer, L. Maggie Gordon, X. D. Victor Yang, L. David Dickensheets, and I. Alex Vitkin, "Dynamic focus control in high-speed optical coherence tomography based on a microelectromechanical mirror," *Optics Communications* **232**(1-6), 123-128 (2004).
- Roguin, A., "Christian Johann Doppler: the man behind the effect," *British Journal of Radiology* **75**(895), 615 (2002).
- Rolland, J. P., P. Meemon, S. Murali, A. Jain, N. Papp, K. P. Thompson, and K. S. Lee, "Gabor domain optical coherence microscopy." 1st Canterbury Workshop on Optical Coherence Tomography and Adaptive Optics (Canterbury, United Kingdom), *Proceeding of SPIE* (2008).
- Rolland, J. P., P. Meemon, S. Murali, K. P. Thompson, and K. S. Lee, "Gabor-based fusion technique for Optical Coherence Microscopy," *Optics Express* **18**, 3632-3642 (2010a).
- Rolland, J. P., P. Meemon, S. Murali, K. P. Thompson, and K. Lee, "Gabor-based fusion technique for Optical Coherence Microscopy," *Opt. Express* **18**, 3632-3642 (2010b).
- Rost, F. W. D., *Fluorescence microscopy*, Cambridge Univ Pr (1995).
- Sarvazyan, A., "Shear acoustic properties of soft biological tissues in medical diagnostics," *The Journal of the Acoustical Society of America* **93**, 2329 (1993).
- Schmitt, J., "OCT elastography: imaging microscopic deformation and strain of tissue," *Optics Express* **3**(6), 199-211 (1998).
- Schmitt, J. M., S. L. Lee, and K. M. Yung, "An optical coherence microscope with enhanced resolving power in thick tissue," *Optics Communications* **142**(4-6), 203-207 (1997).
- Schmoll, T., C. Kolbitsch, and R. A. Leitgeb, "Ultra-high-speed volumetric tomography of human retinal blood flow," *Optics Express* **17**(5), 4166-4176 (2009).
- Sherar, M. D., M. B. Noss, and F. S. Foster, "Ultrasound backscatter microscopy images the internal structure of living tumor spheroids," *Nature* **330**(3), 493-495 (1987).
- Sigel, B., "A brief history of Doppler ultrasound in the diagnosis of peripheral vascular disease," *Ultrasound in medicine & biology* **24**(2), 169-176 (1998).
- So, P. T. C., C. Y. Dong, B. R. Masters, and K. M. Berland, "Two-photon excitation fluorescence microscopy," *Annual Review of Biomedical Engineering* **2**(1), 399-429 (2000).
- Szkulmowski, M., A. Szkulmowska, T. Bajraszewski, A. Kowalczyk, and M. Wojtkowski, "Flow velocity estimation using joint Spectral and Time domain Optical Coherence Tomography," *Optics Express* **16**, 6008-6025 (2008a).
- Szkulmowski, M., A. Szkulmowska, T. Bajraszewski, A. Kowalczyk, and M. Wojtkowski, "Flow velocity estimation using joint Spectral and Time domain Optical Coherence Tomography," *Opt. Express* **16**, 6008-6025 (2008b).
- Szkulmowski, M., I. Grulkowski, D. Szig, A. Szkulmowska, A. Kowalczyk, and M. Wojtkowski, "Flow velocity estimation by complex ambiguity free joint Spectral and Time domain Optical Coherence Tomography," *Optics Express* **17**(16), 14281-14297 (2009).
- Targowski, P., M. Wojtkowski, A. Kowalczyk, T. Bajraszewski, M. Szkulmowski, and I. Gorczy ska, "Complex spectral OCT in human eye imaging in vivo," *Optics Communications* **229**(1-6), 79-84 (2004).

- Tearney, G. J., S. A. Boppart, B. E. Bouma, M. E. Brezinski, N. J. Weissman, J. F. Southern, and J. G. Fujimoto, "Scanning single-mode fiber optic catheter-endoscope for optical coherence tomography," *Optics Letters* **21**(7), 543-545 (1996).
- Tran, P. H., D. S. Mukai, M. Brenner, and Z. Chen, "In vivo endoscopic optical coherence tomography by use of a rotational microelectromechanical system probe," *Optics Letters* **29**(11), 1236-1238 (2004).
- Tumlinson, A. R., J. K. Barton, J. McNally, A. Unterhuber, B. Hermann, H. Sattman, and W. Drexler, "An achromatized endoscope for ultrahigh-resolution optical coherence tomography." *Optical Coherence Tomography and Coherence Techniques II, Proc. of SPIE* (2005).
- Vakoc, B. J., S. H. Yun, G. J. Tearney, and B. E. Bouma, "Elimination of depth degeneracy in optical frequency-domain imaging through polarization-based optical demodulation," *Optics letters* **31**(3), 362-364 (2006).
- Vakoc, B. J., R. M. Lanning, J. A. Tyrrell, T. P. Padera, L. A. Bartlett, T. Stylianopoulos, L. L. Munn, G. J. Tearney, D. Fukumura, and R. K. Jain, "Three-dimensional microscopy of the tumor microenvironment in vivo using optical frequency domain imaging," *Nature medicine* **15**(10), 1219-1223 (2009).
- Walther, J. and E. Koch, "Transverse motion as a source of noise and reduced correlation of the Doppler phase shift in spectral domain OCT," *Opt. Express* **17**, 19698-19713 (2009).
- Walz, M., J. Teubner, and M. Georgi, "Elasticity of benign and malignant breast lesions, imaging, application and results in clinical and general practice." 8th Int. Congress on the Ultrasonic Examination of the Breast (1993).
- Wang, L. V. and H. I. Wu, *Biomedical Optics: Principles and Imaging*, Wiley-Interscience (2007).
- Wang, R. K., Z. Ma, and S. Kirkpatrick, "Tissue Doppler optical coherence elastography for real time strain rate and strain mapping of soft tissue," *Applied Physics Letters* **89**, 144103 (1-3) (2006).
- Wang, R. K., S. L. Jacques, Z. Ma, S. Hurst, S. R. Hanson, and A. Gruber, "Three dimensional optical angiography," *Opt. Express* **15**, 4083-4097 (2007).
- Wang, R. K., "Three-dimensional optical micro-angiography maps directional blood perfusion deep within microcirculation tissue beds in vivo," *Physics in medicine and biology* **52**, N531 (2007a).
- Wang, R. K., "In vivo full range complex Fourier domain optical coherence tomography," *Applied Physics Letters* **90**, 054103 (2007b).
- Wang, R. K., "Directional blood flow imaging in volumetric optical microangiography achieved by digital frequency modulation," *Optics letters* **33**(16), 1878-1880 (2008).
- Wang, R. K., L. An, P. Francis, and D. J. Wilson, "Depth-resolved imaging of capillary networks in retina and choroid using ultrahigh sensitive optical microangiography," *Optics letters* **35**(9), 1467-1469 (2010).
- Wang, Y., B. A. Bower, J. A. Izatt, O. Tan, and D. Huang, "In vivo total retinal blood flow measurement by Fourier domain Doppler optical coherence tomography," *Journal of Biomedical Optics* **12**, 041215 (2007).

- Wang, Y., A. Fawzi, O. Tan, J. Gil-Flamer, and D. Huang, "Retinal blood flow detection in diabetic patients by Doppler Fourier domain optical coherence tomography," *Optics Express* **17**(5), 4061-4073 (2009).
- Weisstein, E. W., "Gaussian Function." Retrieved March 5, from <http://mathworld.wolfram.com/GaussianFunction.html> (2010).
- White, B., M. Pierce, N. Nassif, B. Cense, B. Park, G. Tearney, B. Bouma, T. Chen, and J. de Boer, "In vivo dynamic human retinal blood flow imaging using ultra-high-speed spectral domain optical coherence tomography," *Optics Express* **11**(25), 3490-3497 (2003).
- White, D. N., "Johann Christian Doppler and his effect--a brief history," *Ultrasound in medicine & biology* **8**(6), 583 (1982).
- Wojtkowski, M., A. Kowalczyk, R. Leitgeb, and A. F. Fercher, "Full range complex spectral optical coherence tomography technique in eye imaging," *Optics Letters* **27**(16), 1415-1417 (2002).
- Wyant, J. C., "Use of an ac heterodyne lateral shear interferometer with real-time wavefront correction systems," *Applied optics* **14**(11), 2622-2626 (1975).
- Xie, T., S. Guo, Z. Chen, D. Mukai, and M. Brenner, "GRIN lens rod based probe for endoscopic spectral domain optical coherence tomography with fast dynamic focus tracking," *Optics Express* **14**(8), 3238-3246 (2006).
- Yang, V. X. D., M. L. Gordon, A. Mok, Y. Zhao, Z. Chen, R. S. C. Cobbold, B. C. Wilson, and I. Alex Vitkin, "Improved phase-resolved optical Doppler tomography using the Kasai velocity estimator and histogram segmentation," *Optics Communications* **208**(4-6), 209-214 (2002).
- Yang, V. X. D., M. Gordon, S. Tang, N. Marcon, G. Gardiner, B. Qi, S. Bisland, E. Seng-Yue, S. Lo, and J. Pekar, "High speed, wide velocity dynamic range Doppler optical coherence tomography (Part III): in vivo endoscopic imaging of blood flow in the rat and human gastrointestinal tracts," *Optics Express* **11**(19), 2416-2424 (2003a).
- Yang, V. X. D., M. L. Gordon, B. Qi, J. Pekar, S. Lo, E. Seng-Yue, A. Mok, B. C. Wilson, and I. A. Vitkin, "High speed, wide velocity dynamic range Doppler optical coherence tomography (Part I): System design, signal processing, and performance," *Optics Express* **11**(7), 794-809 (2003b).
- Yaqoob, Z., J. Wu, E. J. McDowell, X. Heng, and C. Yang, "Methods and application areas of endoscopic optical coherence tomography," *Journal of Biomedical Optics* **11**, 063001 (2006).
- Yasuno, Y., S. Makita, T. Endo, G. Aoki, M. Itoh, and T. Yatagai, "Simultaneous BM-mode scanning method for real-time full-range Fourier domain optical coherence tomography," *Applied Optics* **45**(8), 1861-1865 (2006).
- Yun, S. H., G. J. Tearney, J. F. de Boer, and B. E. Bouma, "Motion artifacts in optical coherence tomography with frequency-domain ranging," *Optics Express* **12**(13), 2977-2998 (2004).
- Zhang, J., W. Jung, J. Nelson, and Z. Chen, "Full range polarization-sensitive Fourier domain optical coherence tomography," *Optics Express* **12**(24), 6033-6039 (2004).
- Zhao, Y., Z. Chen, C. Saxer, S. Xiang, J. F. de Boer, and J. S. Nelson, "Phase-resolved optical coherence tomography and optical Doppler tomography for imaging blood flow in human

- skin with fast scanning speed and high velocity sensitivity," *Optics letters* **25**(2), 114-116 (2000a).
- Zhao, Y., Z. Chen, C. Saxer, Q. Shen, S. Xiang, J. F. de Boer, and J. S. Nelson, "Doppler standard deviation imaging for clinical monitoring of in vivo human skin blood flow," *Optics letters* **25**(18), 1358-1360 (2000b).